1993

Dynamic D Sight for measuring surface vibration.

Philip Albert. Aylesworth
University of Windsor

NOTICE

The quality of this microform is heavily dependent upon the quality of the original thesis submitted for microfilming. Every effort has been made to ensure the highest quality of reproduction possible.

If pages are missing, contact the university which granted the degree.

Some pages may have indistinct print especially if the original pages were typed with a poor typewriter ribbon or if the university sent us an inferior photocopy.

Reproduction in full or in part of this microform is governed by the Canadian Copyright Act, R.S.C. 1970, c. C-30, and subsequent amendments.

AVIS

La qualité de cette microforme dépend grandement de la qualité de la thèse soumise au microfilmage. Nous avons tout fait pour assurer une qualité supérieure de reproduction.

S'il manque des pages, veuillez communiquer avec l'université qui a conféré le grade.

La qualité d'impression de certaines pages peut laisser à désirer, surtout si les pages originales ont été dactylographiées à l'aide d'un ruban usé ou si l'université nous a fait parvenir une photocopie de qualité inférieure.

La reproduction, même partielle, de cette microforme est soumise à la Loi canadienne sur le droit d'auteur, SRC 1970, c. C-30, et ses amendements subséquents.

Canada

Dynamic D Sight for Measuring Surface Vibration

A Thesis Submitted to the
Faculty of Graduate Studies and Research
through the Department of Mechanical Engineering
in Partial Fulfillment of the Requirements for the
Degree of Master of Applied Science
at the University of Windsor

Philip A. Aylesworth

Canada

Subject Categories

THE HUMANITIES AND SOCIAL SCIENCES

COMMUNICATIONS AND THE ARTS
Architecture 0729
Art History 0377
Cinema 0900
Dance 0378
Fine Arts 0357
Information Science 0723
Journalism 0391
Library Science 0399
Mass Communications 0708
Music 0413
Speech Communication 0459
Theater 0465

EDUCATION
General 0515
Administration 0514
Adult and Continuing 0516
Agricultural 0517
Art 0273
Bilingual and Multicultural 0282
Business 0688
Community College 0275
Curriculum and Instruction 0727
Early Childhood 0518
Elementary 0524
Finance 0277
Guidance and Counseling 0519
Health 0680
Higher 0745
History of 0520
Home Economics 0278
Industrial 0521
Language and Literature 0279
Mathematics 0280
Music 0522
Philosophy of 0998
Physical 0523

Psychology 0525
Reading 0535
Religious 0527
Sciences 0714
Secondary 0533
Social Sciences 0534
Sociology of 0340
Special 0529
Teacher Training 0530
Technology 0710
Tests and Measurements 0288
Vocational 0747

LANGUAGE, LITERATURE AND LINGUISTICS
Language
 General 0679
 Ancient 0289
 Linguistics 0290
 Modern 0291
Literature
 General 0401
 Classical 0294
 Comparative 0295
 Medieval 0297
 Modern 0298
 African 0316
 American 0591
 Asian 0305
 Canadian (English) 0352
 Canadian (French) 0355
 English 0593
 Germanic 0311
 Latin American 0312
 Middle Eastern 0315
 Romance 0313
 Slavic and East European 0314

PHILOSOPHY, RELIGION AND THEOLOGY
Philosophy 0422
Religion
 General 0318
 Biblical Studies 0321
 Clergy 0319
 History of 0320
 Philosophy of 0322
Theology 0469

SOCIAL SCIENCES
American Studies 0323
Anthropology
 Archaeology 0324
 Cultural 0326
 Physical 0327
Business Administration
 General 0310
 Accounting 0272
 Banking 0770
 Management 0454
 Marketing 0338
Canadian Studies 0385
Economics
 General 0501
 Agricultural 0503
 Commerce-Business 0505
 Finance 0508
 History 0509
 Labor 0510
 Theory 0511
Folklore 0358
Geography 0366
Gerontology 0351
History
 General 0578

Ancient 0579
Medieval 0581
Modern 0582
Black 0328
African 0331
Asia, Australia and Oceania 0332
Canadian 0334
European 0335
Latin American 0336
Middle Eastern 0333
United States 0337
History of Science 0585
Law 0398
Political Science
 General 0615
 International Law and
  Relations 0616
 Public Administration 0617
Recreation 0814
Social Work 0452
Sociology
 General 0626
 Criminology and Penology ... 0627
 Demography 0938
 Ethnic and Racial Studies 0631
 Individual and Family
  Studies 0628
 Industrial and Labor
  Relations 0629
 Public and Social Welfare 0630
 Social Structure and
  Development 0700
 Theory and Methods 0344
Transportation 0709
Urban and Regional Planning 0999
Women's Studies 0453

THE SCIENCES AND ENGINEERING

BIOLOGICAL SCIENCES
Agriculture
 General 0473
 Agronomy 0285
 Animal Culture and
  Nutrition 0475
 Animal Pathology 0476
 Food Science and
  Technology 0359
 Forestry and Wildlife 0478
 Plant Culture 0479
 Plant Pathology 0480
 Plant Physiology 0817
 Range Management 0777
 Wood Technology 0746
Biology
 General 0306
 Anatomy 0287
 Biostatistics 0308
 Botany 0309
 Cell 0379
 Ecology 0329
 Entomology 0353
 Genetics 0369
 Limnology 0793
 Microbiology 0410
 Molecular 0307
 Neuroscience 0317
 Oceanography 0416
 Physiology 0433
 Radiation 0821
 Veterinary Science 0778
 Zoology 0472
Biophysics
 General 0786
 Medical 0760

EARTH SCIENCES
Biogeochemistry 0425
Geochemistry 0996

Geodesy 0370
Geology 0372
Geophysics 0373
Hydrology 0388
Mineralogy 0411
Paleobotany 0345
Paleoecology 0426
Paleontology 0418
Paleozoology 0985
Palynology 0427
Physical Geography 0368
Physical Oceanography 0415

HEALTH AND ENVIRONMENTAL SCIENCES
Environmental Sciences 0768
Health Sciences
 General 0566
 Audiology 0300
 Chemotherapy 0992
 Dentistry 0567
 Education 0350
 Hospital Management 0769
 Human Development 0758
 Immunology 0982
 Medicine and Surgery 0564
 Mental Health 0347
 Nursing 0569
 Nutrition 0570
 Obstetrics and Gynecology .. 0380
 Occupational Health and
  Therapy 0354
 Ophthalmology 0381
 Pathology 0571
 Pharmacology 0419
 Pharmacy 0572
 Physical Therapy 0382
 Public Health 0573
 Radiology 0574
 Recreation 0575

Speech Pathology 0460
Toxicology 0383
Home Economics 0386

PHYSICAL SCIENCES
Pure Sciences
Chemistry
 General 0485
 Agricultural 0749
 Analytical 0486
 Biochemistry 0487
 Inorganic 0488
 Nuclear 0738
 Organic 0490
 Pharmaceutical 0491
 Physical 0494
 Polymer 0495
 Radiation 0754
Mathematics 0405
Physics
 General 0605
 Acoustics 0986
 Astronomy and
  Astrophysics 0606
 Atmospheric Science 0608
 Atomic 0748
 Electronics and Electricity 0607
 Elementary Particles and
  High Energy 0798
 Fluid and Plasma 0759
 Molecular 0609
 Nuclear 0610
 Optics 0752
 Radiation 0756
 Solid State 0611
Statistics 0463

Applied Sciences
Applied Mechanics 0346
Computer Science 0984

Engineering
 General 0537
 Aerospace 0538
 Agricultural 0539
 Automotive 0540
 Biomedical 0541
 Chemical 0542
 Civil 0543
 Electronics and Electrical 0544
 Heat and Thermodynamics ... 0348
 Hydraulic 0545
 Industrial 0546
 Marine 0547
 Materials Science 0794
 Mechanical 0548
 Metallurgy 0743
 Mining 0551
 Nuclear 0552
 Packaging 0549
 Petroleum 0765
 Sanitary and Municipal 0554
 System Science 0790
Geotechnology 0428
Operations Research 0796
Plastics Technology 0795
Textile Technology 0994

PSYCHOLOGY
General 0621
Behavioral 0384
Clinical 0622
Developmental 0620
Experimental 0623
Industrial 0624
Personality 0625
Physiological 0989
Psychobiology 0349
Psychometrics 0632
Social 0451

✪

Abstract

D Sight is an optical method for exaggerating local variations in the contours of a surface. It has been implemented in a commercial product for the inspection of automobile bodies and glass. This research explores extending its use on steady-state dynamic (vibrating) surfaces.

The objectives of the research were to determine if D Sight can be used to determine the mode shapes and location of nodes in a steady-state vibrating surface; to study the effect of varying the angle of incidence and determine an optimum angle; to correlate these results with finite element vibration analysis; and to determine if this method can be applied to the problem of locating subsurface debonds.

Dynamic D Sight was very effective in determining the mode shapes and location. The result is a visual technique that can be used in real time. It was verified by simply feeling the vibrating surface to determine the node locations and also using a laser reflected off the surface to determine node and anti-node locations. The low cost of

D Sight, the fact that part registration is not a problem, and the fact that it can be viewed in real time make it a very attractive alternative to holography.

It was found that as the angle of incidence increased the contrast of the image increased. This will provide a better image in the case of small amplitude vibrations or if the surface is not very bright. Since the surface used was polished brass, the image was sufficiently contrasty to use at small angles of incidence which has the advantage of very little perspective distortion and less loss due to parallax error. For this reason a small angle of incidence was found to be optimum for this surface.

The finite element vibration modeling found many mode shapes but seemed to miss some that were very evident in the experimental work. A theoretical method showed that some modes appeared differently than expected. Otherwise there was a fair correlation between the mode shapes that were found in both.

To look for debonds a cross-brace was fastened to the back of a brass plate. Dynamic D Sight enhanced the image of the debonds although the debonds were visible even in the static D Sight images. In another case a point contact was fastened to the back of the plate. Again it was visible in the static view but in the Dynamic D Sight image it could be observed how the point contact affected the mode shapes of the vibrating plate. In both cases the Dynamic D Sight enhanced the detection of the bonds and debonds in the plate.

Acknowledgments

The author wishes to thank the many people for their part in this work. My wife Susan kept prodding me on so that I didn't fall too far behind schedule (although she may not agree with that assessment). Sam Basile was an incredible help with theoretical questions for the Finite Element Analysis (he actually called regularly to see how things were going!), and Mike Reiser helped get me up and going with the FEA software (it may have only been a few minutes, but it probably saved me a month).

Robert Tattersall was always there when I needed his technical skills (although his advice as to what I should do with that part was not always appreciated). My employer, Dr. William Miller has given much help and encouragement, as well as the use of some equipment.

Of course it would not have been possible without my supervisor, Dr. Walter North, whose help and encouragement was invaluable.

Table of Contents

List of Tables

List of Figures

Introduction

1.1 Introduction to D Sight

D Sight is a trademark owned by Diffracto Limited, Windsor, Ontario and refers to a patented technique which visually exaggerates flaws in a smooth glossy surface.

D Sight is a phenomenon that occurs when a light source is reflected from a specular (i.e. highly reflective) object onto a retroreflective screen (retroreflector) and then viewed from a point very close to the light source as shown in Figure 1. Light and dark areas are seen on the surface of the object. The intensity of light in these areas is proportional to the local change in slope of the surface of the object.[1] Since it is local slope that D Sight detects, it is insensitive to gentle continuous slope changes.[2] For this reason precision fixtures are not required.

D Sight is also very sensitive, able to detect flaws as small as 1 μm if they are very localized.[3]

The retroreflector (in this case 3M Scotchlite) is made up of very small
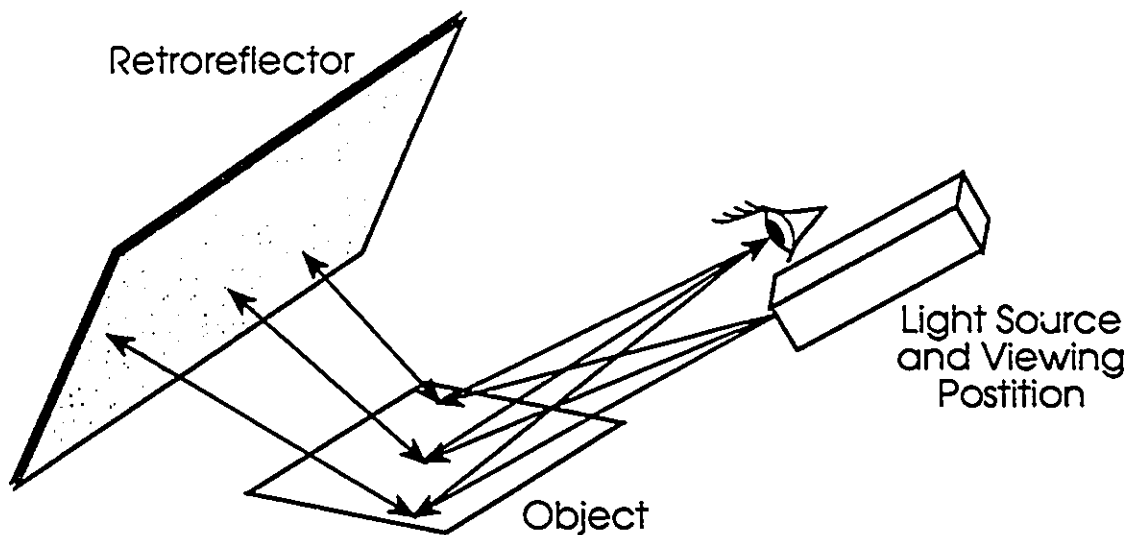
FIGURE 1: D Sight Setup

(approximately 0.127 mm), high refractive index glass beads with a reflective coating on the back, bonded to a flexible sheet. This screen will reflect light back in the same direction as the incident light as shown in Figure 2. Since the retroreflector is not perfect, the light is slightly scattered, returning a cone of light in the incident direction, see Figure 3.

When light is reflected from the object onto the retroreflector, an image of local distortion is formed on the retroreflector due to local changes in the slope of the object as illustrated in Figure 4. This is called the primary image. If the object were uniformly curved, the retroreflector would receive an even illumination and there would be no image, it is only local changes in slope that create this image. Figure 5 illustrates viewing the D Sight image on the surface. The flaws are small enough that they do not have a serious impact on the returned image, so it is assumed to be perfectly reflected.
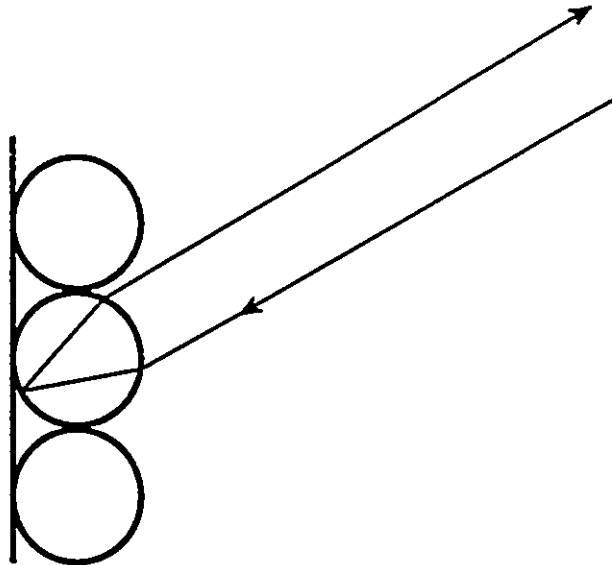
FIGURE 2: A Single Ray Hitting a Retroreflector

Incident Light

Reflected Light
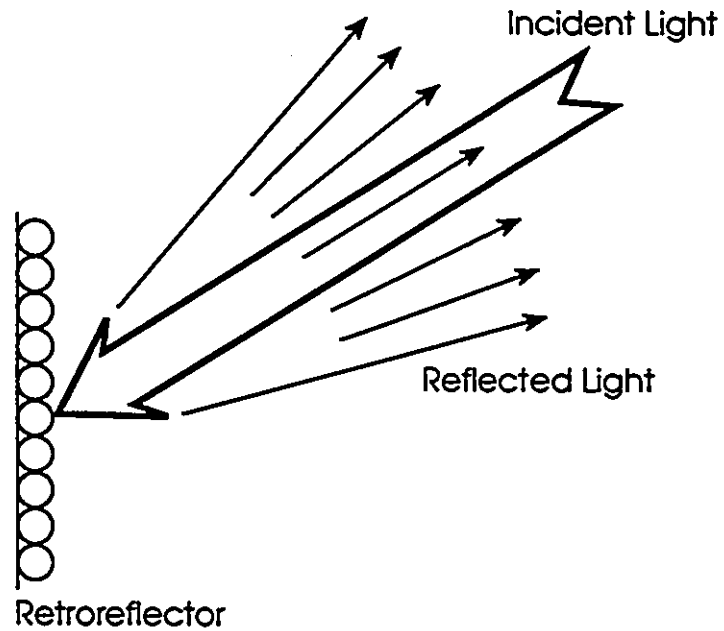
Retroreflector

FIGURE 3: Retroreflective Screen

Retroreflector

Light Source

Surface of Object
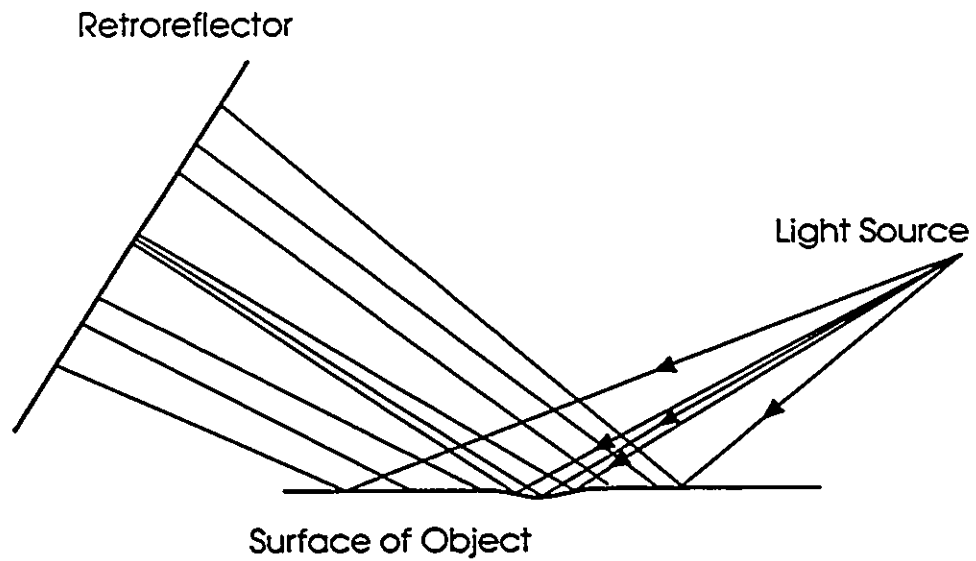
FIGURE 4: An Image Is Formed on the Retroreflector

Retroreflector

Viewing Position

Surface of Object
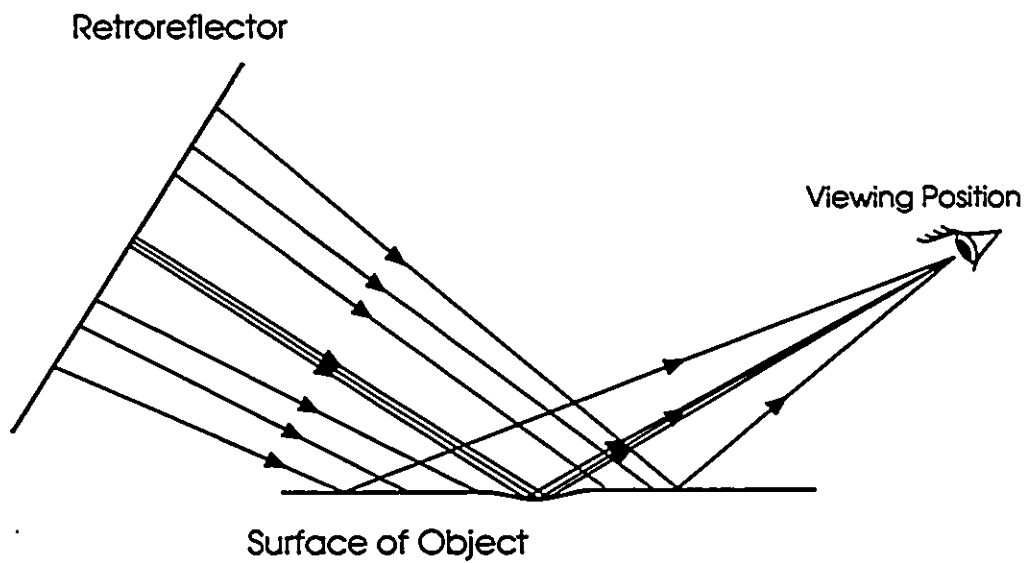
FIGURE 5: Viewing a D Sight Image

If this flaw were a linear trough in the part, an image as shown in Figure 6 would be seen. The bright area indicates a concave surface, the darker areas indicate a convex surface, and uniform grey indicates uniform curvature.

Viewing Position
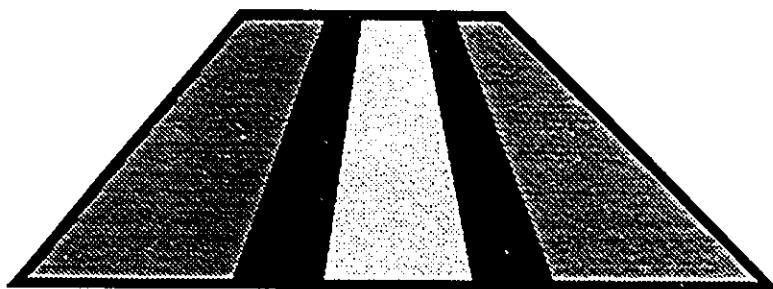
Surface of Object

FIGURE 6: Hypothetical D Sight Image

1.2 Applications of D Sight

The use of D Sight for viewing contours of static surfaces has been explored extensively. Diffracto markets several products to detect flaws in painted metal and plastic parts.

1.3 Dynamic D Sight

This research explores the possibility of using D Sight in the case of a dynamic surface, therefore, the term Dynamic D Sight will be used. By using D Sight to view a

vibrating surface it was hoped that mode shapes and locations could be determined visually.

A strobe light was used to freeze the motion of the vibrating surface. Other methods may be possible such as video cameras with very fast shutter speeds or even high speed video which would allow slow motion playback of the moving surface.

The goal was to produce a high contrast image of the node locations at their actual location on the smooth flat plate. For this reason, unlike typical D Sight, a small angle of incidence (near normal) was preferred. No attempt was made to determine numerical slope or displacement information, rather it was intended for visual interpretation.

Optically the process is related to shadowgraphy. Indeed if the retroreflector is replaced by a diffuse screen of white paper for example, the image on this diffuse surface is that of shadowgraphy. While white paper generates a D Sight image without secondary images, the efficiency is low. However, this image is then returned by the retroreflector through the surface for a second pass, to be imaged near the location of the point light source. Parallel light for cannot be used for D Sight as it does not work in the manner described here.

Clark, Reynolds, and Pryor[4] have patented the technique which visually exaggerates flaws in a smooth glossy surface, this is marketed by Diffracto Ltd. under the trademark D-Sight.

Many applications of this technology have been explored. **Heywood**[5] describes its use for detecting waviness in composite components. **Austin and Barrett**[6] used D Sight for quality control of tool and die services as well as sheet metal automotive parts. **Komorowski, Gould, and Pastorius**[7] use D Sight to detect impact damage to composite

aircraft structure and **Komorowski, Simpson, and Gould**[8] describe its use on metal aircraft to detect cold-worked holes, cracks, and surface corrosion.

Reynolds[9] has fabricated test plaques for surface waviness which are a circular sine wave formation. D Sight images of these plaques show that although D Sight is more sensitive to waves across the line of sight, it can still detect waves along the line of sight.

Several attempts by Diffracto to quantify the grey level image in order to produce general contour information have had limited success. **Montrose**[10] tried to quantify grey level to contour data and showed that local slope and rate of change of local slope are important parameters.

Aylesworth and North[11] demonstrated that it was possible to use D Sight on a dynamic surface.

Objectives

D Sight has proven itself as a useful tool for quality control of surfaces, such as automobile sheet metal and glass parts. In this research an investigation of the use of D Sight to view steady state dynamic (vibrating) surfaces will be undertaken with the following objectives:

1. To determine if D Sight can be used to find the mode shapes and location of nodes on a steady state vibrating surface.

2. To study the effect of varying the angle of incidence (of illumination) and to determine an optimum angle.

3. To correlate the results from above with results of finite element vibration analysis.

4. To determine if this method can be applied to the problem of locating subsurface debonds.

Experimental Work

4.1 Overview

In all experiments the plate was viewed using D Sight. The setup is shown in Figure 7 and the dimensions are listed in Table 1. A thin brass plate with a bright surface was rigidly clamped on all four edges in a heavy steel frame mounted in the vertical orientation as shown in Figure 8. A strobe light was bounced off the surface onto a retroreflective screen. (The orientation of the retroreflector is not critical as it has a very high efficiency up to about ±30° from the normal.) The image on this screen was viewed through the reflection on the brass plate from a location slightly (50 mm) off axis to the strobe. The distance from the camera to the object and from the object to the retroreflector were both fixed at 2 metres.

The brass plate was vibrated acoustically using a speaker located directly behind it. This was driven by an amplifier, from a signal produced by a function generator which had two output channels of the same frequency. This frequency could be adjusted continuously
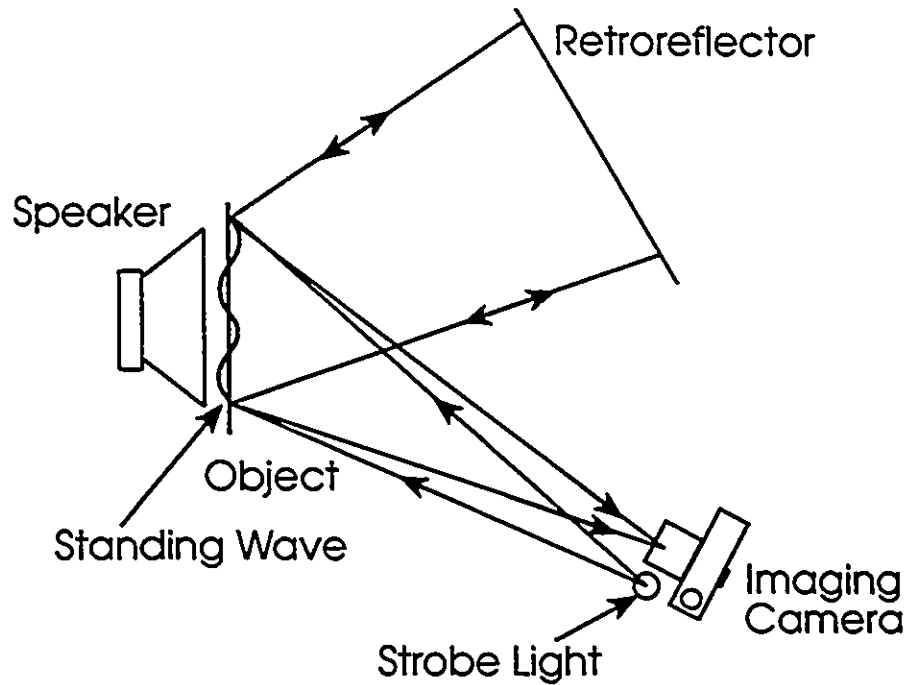
FIGURE 7: Setup for Dynamic Experiments

between 10 Hz and 20,000 Hz, although the strobe light limited the maximum frequency to about 600 Hz. The first channel was a sine wave output to a power amplifier to drive the speaker. The second channel was output as a square wave to the external trigger input on the strobe light. The phase angle between the two channels could be varied continuously.

Description	Measurement
Camera to Plate Distance	2 m
Plate to Retroreflector Distance	2 m
Strobe to Camera Distance (centre to centre)	50 mm
Plate Height and Width (free area)	305 mm
Plate Thickness	0.508 or 0.635 mm
Sphere size in retroreflector	0.1 mm
Retroreflector (height X width)	0.9 X 1.2 m
Exposure (typical)	f/8 @ 2s

TABLE 1: Dimensions of Experimental Setup
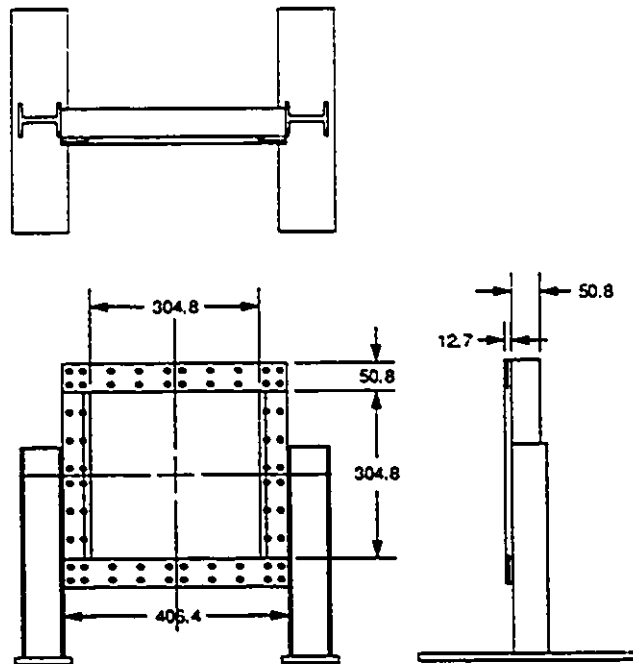
FIGURE 8: Diagram of Plate Assembly

Colour slide film and black and white print film with Exposure Index 1600 and 400 were used in a 35 mm camera to record the images. The camera was used in manual mode because the automatic metering system would not be able to handle the illumination from the strobe light. Exposure was determined by taking a test roll of slide film at various exposures and determining the best exposure from the resulting slides. Slide film was used because of its narrow exposure latitude and the fact that the processing lab cannot compensate for poor exposures (because the lab processes the film only without going through the additional printing step where adjustments can be made to exposure). The exposure was typically 2 seconds at f/8. See Appendix I for complete exposure information on each D Sight image included. Manual focusing was also used in order to select the optimum depth of field, as well as to focus on the plate or on the retroreflector.

4.2 Equipment

Table 2 lists the equipment that was used for all experimental work.

4.3 Detecting Mode Shape: Experiment 1

4.3.1 Purpose

In order to quickly verify that the Dynamic D Sight images were in fact images of the mode shapes, the node locations were determined by manually feeling the vibrating surface.

4.3.2 Equipment

The setup described earlier was used to capture the Dynamic D Sight images. In order to aid in the feeling of the vibration on the plate, a steel bracket was held to the frame with magnetic clamps, such that the bracket was along the horizontal centre line of the plate with a gap of 13 mm between the bracket and the brass plate. A ruler was placed on the bracket to measure the node locations.

4.3.3 Method

Dynamic D Sight images of the vibrating plate were recorded when it appeared to be in a steady-state condition. This was determined visually by looking at the plate using Dynamic D Sight.

When this was complete, while the plate was still being excited, the bracket was placed along the horizontal centre line of the plate. By touching the plate lightly, the vibration could be felt in the finger tip. Running a finger slowly along the horizontal center line of the plate the node locations could be determined. While the peak to peak amplitude

could not be measured, it is estimated to be 0.1 mm. In any case it is not visible to the naked eye.

Description	ID Number
Stroboscopic Light (General Radio 1538-A, reflector removed)	Mechanical Eng. 95894
35 mm Camera (Canon EOS 10s with 35-135 mm lens)	Personal
Plate Assembly (clamped area of plate is 305 X 305 mm, 0.508 or 0.635 mm thick yellow brass)	Mechanical Eng.
Power Amplifier (Bruel & Kjaer type 2706)	Mechanical Eng. 36959
Frequency Oscillator (Feedback variable phase function generator TWG500)	Electrical Eng. 79205
Speaker (Marsland Linear 'B' 1200 VHP 12" high compliance loudspeaker in 1" thick particle board enclosure)	Personal
Laser, 5 mW Helium-Neon (Melles Griot model 05-LHP-121)	Electrical Eng. S/N 4579YY
Retroreflective Screen (3M Scotchlite, 0.127 mm diameter beads, 900 X 1200 mm)	Mechanical Eng.
Hearing Protection Headphones (Peltor model H7A)	Electrical Eng.
Hot glue gun (Black and Decker butane)	Electrical Eng.
Frequency counter (Fluke 87 true RMS multimeter)	Electrical Eng.

TABLE 2: Experimental Equipment

Where a node could be felt (i.e. no vibration) the position was noted as shown in Table 3. These were then compared to the photographs of the plate taken immediately prior to recording the node locations by feel.

Node	Feel (mm)	Photo (mm)
1	57	53
2	118	104
3	178	168
4	235	230

TABLE 3: Node Locations Across Horizontal Centre Line of Plate

4.3.4 Results

Experiment results are documented in the following figures. In each photograph, the camera was focussed between the plate and the retroreflector such that the depth of field would include them both. Figure 9 shows a view of the plate in the static condition. Roller/stretch marks in the brass plate as a result of the forming process are revealed by the sensitivity of D Sight. Figure 10 and Figure 11 show the vibrating surface at 0° and 180° phase angles respectively, the light and dark areas represent varying slope on the surface of the plate. Figure 12 shows a double exposure of Figure 10 and Figure 11 so that all node locations can be seen simultaneously.

The node occurs at the location where there is a transition from light to dark (or visa versa) in the D Sight image. The double exposed image shows all of the nodes clearly because there is a bright area at the transition from dark to light. Therefore the double exposure shows each node as a bright area.

Measurements were made from the double exposed photograph measuring from the left edge of the image (to compensate for parallax) to the centre of the bright area. These numbers were then scaled to the actual size of the plate. Figure 13 shows the nodal locations detected by feel superimposed on the D Sight image.
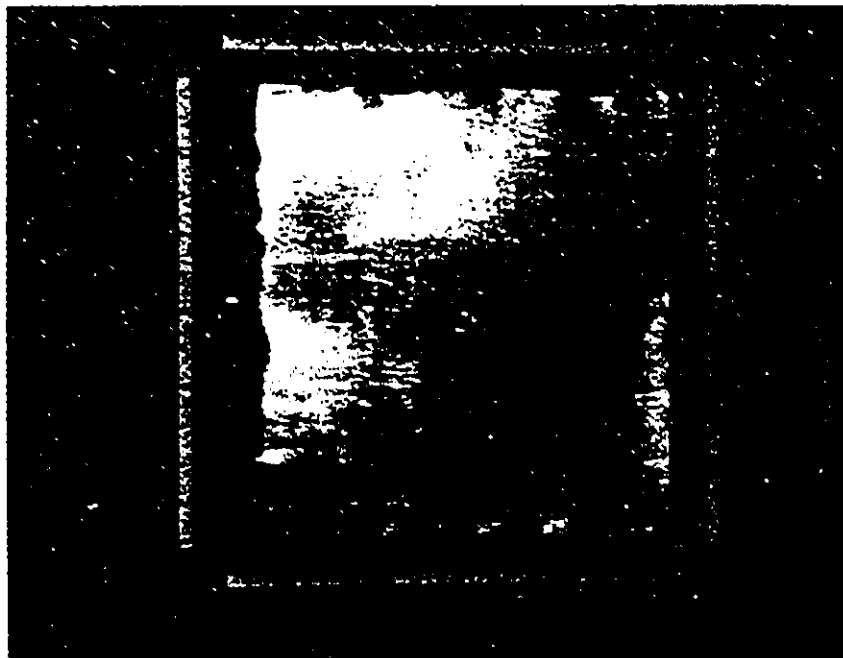
FIGURE 9: Static View of Plate, 10° Angle of Incidence
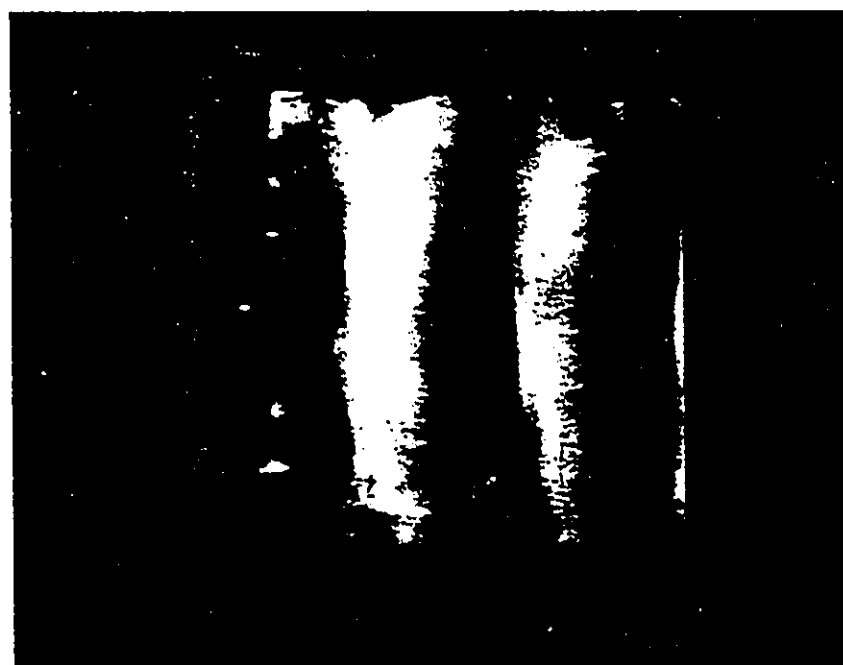
FIGURE 10: Dynamic View of Plate, 400 Hz, 0° Phase Angle

FIGURE 11: Dynamic View of Plate, 400 Hz, 180° Phase Angle
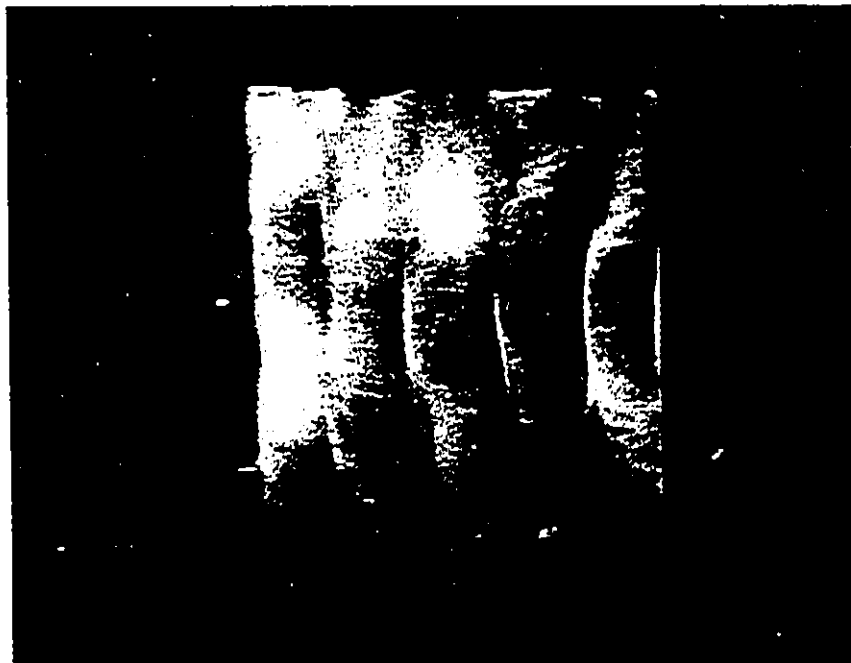
FIGURE 12: Dynamic View of Plate, 400 Hz, Double Exposure

FIGU. :E 13: Nodal Locations Superimposed on D Sight Image

4.4 Detecting Mode Shape: Experiment 2

4.4.1 Purpose

In order to determine if Dynamic D Sight could be used to determine mode shapes, a more quantitative method of finding the nodes was needed. The vibration amplitude was sufficiently great that the vibrations could be felt with the tip of the finger but this proved inaccurate as a method of mapping the nodes and antinodes. Another method needed to be developed.

4.4.2 Equipment

In addition to the Dynamic D Sight image recording, a Helium–Neon Laser was used. A horizontal optical bench was used to move the laser horizontally as well as to

locate its position. For vertical travel, a camera copy stand was used with a tape measure to determine vertical position of the laser.

4.4.3 Method

This method used a laser directed nearly normal to the surface so that the beam would reflect back to the faceplate of the laser, see Figure 14. Where an antinode occurred (maximum displacement, minimum change in slope) there was no deflection of the beam because the slope of the surface did not change. Where a node occurred (minimum displacement, maximum change in slope) the laser beam was deflected the most so a line was seen rather than a point.
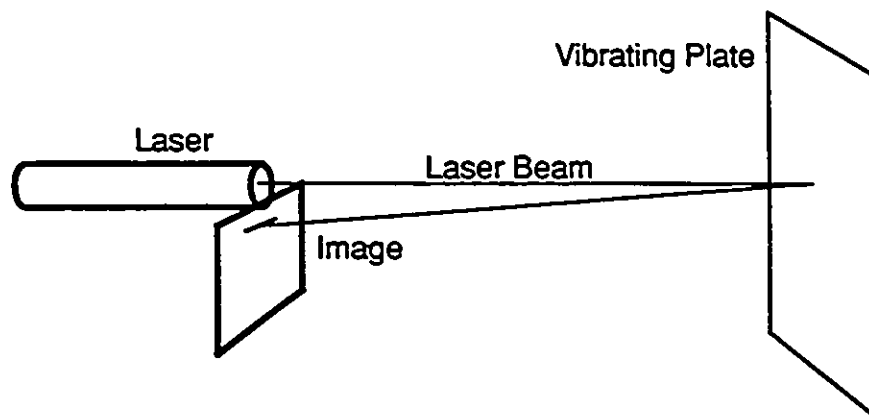
FIGURE 14: Setup to Determine Node and Antinode Locations

Using this technique and scanning across the surface horizontally visually looking for points of maximum (nodes) and minimum (antinodes) deflection, the location of nodes and antinodes was determined. This was repeated in 25 mm increments and the locations were noted. These are shown in Figure 15 which corresponds to Figure 19.

Because the exact point of the maximum deflection was much harder to determine than the minimum, the antinode locations were more reliable than the node locations. This was evident from the erratic shape of the node lines in the above figure. To provide better
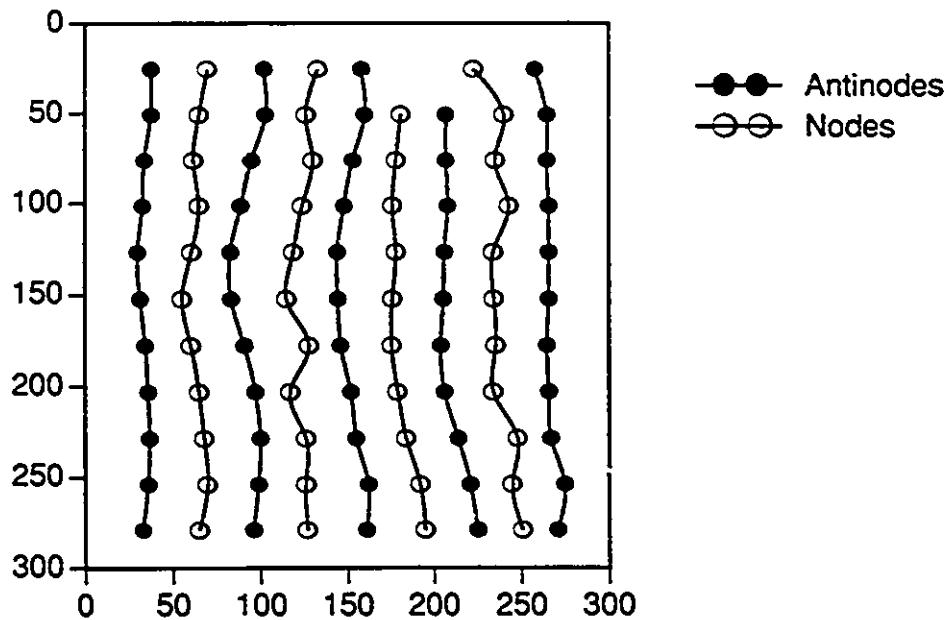
FIGURE 15: Node and Antinode Lines for Figure 19

node lines, node locations were interpolated between antinode locations. This provided smoother node lines as seen in Figure 16. The raw data for these graphs are included in Appendix II.

This experiment was conducted at 317 Hz, providing 4 vertical nodes. There was some vertical deflection of the laser beam indicating vibration in the vertical direction (i.e. horizontal node/antinode lines). The deflection was much smaller in amplitude in the vertical direction (as compared to the horizontal direction) and very erratic when mapping was attempted. Perhaps they were not steady state vibrations.

Figure 17 through Figure 19 show photographs of the dynamic D Sight images. Figure 17 and Figure 18 have a 0° and 180° phase angle and Figure 19 is a double exposure of the first two.
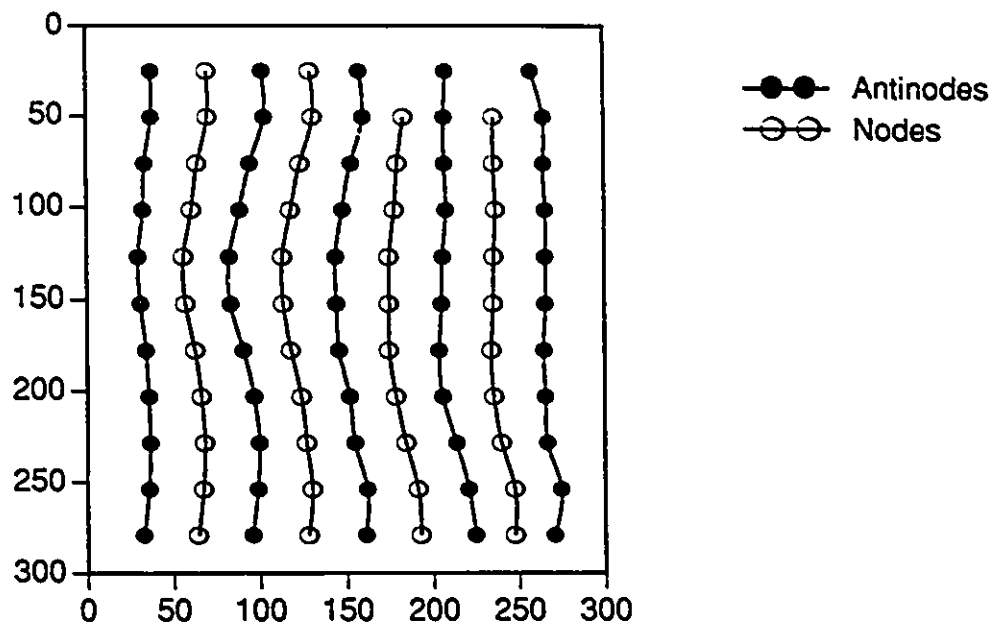
FIGURE 16: Interpolated Node Lines for Figure 19

FIGURE 17: Dynamic D Sight Image 317 Hz, 0° Phase Angle

FIGURE 18: Dynamic D Sight Image 317 Hz, 180° Phase Angle
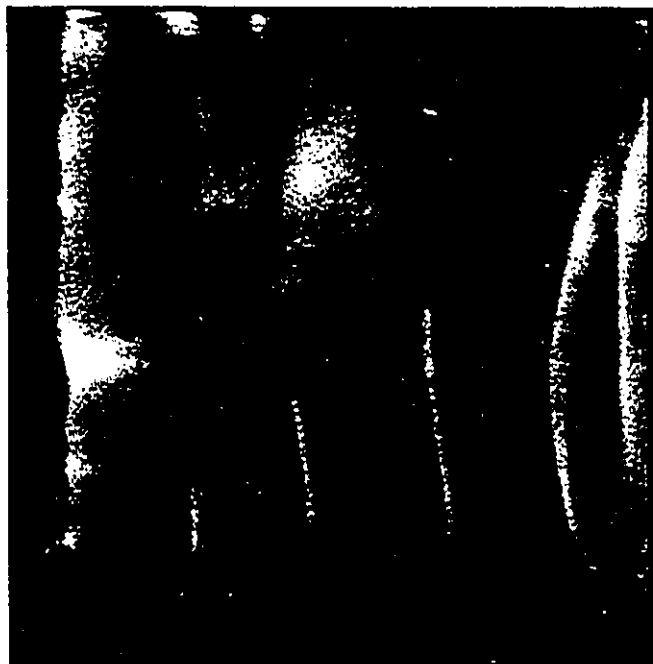
FIGURE 19: Dynamic D Sight Image 317 Hz, Double Exposure

4.4.4 Results

When calculated, the parallax error was determined to be 25 mm. This scaled to 7.3 mm in the photographs. This appears to be slightly larger than the apparent parallax error viewed in the photographs. The node locations (Figure 16) can be overlaid on the double exposure (Figure 19) and the correlation of the node locations is very good.

4.5 Angle of Incidence

4.5.1 Purpose

Experiments were conducted at various angles of incidence from $10°$ to $70°$ in increments of $20°$ to obtain the optimum image and contrast. The closer this angle is to zero the better it is from a geometric point of view because the surface can be seen with a minimum of perspective distortion. $10°$ was about the smallest angle without obstructing the retroreflector with the camera and strobe light.

4.5.2 Equipment

Dynamic D Sight images were recorded in the previously described way. A wire premarked with the distance between the camera and the retroreflector for each angle simplified changing the angle of incidence for each exposure.

4.5.3 Method

Dynamic D Sight images were recorded at $20°$ increments of the angle of incidence from $10°$ to $70°$ (measured from the normal). The plate was excited at a constant frequency of 400 Hz, although the loudspeaker had to be shut off and the plate moved between each exposure. A premarked wire was used to determine the position of the camera, retroreflector, and the plate. The distance from the camera to the plate and from

the plate to the retroreflector were both fixed at 2.0 m. The angle was determined by setting the distance between the camera and the retroreflector. Table 4 shows this distance for each angle.

Angle (degrees)	Distance (m)
10°	0.695
30°	2.000
50°	3.064
70°	3.759

TABLE 4: Distance Between Camera and Retroreflector

Once this distance was set, a wire was suspended over the retroreflector at a fixed location, the same point that was used for the measurement. The plate angle was then adjusted so that the reflection of the wire was running vertically down the centre of the plate as viewed through the camera view finder. Once the positions were set they were double checked using the premarked wire.

4.5.4 Results

Figures 20 through 23 show the effects of increasing the angle of incident illumination on both the image contrast and perspective distortion. The image contrast increased as the angle increased, but because the surface is so bright, even at 10° the image was acceptable. At large angles it becomes more difficult to correlate the D Sight image with points on the surface and a greater amount of the image was lost due to parallax. Steady state resonance is 400 Hz with 0° phase angle in each of these figures.

Since the strobe light is offset from the imaging camera, there is a parallax error between the D Sight image and the actual surface. Figure 24 shows why this happens. This parallax error is dependent on three things:

FIGURE 20: 10° Angle of Incidence
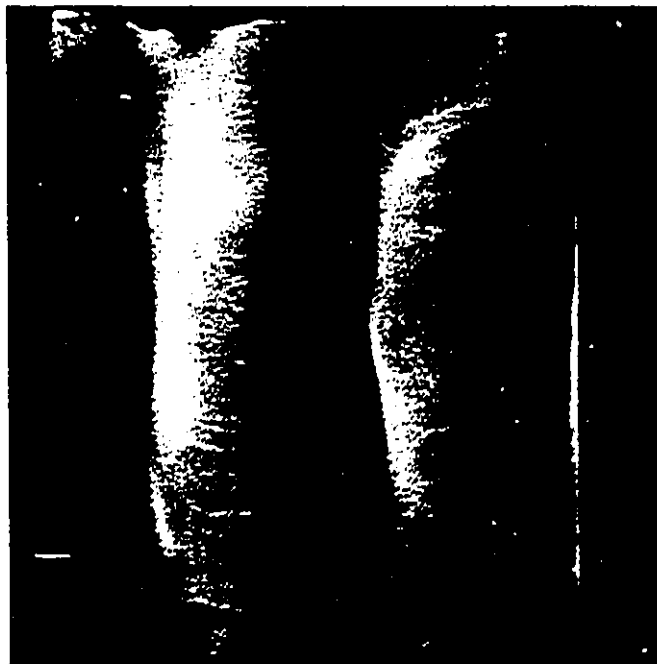
FIGURE 21: 30° Angle of Incidence
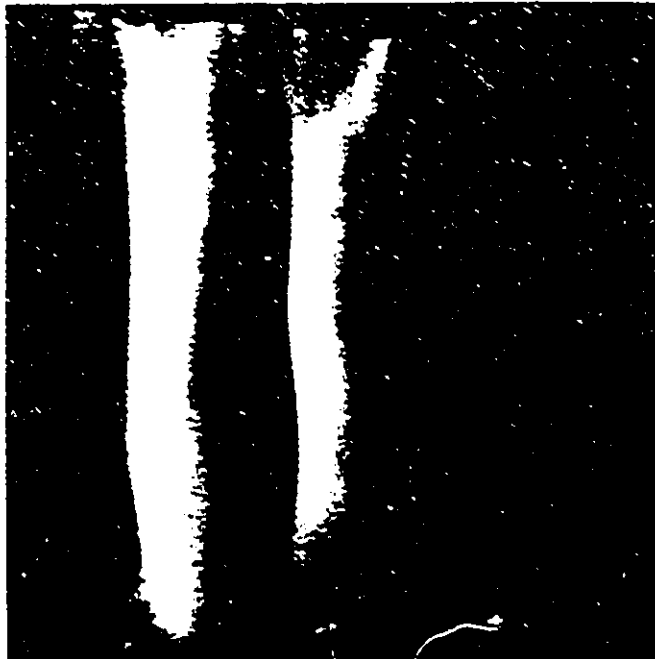
FIGURE 22: 50° Angle of Incidence
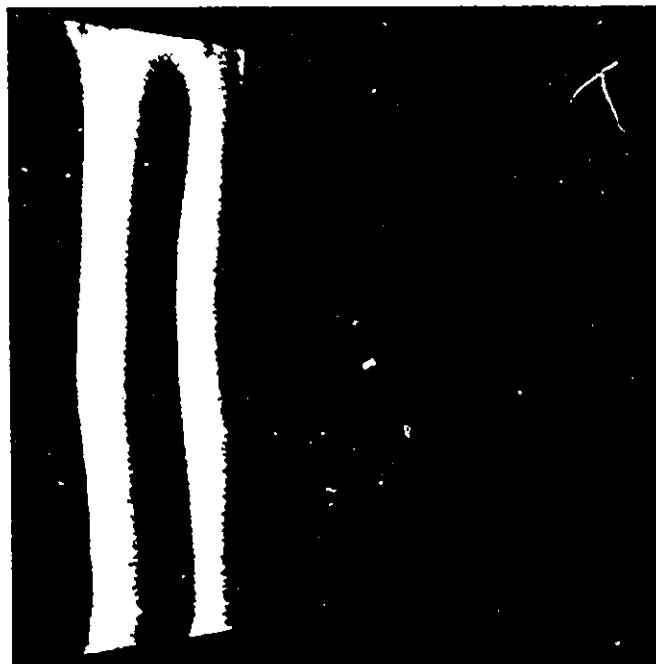
FIGURE 23: 70° Angle of Incidence
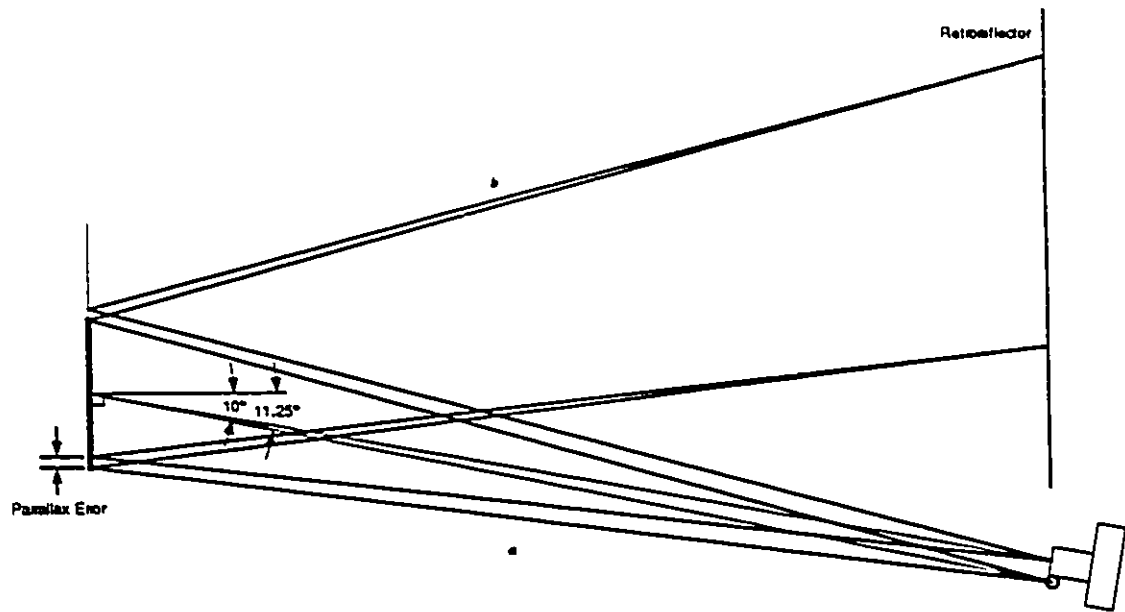
FIGURE 24: Parallax Error

1. Offset distance between imaging lens and the light source. A greater offset causes a larger parallax error.

2. Ratio of the distances between the camera and the object (*a*) and the object and the retroreflector (*b*). The larger this ratio ($\frac{a}{b}$) the less the parallax error will be. See Figure 24.

3. Angle of incidence. The larger the angle of incidence the greater the parallax error.

This results in the dark area on the left of the image and the loss of some of the image on the right of the D Sight images shown. The amount lost is constant when measured parallel to the image (film) plane (as seen in the photographs) but as the angle of incidence increases, this distance will increase in the plane of the plate due to the perspective.

4.6 Finite Element Vibration Analysis

4.6.1 Purpose

The purpose of the Finite Element Analysis (FEA) was to corollate the results of Dynamic D Sight with a theoretical method of determining mode shapes and locations. This also would show what mode shapes and locations are theoretically possible for this physical configuration and help interpret what was detected with Dynamic D Sight.

4.6.2 Equipment

The following software was used to conduct the Finite Element Analysis:

1. SuperDraw II, version 2.24

2. DECODS, version 1.02

3. Algor, version 0.02/387

4. SuperView, version 1.0

5. A custom application written in Think C 5.0.4 on Macintosh to format the data from ALGOR to tab-delineated format for import into DeltaGraph Professional (source code is included in Appendix III).

6. DeltaGraph Professional, version 2.0 (for Macintosh)

4.6.3 Method

The Finite Element Analysis was conducted on an MS-DOS computer using Algor Dynamic Modal Analysis. SuperDraw II was used to enter the two dimensional geometry of the plate and to create the mesh. Decods was used to enter the material properties, thickness (see Table 5), define the 2D plate elements as linear strain with reduced shear, and to convert the data to a format compatible with Algor. Several runs modeling the

whole plate were conducted to determine the sensitivity of the system to the mesh density (i.e. the number of elements).

Property	Value
Density	8.50 g/cm^3
Young's Modulus	96.5 GPa
Poisson's Ratio	0.3
Thickness	0.508 or 0.635 mm

TABLE 5: Material Properties Used In FEA models

4.6.3.1 Quarter Plate Model

Since the plate and its boundary conditions are symmetric about both X and Y centre lines (axes), only one quarter of the plate has to be modeled and proper symmetry and or anti-symmetry boundary conditions applied to the centre lines. A symmetry boundary condition is where the plated is reflected, as in a mirror, about that axis. The values are equal at equal locations on either side of a symmetric boundary. An anti-symmetric boundary condition is where the values are equal but opposite in sign on either side of the axis. Modeling the plate in this manner means that there are four possible sets of boundary conditions:

1. Symmetric about both X and Y-axes.

2. Anti-symmetric about both X and Y-axes.

3. Symmetric about the X-axis and anti-symmetric about the Y-axis.

4. Anti-symmetric about the X-axis and symmetric about the Y-axis.

Since, in this case, the plate is square, cases 3 and 4 will occur at the same frequency as was found in the first modeling of the whole plate, and are therefore redundant. The first three conditions were run, keeping in mind that the symmetric/anti-
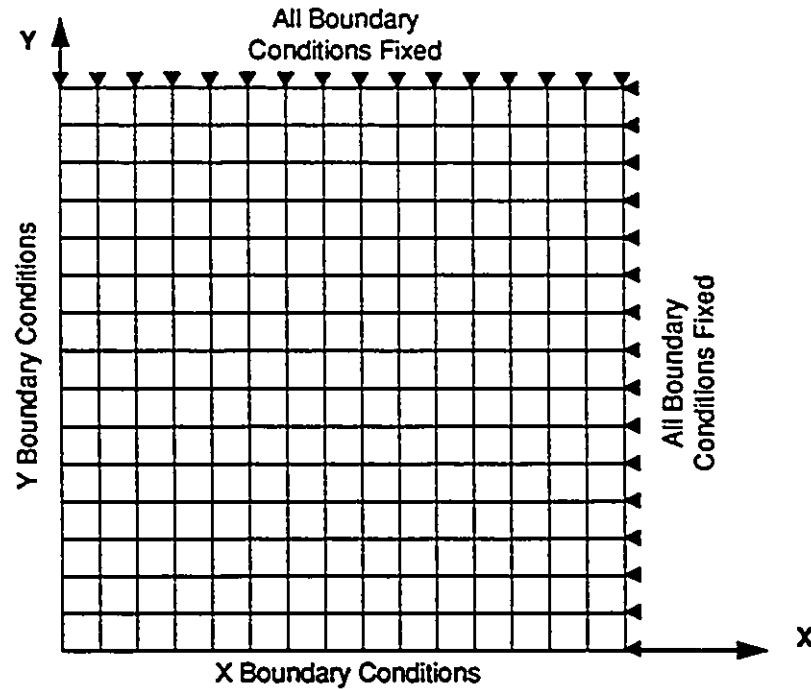
FIGURE 25: Diagram of Quarter Plate for FEA Model

symmetric case has an opposite counterpart (anti-symmetric/symmetric). If the plate were rectangular, all four cases would be required.

The perimeter of the plate has all six boundary conditions fixed (i.e. no translation, no rotation). Table 6 lists the possible boundary conditions for all combinations listed above. The terms tx, ty, and tz refer to translation of that node in the direction specified and rx, ry, and rz refer to rotation at that node about the specified axis. The numbering of these conditions is a convention and they are often referred to by number rather than tx, ty, etc. The centre point of the plate has the fixed boundary conditions for both the X and Y-axis given in the table. An asterisk (*) in the table indicates a condition that is fixed, otherwise it is free to translate or rotate, as the case may be.

Boundary Conditions	X-Axis		Y-Axis	
	Symmetric	Anti-Symmetric	Symmetric	Anti-Symmetric
1) tx		*	*	
2) ty	*			*
3) tz		*		*
4) rx	*			*
5) ry		*	*	
6) rz	*		*	

TABLE 6: Boundary Conditions for Quarter Plate Model

4.6.3.2 Plotting the Results

To print plots of the surface, the data had to be converted to a form that could be read by DeltaGraph Professional (a powerful graphing application for Macintosh). When the entire plate was modeled this was done with a word processor but this became impractical when the quarter plate model was used because the data had to be reflected into the other three quarters of the plate. This task was accomplished by writing a program in C language using Think C compiler. The program read the output file from ALGOR and determined from the file how many elements and mode shapes were present. It then parsed the data and output a tab-delineated text file for each mode, with the data repeated into the other sections of the plate. This data was either symmetric or anti-symmetric (either the same value or the negative of the value). This was determined by the naming convention of the file, which had 'S' or 'A' for its fourth and fifth characters depending on whether the X or Y-axis were symmetric or anti-symmetric. For example 'A15SA.L' is symmetric about the X-axis and anti-symmetric about the Y-axis. ALGOR files must start with a letter, hence 'A' was arbitrarily used, 15 refers to the number of elements in the X and Y direction, and '.L' is the suffix given to the output file by ALGOR. See Appendix III for the code listing.

4.6.4 Results

4.6.4.1 Mesh Density

Various uniform mesh densities were used to model the entire plate and one density was used to model the quarter plate with proper boundary conditions. Natural frequencies for the various mesh densities are given in Table 7. At higher frequencies the system is more sensitive to the number of elements because more nodes will be required to describe the sinusoidal curves of the surface. This means that for higher frequencies, it is more important to have a denser mesh. The processing time increased dramatically as the mesh density was increased, there is a practical limit to how many elements could be modeled. When a model more than 35 elements wide was attempted, the computer ran out of hard disk space, having 46 Megabytes of free space. Since the change in frequency values was small between 30 and 35 elements it was decided that 30 elements would be sufficient to model this plate.

The quarter plate model (15X15) was also included to compare the natural frequencies found with this model. Frequencies marked with a dagger (†) were not calculated but are the same value as the one above due to the symmetry of the plate.

4.6.4.2 Thickness

Models with different thickness were run using a 15X15 element model with symmetric boundary conditions along both the X and Y-axes. The results are plotted in Figure 26 and the raw data is in Appendix II. The variation due to thickness is linear, this can be predicted from the formulas used to find the frequency.

Mode Number	15 X 15 (225 elements)	20 X 20 (400 elements)	25 X 25 (625 elements)	30 X 30 (900 elements)	15 X 15 (Quarter Plate)	35 X 35 (1225 elements)
1	32.03	31.99	31.98	31.97	31.97	31.96
2	65.37	65.28	65.24	65.21	65.21	65.20
	65.37	65.28	65.24	65.21	†	65.20
3	96.84	96.48	96.33	96.26	96.26	96.21
4	117.19	117.03	116.96	116.92	116.92	116.89
5	117.71	117.57	117.50	117.46	117.46	117.44
6	147.87	147.28	146.99	146.84	146.84	146.74
	147.87	147.28	146.99	146.84	†	146.74
7	187.34	187.19	187.10	187.04	187.04	187.01
	187.34	187.19	187.10	187.04	†	187.01
8	198.20	196.98	196.39	196.07	196.07	195.88
9	217.12	216.25	215.80	215.55	215.55	215.40
10	217.86	217.06	216.64	216.40	216.40	216.26
11	267.61	265.76	264.81	264.28	264.28	263.96
	267.61	265.76	264.81	264.28	†	263.96
12	274.54	274.58	274.50	274.44	274.44	274.39
13	274.73	274.79	274.72	274.66	274.66	274.62
14	304.91	304.04	303.48	303.15	303.15	302.95
	304.91	304.04	303.48	303.15	†	302.95
15	337.11	334.19	332.59	331.70	331.70	331.16

TABLE 7: Natural Frequencies for various mesh densities

$$f = \sqrt{\frac{k}{m}}$$

where $k \propto t^3$

and $m \propto t$

therefore $f \propto \sqrt{\frac{t^3}{t}} = \sqrt{t^2} = t$.

In the FEA solution k and m are actually matrices, but the effect is the same.
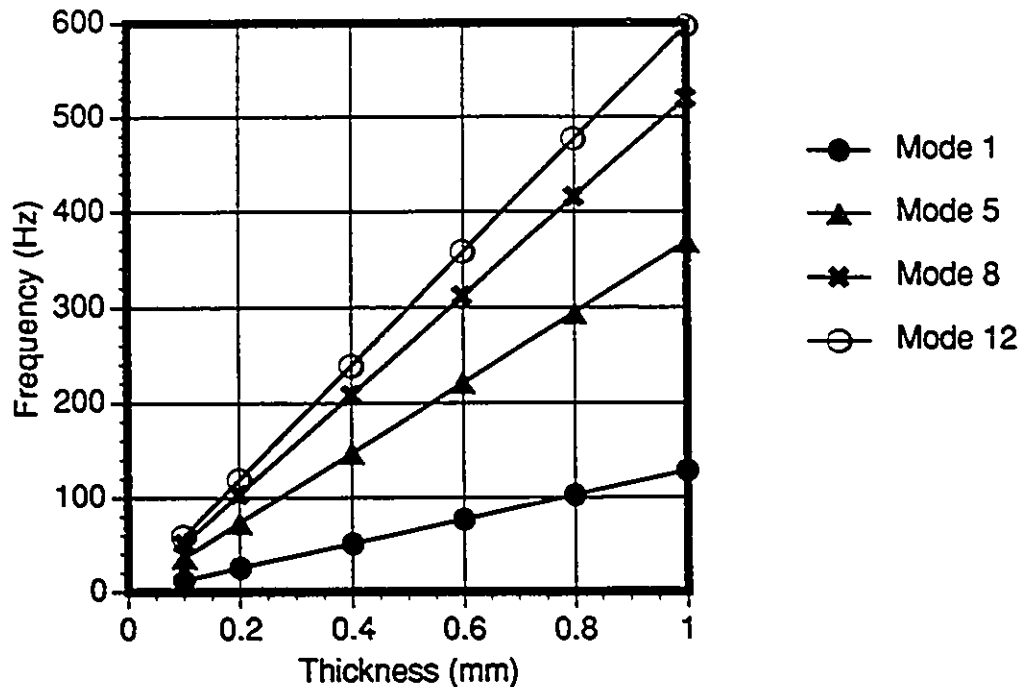
FIGURE 26: Graph of Various Thickness Values in the FEA model

4.6.4.3 Correlation to Experimental Results

For this experiment a 0.635 mm brass plate was used in the same clamping frame as the other experiments. The strongest mode shapes were located and photographed for comparison to the FEA results.

Many of the mode shapes from the FEA model could not be found experimentally. FEA does not give the relative amplitudes between each mode.[12] This is because the equations do not have enough data for a complete solution. When the amplitudes are solved, an arbitrarily value is used for the first node and the rest of the nodes are solved relative to it. This means that there is no cross-reference between mode shapes and, although a mode shape may look very impressive, the actual amplitude may be negligible.

On the other hand there were several mode shapes found experimentally that were not part of the FEA solution. Many runs, trying different mesh densities (to avoid aliasing) and using the known symmetry conditions, did not reveal any of the missing modes.

Mode 1 was not detected with Dynamic D Sight because D Sight is not sensitive to gentle slopes. In these cases the plate had a very uniform gentle slope, it was not until the higher modes that there was enough local slope for D Sight to detect.

Table 8 shows a comparison of some frequencies which showed up very clearly in the experimental work and the FEA frequencies for the same mode shapes, where they exist. The mode shape notation refers to the number of half waves in the X and Y directions, therefore (5,1) has 5 half waves in the X direction and 1 half wave in the Y direction. This notation was used by **Hazell and Mitchell**[13] as well as **Montrose** to describe the shape of the mode. This notation works very well for the modes which are rows of the same number of half waves. In the FEA some of the modes do not follow this pattern (for example Modes 4, 5, 9, 10).

The Dynamic D Sight images and the corresponding FEA contour plots are shown in Figures 27 to 32 for the images with good correlation. Since the D Sight images relate to curvature of the surface and the contour plots relate to the amplitude, the comparison is not directly obvious. However, since curvature is the second derivative of displacement and the surface is approximately a sine wave, and the second derivative of a sine wave is also a sine wave (of opposite magnitude), the comparison works. In the Dynamic D Sight image the dark represents convex areas and light represents concave areas. The node locations are at the interface between light and dark areas. Figure 32 shows the node locations from the FEA contour plot extrapolated onto the Dynamic D Sight image.

Experimental Frequency (Hz)	Mode Shape	FEA Mode	FEA Frequency (Hz)	Exp Freq/ FEA Freq (%)
60.82	(2,1)	2	81.51	75
110.43	(5,1)	12	343.04	32
117.67	(4,5)	21	522.16	23
125.16	(3,1)	5	146.77	85
140.22	(2,2)	3	120.32	117
223.4	(3,3)	8	245.09	91
295.9	(3,5)	18	474.52	62
301.5	(5,1)	12	343.04	88
306.0	(4,3)	11	330.92	93
312.2	(5,1)	12	343.04	91
332.0	(1,5)	13	343.04	97
351.4	(2,5)	14	378.90	93
367.6	(2,5)	14	378.90	97
420.2	(3,5)	13	343.32	122
594.4	(6,1)	18	474.52	125
596.1	(5,5)	23	627.69	95
616.5	(6,7)	45	1029.83	60

TABLE 8: Experimental and FEA Frequencies Compared

Other Dynamic D Sight images are in Appendix IV. Three dimensional surface plots and contour plots from the FEA data are included in Appendix V for the first 50 modes.

4.6.5 Error Analysis

The frequencies found using Dynamic D Sight varied from 23 to 125% (a typical value being about 90%) of the values found by FEA. Since the frequency of the plate was not directly measured it may be that the plate was vibrating at a frequency different than the excitation frequency of the function generator. Another important factor is that the material properties and boundary conditions are most certainly different than the ideal values used by FEA. This can be shown by the fact that roller/stretch marks are clearly

visible in the static D Sight images of the plate. This would introduce different physical properties in the horizontal and vertical directions on the plate.

Since the node locations in the Dynamic D Sight images are in a grey scale transition from light to dark, it should be possible to calibrated the exact location of the nodes for a particular set up and equipment. The small difference shown here is probably due to the difference in material properties and boundary conditions mentioned above.

As shown in Figure 33 the node location predicted by FEA is a straight line, however the plate appears to have non-linear influences causing the node location to shift slightly. Table 9 shows node values at a few points on the plate. The first two points were selected along the centre line and the third is the worst case. This shows a worst case difference of less that 5% difference between the FEA solution and the D Sight node locations.

Point	FEA node (mm)	D Sight node (mm)	%Δ
1	104.1	107.0	2.8
2	151.2	146.1	-3.4
3	104.1	99.3	-4.6

TABLE 9: Node Locations From Left Edge of Plate

4.7 Theoretical Solution

4.7.1 Purpose

A theoretical solution would provide a correlation for both FEA and Dynamic D Sight. Blevins[14] provides an approximate theoretical solution to find frequencies for plate vibrations.
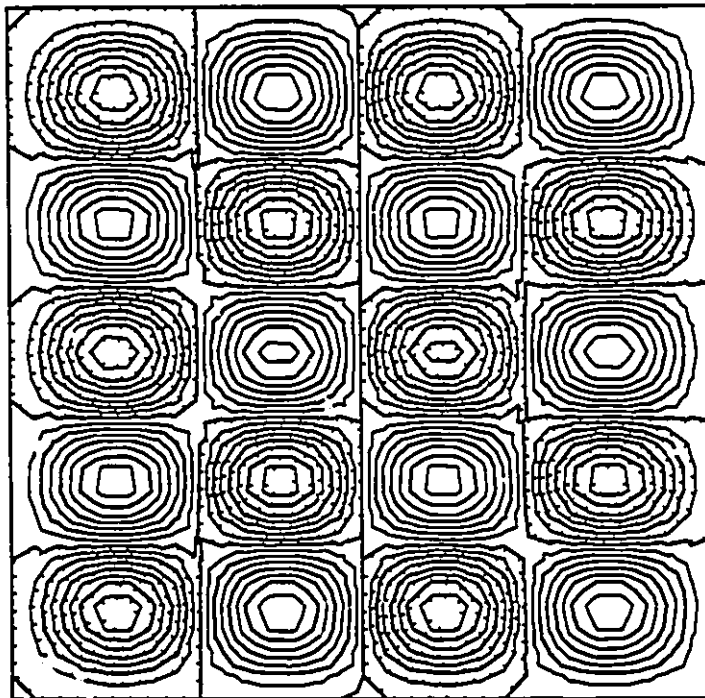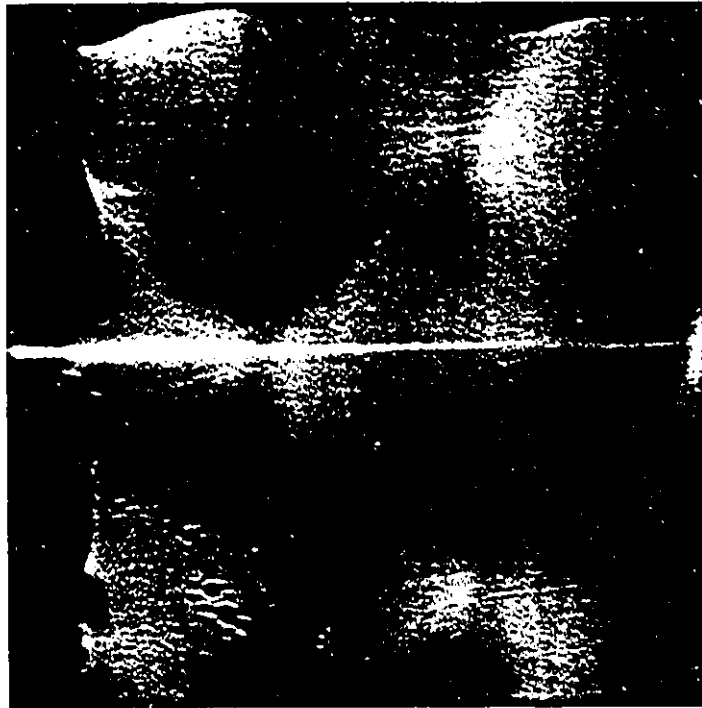
FIGURE 27: Mode Shape (4,5) Top: D Sight Image, Bottom: FEA Contour Plot
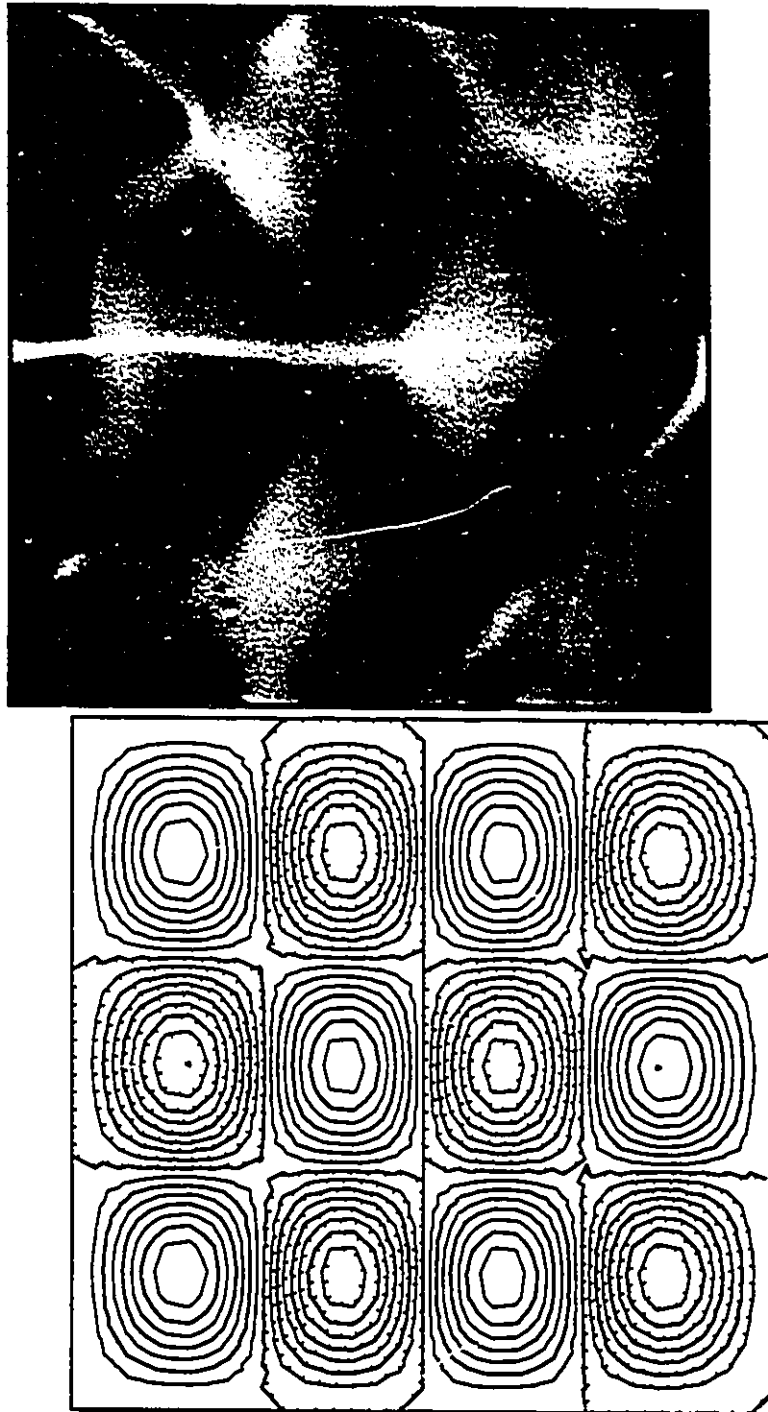
FIGURE 28: Mode Shape (4,3) Top: D Sight Image, Bottom: FEA Contour Plot
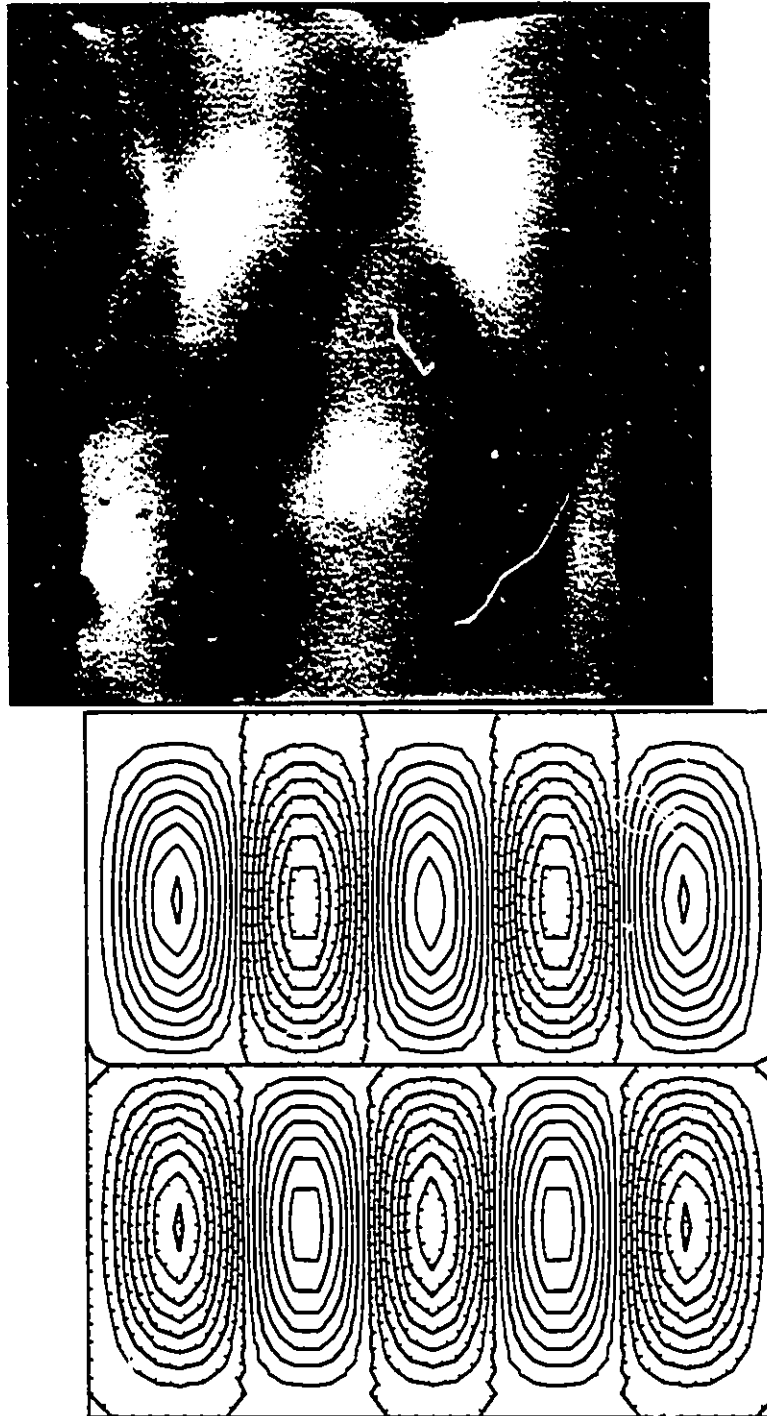
FIGURE 29: Mode Shape (5,2) Top: D Sight Image, Bottom: FEA Contour Plot
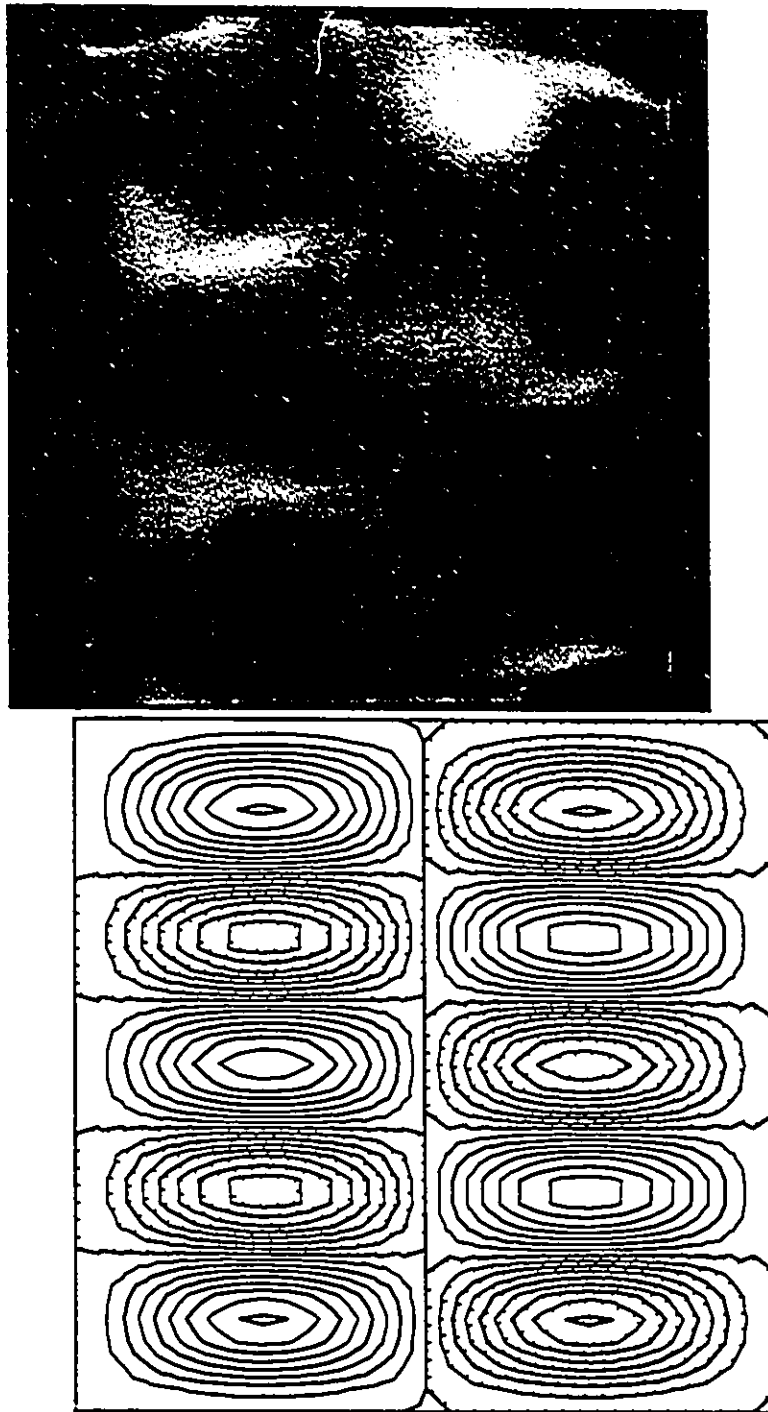
FIGURE 30: Mode Shape (2,5) Top: D Sight Image, Bottom: FEA Contour Plot
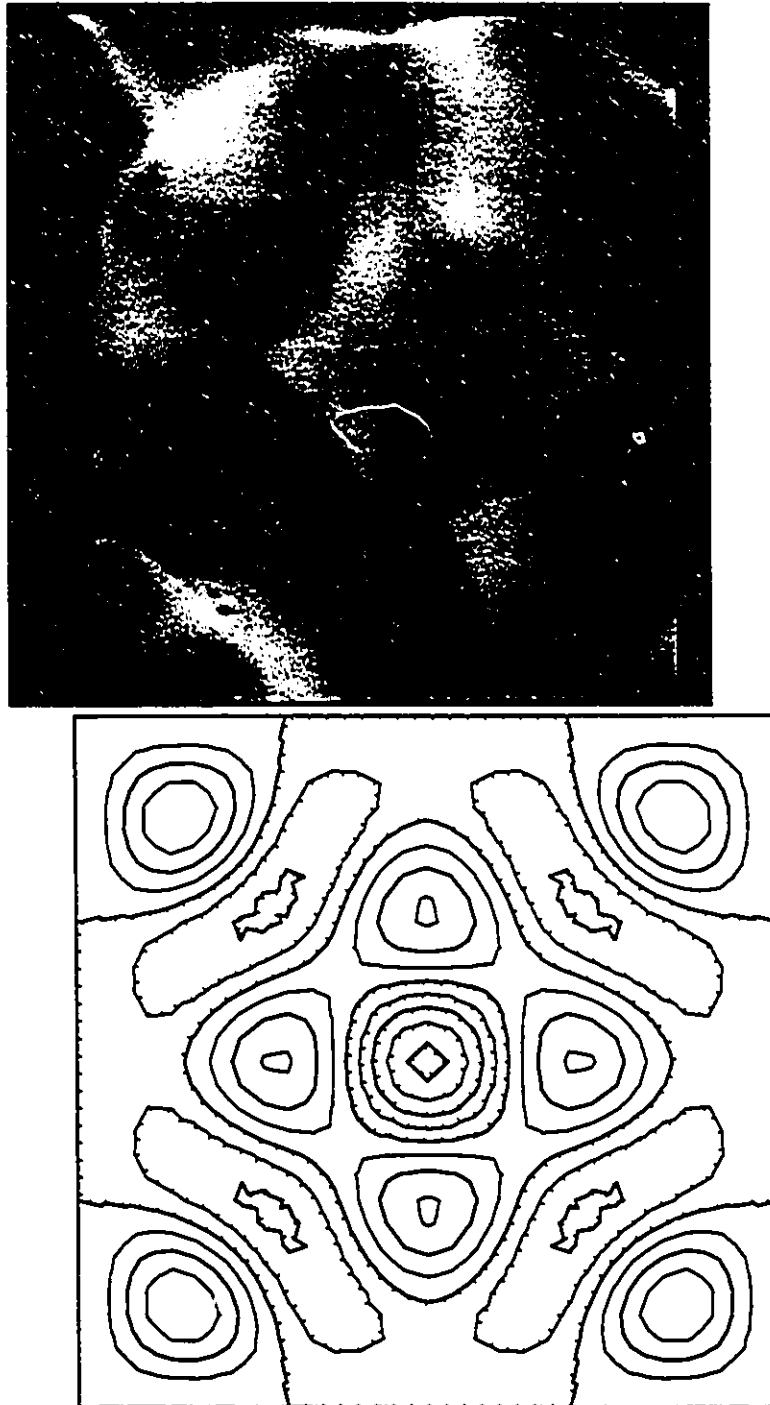
FIGURE 31: Mode Shape (3,5) Top: D Sight Image, Bottom: FEA Contour Plot
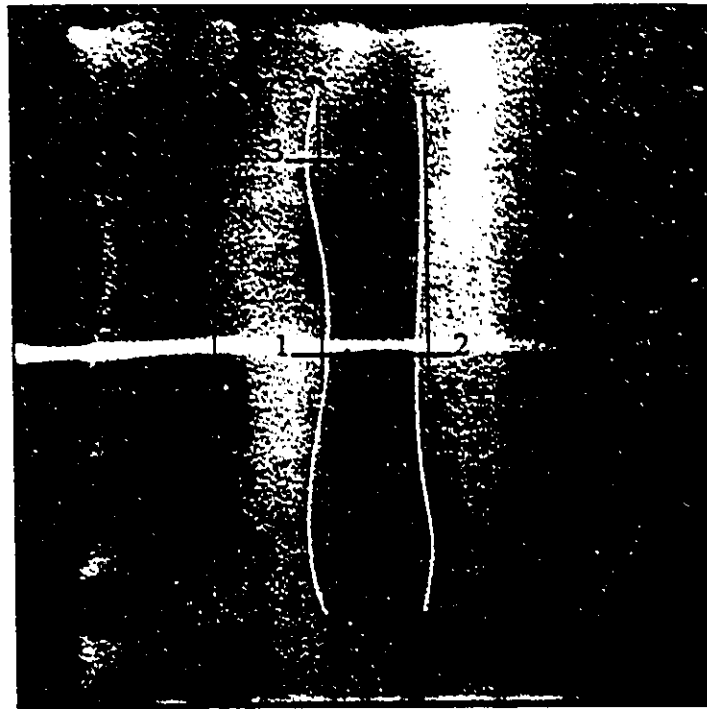
Node lines
extrapolated
from FEA
contour plot
shown in black.

D Sight nodes
shown in white.
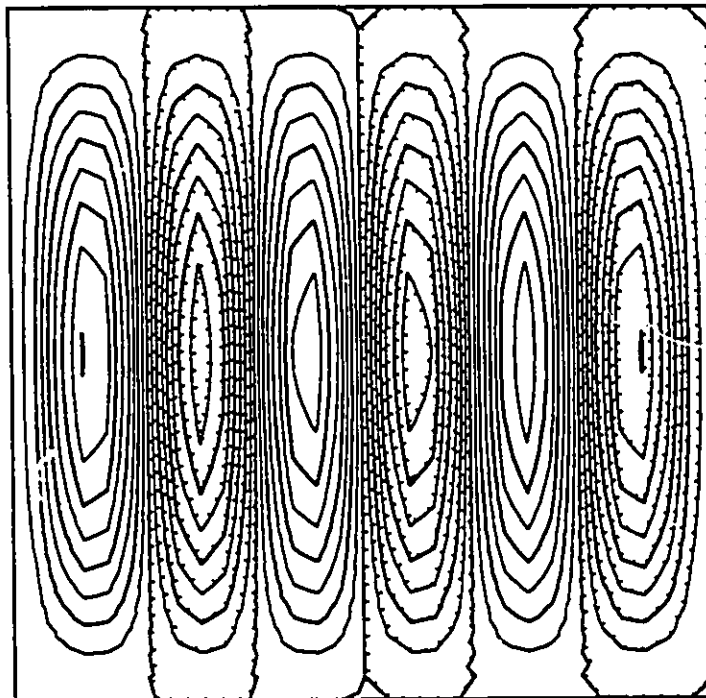
FIGURE 32: Mode Shape (6,1) Top: D Sight Image, Bottom: FEA Contour Plot

4.7.2 Method

Blevins gives the approximate frequency solution formula as:

$$f_{ij} = \frac{\pi}{2}\left[\frac{G_1^4}{a^4} + \frac{G_2^4}{b^4} + \frac{2J_1J_2 + 2v\,(H_1H_2 - J_1J_2)}{a^2b^2}\right]^{1/2}\left[\frac{Eh^3}{12\gamma(1-v^2)}\right]^{1/2}$$

Where:

$i = 1, 2, 3..., j = 1, 2, 3...$

$G = G_1, H = H_1, J = J_1$ for mode index $= i$ for Y-axis and

$G = G_2, H = H_2, J = J_2$ for mode index $= j$ for X-Axis

For a plate clamped on all sides:

$G=1.506$ for mode index $n = 1$ and $n+\frac{1}{2}$ for mode index $n > 1$

$H=1.248$ for mode index $n = 1$ and $\left[n+\frac{1}{2}\right]^2\left[1-\frac{2}{(n+\frac{1}{2})\pi}\right]$ for mode index $n > 1$

$J = H$.

This leads to the simplification of the equation for a square plate clamped on all sides since $J = H$, therefore the term $2v(H_1H_2 - J_1J_2) = 0$ and also $a = b$ the equation simplifies to:

$$f_{ij} = \frac{\pi}{2a^2}\,[G_1^4 + G_2^4 + 2H_1H_2]^{1/2}\left[\frac{Eh^3}{12\gamma(1-v^2)}\right]^{1/2}$$

The physical properties used in this calculation are given in Table 10. The values calculated are given in Table 11 with FEA values for comparison.

Property	Symbol	Value
Length	a, b	0.305 m
Young's Modulus	E	96.5×10^9 Pa
Thickness	h	0.508×10^{-3} m
Mass per unit area	γ	4.318 kg/m^2
Poisson's Ratio	v	0.3

TABLE 10: Properties Used for Approximate Frequency Solution

4.7.3 Results

According to **Blevins** there is no general closed-form solution for mode shapes. In his discussion of mode shapes he points out that all mode shapes for i and j do not necessarily exist. Also "the intertwining of the deformations along the two axes can produce complex and fanciful geometric nodal patterns..."[15] This would explain why some mode shapes are missing from the FEA solution. If fact, an example that he gives is for (1,3) and (3,1) node locations for a completely free plate. While this may not relate to a clamped plate, the shapes are the same as FEA modes 4 and 5 (see Figure 33) which coincide with the frequencies found for (1,3) and (3,1) using the approximate theoretical method. Therefore, the more complex looking modes may in fact be straight forward (i, j) modes

A curious effect is that Dynamic D Sight detects mode (1,5) very clearly (see Figure 13 on page 18 while the corresponding FEA mode 12 or 13 (see Figure 34) is much different looking.

4.8 Debonding: Cross-Brace

4.8.1 Purpose

The purpose of the cross-brace experiment was to determine if Dynamic D Sight can detect debonding in layers of laminated materials.
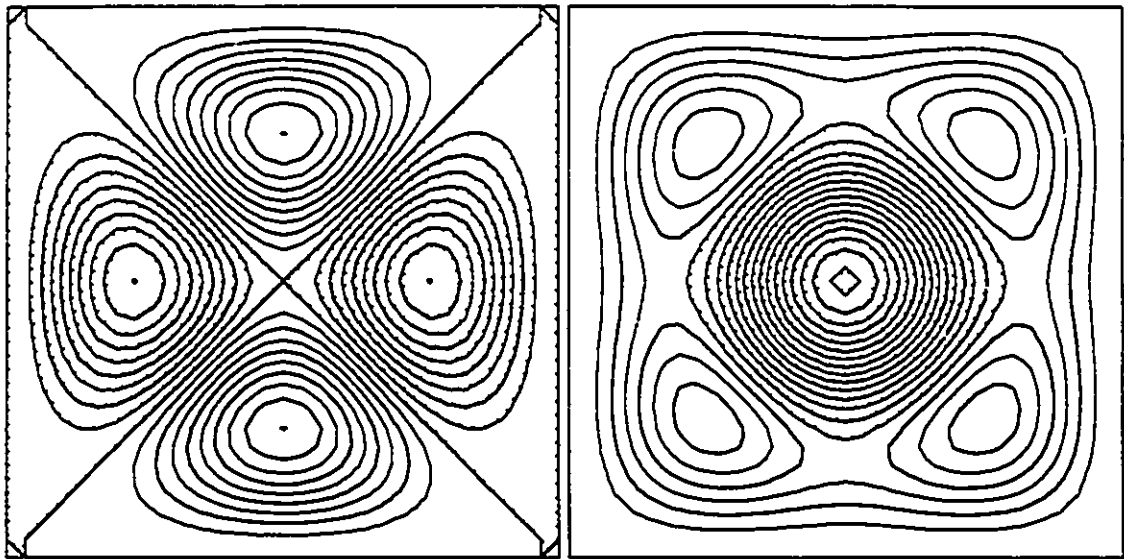
Mode 4   Mode 5

FIGURE 33: Contours which Correlate to Mode Index (1, 3) and (3, 1)
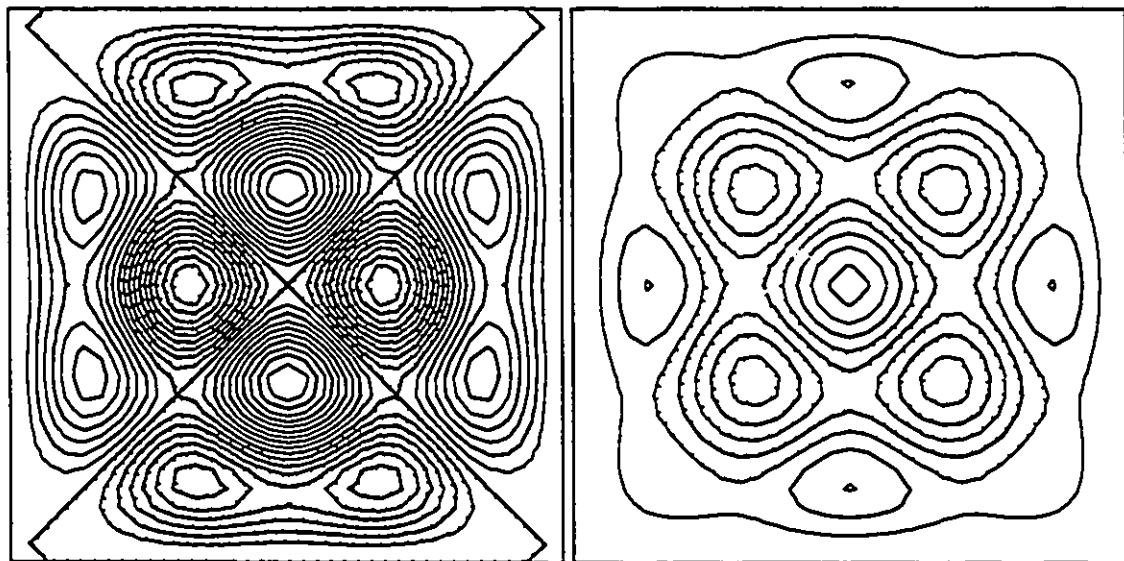
Mode 12   Mode 13

FIGURE 34: Contours which Correlate to Mode Index (1, 5) and (5, 1)

i	j	Frequency (Hz)		Mode
		Theoretical	FEA	
1	1	32.02	31.96	1
1	2	65.35	65.20	2
2	1	65.35	65.20	
2	2	96.42	96.21	3
1	3	117.42	116.89	4
3	1	117.42	117.44	5
2	3	147.01	146.74	6
3	2	147.01	146.74	
1	4	187.30	187.01	7
4	1	187.30	187.01	
3	3	195.77	195.88	8
2	4	216.21	215.40	9
4	2	216.21	216.26	10
3	4	263.64	263.96	11
4	3	263.64	263.96	
1	5	274.78	274.39	12
5	1	274.78	274.62	13
2	5	303.40	302.95	14
5	2	303.40	302.95	
4	4	330.12	331.16	15

TABLE 11: Frequency Comparison for Theoretical Solution

4.8.2 Equipment

The same equipment was used in this experiment but the brass plate was replaced with a 0.502 mm brass plate with an aluminum cross-brace, shown in Figure 35, fixed to the back of it with double sided tape.

4.8.3 Method

The plate was mounted in the same frame as was used previously. It was then acoustically excited and viewed with Dynamic D Sight. Various frequencies and phase angles were used to study the effect.
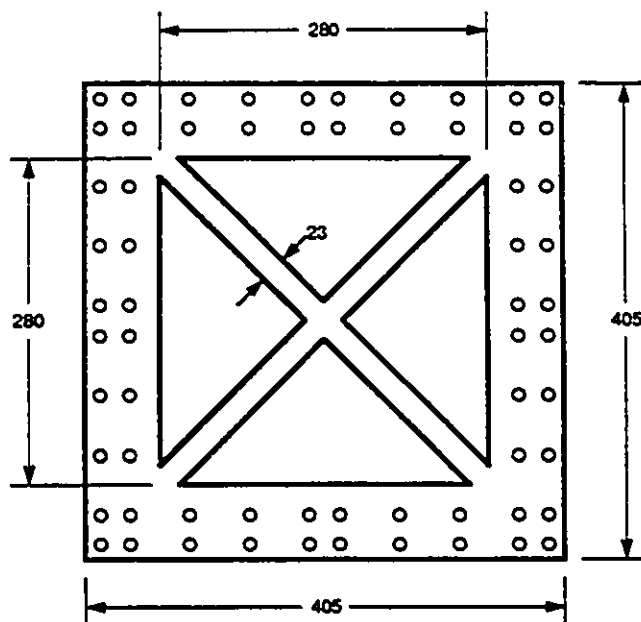
FIGURE 35: Diagram of Brace Used for Debonding Experiment

4.8.4 Results

Figure 36 shows a static photograph of the plate. The X-brace can be seen with static D Sight because of the distortion of the surface caused by the X-brace being attached. Debonding is apparent even in the static condition. Figure 37 shows the dynamic image of the plate. The best results were achieved in the range of 240 to 300 Hz. In the dynamic pictures an area of debonding along both arms is clearly enhanced.

4.9 Debonding: Point Contact

4.9.1 Purpose

This experiment was to determine if Dynamic D Sight could be used to detect a point bond with the vibrating surface such as might be the case in a spot weld.

FIGURE 36: Static View of Plates With Cross-Brace

FIGURE 37: Dynamic View of Plate With Cross-Brace

4.9.2 Equipment

For this experiment the clamping frame was modified to accommodate a bracket across the back to hold a contact rod. Four pairs of holes were drilled and tapped into the frame to allow the bracket to be located in four different vertical positions. The bracket, in turn, had four holes with set screws to allow the contact rod to be placed in four different horizontal positions. This arrangement meant that the contact rod could be placed in 16 locations in one quarter of the brass plate. Figure 38 shows a photograph of the bracket and Figure 39 shows a closer view of the contact rod in the bracket.

FIGURE 38: Bracket on Mounting Frame

4.9.3 Method

For each location of interest the contact rod was glued, using hot melt glue, to the back surface of the brass plate. This allowed for quick setup and the glue came off cleanly by twisting the contact rod.
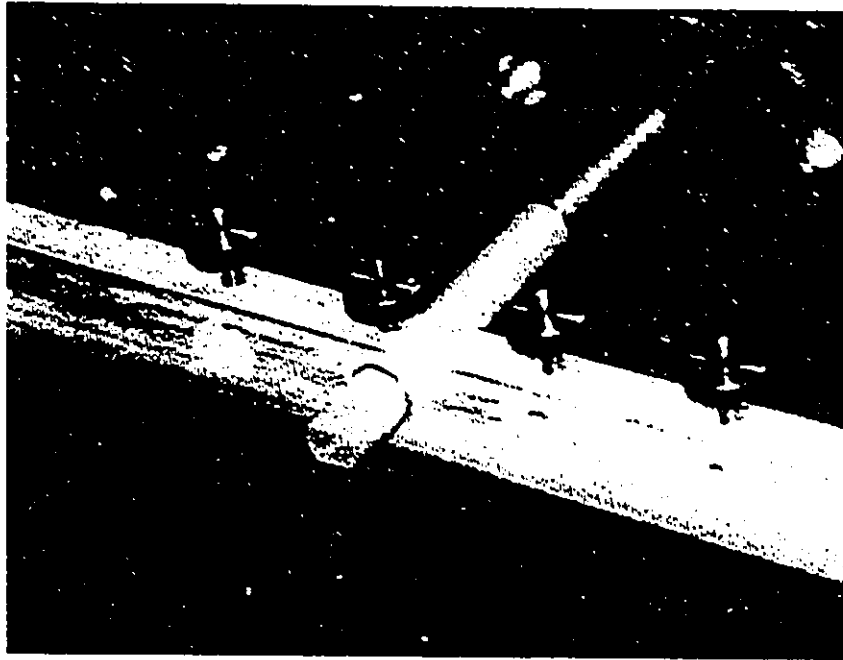
FIGURE 39: Close-up of Contact Rod In Bracket

The plate was then vibrated at various frequencies and phase angles to find the combinations that indicated a standing wave pattern on the plate.

4.9.4 Results

When the contact rod was glued to the plate the point of contact could be seen clearly with static D Sight, as shown in Figure 40. When vibrated at a natural frequency the point of contact clearly shows as a dark spot in the Dynamic D Sight image. Figure 41 shows the plate vibrating at 302 Hz, 0° phase angle and Figure 42 shows the same frequency at 180° phase angle.
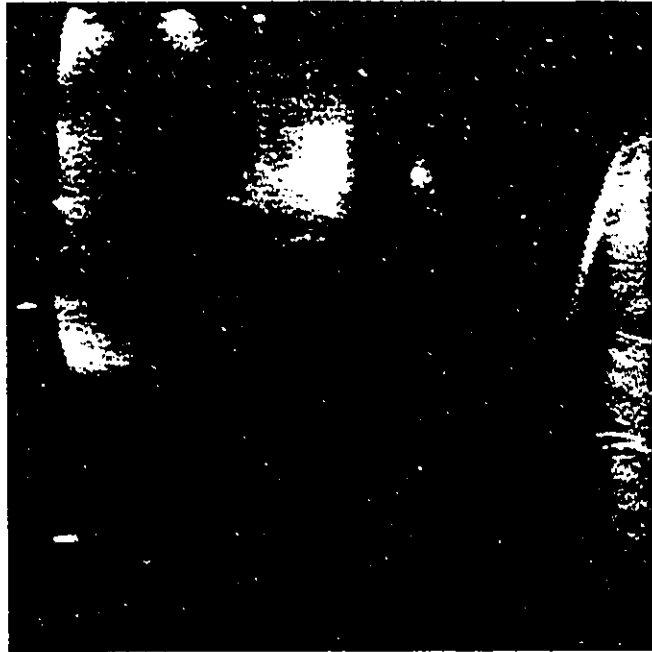
FIGURE 40: Point Contact, Static

FIGURE 41: Point Contact, 302 Hz

FIGURE 42: Point Contact, 340 Hz

Summary

5.1 Mode Shape Detection

From the results of the first two experiments it can be concluded that Dynamic D Sight can be used to determine mode shapes and node locations. In the single exposure photographs, which are the same as what an observer would see, the dark areas indicate convex areas and the bright areas indicate concave areas. The antinode locations lie in this region. The node locations appear at the transition between light and dark areas.

Similar investigations have been carried out using holographic interferometry as this also yields full field information. However holography cannot be done in real time, as is the case for Dynamic D Sight. Holography requires a large multiple pulsed laser which can cost $200,000. Such high power lasers are also dangerous to the human eye. Nor can holographic results be viewed in real time to pick the optimum or significant events. Holographic interferometry does however yield displacement information, whereas

D Sight yields curvature information. Both methods have similar sensitivity to small changes.

Because Dynamic D Sight is inexpensive, easy to use and gives full field results it would be ideal to investigate the response of automobile doors, hoods, panels subjected to typical road excitation. These panels, when painted are very reflective and would quickly demonstrate the change in signature if a given zone is reinforced or otherwise constrained to reduce vibration amplitude and the resulting noise created by such vibrations.

Similar applications would occur in aircraft, passenger trains, trucks, boats, and a host of other industries where plate vibrations result in noise and fatigue.

5.2 Angle of Incidence

The ideal case would be to view the surface at normal incidence. This would eliminate any perspective distortion of the surface and allow easier correlation of the nodes with their surface location. Also, the parallax error decreases as the angle of incidence decreases because the projected distance on the surface decreases.

Unfortunately this is not possible because the camera and strobe light would be reflected in the surface and would obstruct the path to the retroreflector.

The angle of incidence experiment shows that the contrast of the image increases as the angle of incidence increases but because the surface was so bright the images were very useful even at 10° to the normal. This meant that the object could be viewed at near normal angles so there was little perspective distortion.

Compensation for parallax error is necessary and can be calculated from the geometry or determined by the dark area at the edge of the object.

5.3 Finite Element Vibration Analysis

The FEA did corollate quite well with the experimental work for the frequencies that were found. However, some of the frequencies found experimentally were off by a factor of 2, 3, and even 4 as compared to the FEA results. It could be that the plate vibrated at multiples of the excitation frequency.

Node locations from Dynamic D Sight can be determined within 5% of the value from the FEA results. Neither FEA nor D Sight predict the amplitude of the vibration. As the FEA model is a highly idealized representation of the "real" plate used in these experiments, the true discrepancies are unknown. Some of the vibrating modes were found to be very delicate and can easily be influenced by small variations.

5.4 Theoretical Method

The theoretical method provided confidence in the FEA results since the frequencies determined by both methods were very close. It also provided some insight into why some modes appeared to be missing from the FEA results. These were found to appear quite different than would be expected from the mode index (i, j) numbers.

5.5 Debonding

In both of the debonding experiments the debonds were visible with static D Sight. In the cross-brace experiment the use of Dynamic D Sight significantly enhanced the image of the debonds so that they could clearly be identified. In the point contact experiment the anchored point has a signature similar to a surface flaw but when viewed with Dynamic D Sight it could be seen that it was not vibrating with the surface of the

plate. Both cases showed that the mode shapes and locations of the plate were dramatically distorted.

It appears that both types of bonds can be identified using Dynamic D Sight. This may have application in adhesive bonds of the X-brace to an automobile hood or trunk lid or to spot welds or spot adhesive bonds in similar reinforcements.

Similarly, subsurface debonds may be excited acoustically or mechanically to yield a Dynamic D Sight signature. Examples may include rubber to casing debonds in automobile tires, debonds in fiber reinforced plastics used in aircraft airfoils as a result of impact damage, laminated wood construction, etc.

Conclusions

6.1 Mode Shape Detection

1. Dynamic D Sight can be used to determine mode shapes and node locations. The node locations appear at the transition between light and dark areas.

6.2 Angle of Incidence

2. Both contrast of the image and perspective distortion increases as the angle of incidence increases. Because the surface was so bright, the images were very useful even at a 10° angle of incidence. This meant that the object could be viewed at near normal angles to minimize perspective distortion.

3. Compensation for parallax error is necessary and can be calculated from the geometry or estimated by the dark area at the edge of the object.

6.3 Finite Element Vibration Analysis

4. Experiments showed that Dynamic D Sight can predict the steady state frequency within 10% of the FEA result.

5. Dynamic D Sight will predict node location within 5% of the location predicted by FEA.

6.4 Theoretical Method

6. The theoretical method provided confidence in the FEA results since the frequencies determined by both methods were very close. It also provided some insight into why some modes appeared to be missing from the FEA results. These were found to appear quite different than would be expected from the mode index (i, j) numbers.

6.5 Debonding

7. Dynamic D Sight significantly enhanced the image of the debonds so that they could clearly be identified.

Recommendations

Some possible extensions to this research could include the following:

1. Use a high speed video camera with a continuous white light source to capture the D Sight image. This would allow viewing the D Sight image in slow motion. An added advantage would be that an impulse excitation could be used and the resulting decay could be observed.

2. Use a computer to interpret the image. Although direct amplitudes would be difficult to determine, the boundaries of the mode shape and perhaps a contour plot of the surface could be produced.

3. Attach an accelerometer to the plate to make sure the plate is vibrating at the same frequency as the excitation frequency. This may help find the natural frequencies more accurately since the amplitude of the vibration could be monitored to determine when it reaches a maximum.

References

1. Karpala, Frank, and Clarke, Don, <u>A Study to Recover Surface Contour Information from D Sight,</u> Final Report for National Research Council of Canada, Diffracto Limited, (July 1989).

2. Pryor T.R., Reynolds, R, Pastorius, W, <u>D Sight™: A Whole-Field Optical Technique for Determination of Surface Form Deviation,</u> Surface Topography, Vol 1, Issue 3, September 1988, pp. 338.

3. ibid. pp. 340.

4. Clarke D.A., Reynolds R.L., and Pryor T.R., <u>Panel Surface Flaw Inspection,</u> U.S. Patent No. 4629319, (December 16, 1986).

5. Heywood, J., <u>D Sight Measurement of Waviness for Process Control,</u> Proceedings: D Sight Second Annual Symposium, 1991.

6. Austin, D., Barrett, B., <u>D Sight at Ogihara of America Corporation Practical Examples and Uses,</u> Proceedings: D Sight Second Annual Symposium, 1991.

7. Komorowski, J.P., Gould, R.W., Pastorius, W.J., <u>A Technique for Rapid Inspection of Composite Aircraft Structure for Impact Damage.</u> Conference Proceedings No. 462. pp. 11-1.

References

8. Komorowski, J.P., Simpson, D.L., Gould, R.W., <u>Enhanced Visual Technique for Rapid Inspection of Aircraft Structures</u>, Materials Evaluation, December 1991. pp. 1486.

9. Reynolds, R.L., <u>Defining a Standard for Surface Waviness</u>, Proceedings: D Sight Second Annual Symposium, 1991.

10. Montrose, Cameron, <u>Non–Contact Surface Flaw Inspection</u>, M.A.Sc. Thesis, University of Windsor, 1988.

11. Aylesworth, P.A., North, W.P.T., <u>D Sight for Measuring Surface Vibration</u>, Proceedings: D Sight Third Annual Symposium, 1992.

12. Reddy, J. N., <u>An Introduction to the Finite Element Method</u>, McGraw-Hill Book Company, 1984. pp. 405.

13. Mitchell, A. K., Hazell, C. R., <u>Experimental Eigenvalues and Mode Shapes for Flat Clamped Plates</u>, Experimental Mechanics, 26, No. 4, pp. 337–344 (Dec. 1986).

14. Blevins, Robert D., <u>Formulas for Natural Frequency and Mode Shape</u>, Van Nostrand Reinhold Company, 1979. pp. 259.

15. ibid. pp. 264

Appendix I

Exposure Information

The following is exposure information for all D Sight images contained in this thesis.
Thickness of the plate used is indicated by t.

Figure 9: Fuji Neopan 1600 film, 1/2 sec @ f/8. August 16, 1992.
10° angle of incidence, Static with D Sight, t=0.508 mm, Photo 4.10.

Figure 10: Fuji Neopan 1600 film, 1/2 sec @ f/8. August 16, 1992.
10° angle of incidence, 400 Hz, 0° Phase Angle, t=0.508 mm, Photo 4.12.

Figure 11: Fuji Neopan 1600 film, 1/2 sec @ f/8. August 16, 1992.
10° angle of incidence, 400 Hz,180° Phase Angle, t=0.508 mm, Photo 4.13.

Figure 12: Fuji Neopan 1600 film, 1/2 sec @ f/8. August 16, 1992.
10° angle of incidence, 400 Hz, Double Exposure, t=0.508 mm, Photo 4.17.

Figure 13: Fuji Neopan 1600 film, 1/2 sec @ f/8. August 16, 1992.
10° angle of incidence, 400 Hz, 0° Phase Angle, t=0.508 mm, Photo 4.12.
Node Lines superimposed using Adobe Photoshop.

Figure 17: Kodak T-Max 400 film, 2 sec @ f/8. October 30, 1992.
13.5° angle of incidence, 317 Hz, 0° Phase Angle, t=0.508 mm, Photo 5.26.

Figure 18: Kodak T-Max 400 film, 2 sec @ f/8. October 30, 1992.
13.5° angle of incidence, 317 Hz, 180° Phase Angle, t=0.508 mm, Photo 5.27.

Figure 19: Kodak T-Max 400 film, 2 sec @ f/8. October 30, 1992.
13.5° angle of incidence, 317 Hz, Double Exposure, t=0.508 mm, Photo 5.28.

Figure 20: Fuji Neopan 1600 film, 1/2 sec @ f/8. August 16, 1992.
10° angle of incidence, 400 Hz, 0° Phase Angle, t=0.508 mm, Photo 4.16.

Figure 21: Fuji Neopan 1600 film, 1/2 sec @ f/8. August 16, 1992.
30° angle of incidence, 400 Hz, 0° Phase Angle, t=0.508 mm, Photo 4.18.

Figure 22: Fuji Neopan 1600 film, 1/2 sec @ f/8. August 16, 1992.
50° angle of incidence, 400 Hz, 0° Phase Angle, t=0.508 mm, Photo 4.20.

Figure 23: Fuji Neopan 1600 film, 1/2 sec @ f/8. August 16, 1992.
70° angle of incidence, 400 Hz, 0° Phase Angle, t=0.508 mm, Photo 4.22.

Figure 27: Kodak Ektachrome 400 film, 2 sec @ f/8. February 10, 1993.
7° angle of incidence, 140.22 Hz, 0° Phase Angle, t=0.635 mm, Photo 10.07.

Figure 27: Kodak Ektachrome 400 film, 1 sec @ f/8. February 14, 1993.
7° angle of incidence, 223.4 Hz, 180° Phase Angle, t=0.635 mm, Photo 11.36.

Figure 28: Kodak Ektachrome 400 film, 1 sec @ f/8. February 16, 1993.
7° angle of incidence, 306.0 Hz, 180° Phase Angle, t=0.635 mm, Photo 12.04.

Figure 29: Kodak Ektachrome 400 film, 1 sec @ f/8. February 16, 1993.
16.7° angle of incidence, 351.4 Hz, 180° Phase Angle, t=0.635 mm,
Photo 12.28.

Figure 30: Kodak Ektachrome 400 film, 1 sec @ f/8. February 16, 1993.
16.7° angle of incidence, 367.6 Hz, 0° Phase Angle, t=0.635 mm, Photo 12.25.

Figure 31: Kodak Ektachrome 400 film, 1 sec @ f/8. February 16, 1993.
16.7° angle of incidence, 420.2 Hz, 180° Phase Angle, t=0.635 mm,
Photo 12.24.

Figure 32: Kodak Ektachrome 400 film, 1 sec @ f/8. February 16, 1993.
7° angle of incidence, 594.4 Hz, 0° Phase Angle, t=0.635 mm, Photo 12.12.
Node Lines superimposed within FrameMaker 3.0.

Figure 36: Fuji Neopan 1600 film, 1/2 sec @ f/8. August 16, 1992.
10° angle of incidence, Static with D Sight, t=0.508 mm, Photo 4.00.

Figure 37: Fuji Neopan 1600 film, 1/2 sec @ f/8. August 16, 1992.
10° angle of incidence, 320 Hz, 0° Phase Angle, t=0.508 mm, Photo 4.02.

Figure 40: Kodak T-Max 400 film, 2 sec @ f/8. November 10, 1992.
10° angle of incidence, Point contact, Static with D Sight, t=0.508 mm,
Photo 7.21.

Figure 41: Kodak T-Max 400 film, 2 sec @ f/8. November 10, 1992.
10° angle of incidence, Point contact, 301.8 Hz, t=0.508 mm, Photo 7.22.

Figure 42: Kodak T-Max 400 film, 2 sec @ f/8. November 10, 1992.
10° angle of incidence, Point contact, 340.4 Hz, t=0.508 mm, Photo 7.23.

Figure 43: Kodak Ektachrome 400 film, 1 sec @ f/8. February 14, 1993.
7° angle of incidence, 60.82 Hz, 0° Phase Angle, t=0.635 mm, Photo 11.20.

Figure 44: Kodak Ektachrome 400 film, 1 sec @ f/8. February 16, 1993.
7° angle of incidence, 110.43 Hz, 180° Phase Angle, t=0.635 mm, Photo 11.28.

Figure 45: Kodak Ektachrome 400 film, 1 sec @ f/8. February 16, 1993.
7° angle of incidence, 125.16 Hz, 0° Phase Angle, t=0.635 mm, Photo 11.31.

Figure 46: Kodak Ektachrome 400 film, 1 sec @ f/8. February 16, 1993.
16.7° angle of incidence, 301.5 Hz, 0° Phase Angle, t=0.635 mm, Photo 12.29.

Figure 47: Kodak Ektachrome 400 film, 2 sec @ f/8. February 10, 1993.
7° angle of incidence, 312.2 Hz, 180° Phase Angle, t=0.635 mm, Photo 10.23.

Figure 48: Kodak Ektachrome 400 film, 1 sec @ f/8. February 16, 1993.
16.7° angle of incidence, 332.0 Hz, 0° Phase Angle, t=0.635 mm, Photo 12.15.

Figure 49: Kodak Ektachrome 400 film, 1 sec @ f/8. February 16, 1993.
7° angle of incidence, 596.1 Hz, 0° Phase Angle, t=0.635 mm, Photo 11.08.

Figure 50: Kodak Ektachrome 400 film, 1 sec @ f/8. February 16, 1993.
7° angle of incidence, 616.5 Hz, 0° Phase Angle, t=0.635 mm, Photo 11.16.

Appendix II

Raw Data

The following is the raw data for the laser node location experiment described on page 19. Table 12 contains the node and antinode data that is plotted in Figure 15 on page 20. Table 13 contains the interpolated node data which provides smoother node lines as shown in Figure 16 on page 21.

Y	Antinode	Node	Antinode	Node	Antinode	Node	Antinode	Node	Antinode
25.4	38.0	70.0	102.0	133.0	158.0			223.0	258.0
50.8	38.0	65.0	103.0	126.0	160.0	181.0	207.0	240.0	265.0
76.2	34.0	62.0	95.0	130.0	153.0	178.0	207.0	235.0	265.0
101.6	33.0	65.0	89.0	124.0	148.0	176.0	208.0	243.0	266.0
127.0	30.0	61.0	83.0	119.0	144.0	178.0	206.0	234.0	266.0
152.4	31.5	55.5	83.5	115.0	144.5	176.0	205.5	234.5	266.0
177.8	34.5	60.5	91.0	128.0	146.0	175.5	204.0	235.5	265.0
203.2	36.0	65.0	97.0	117.0	152.0	179.0	206.0	234.0	266.0
228.6	37.0	68.0	100.0	126.0	155.0	184.0	214.0	248.0	267.0
254.0	36.0	70.0	99.0	126.0	162.0	192.0	221.0	245.0	275.0
279.4	33.0	65.0	96.0	127.0	161.0	195.0	225.0	251.0	271.0

TABLE 12: Raw Data for Laser Node Location

Y	Antinode	Node	Antinode	Node	Antinode	Node	Antinode	Node	Antinode
25.4	38.0	70.0	102.0	130.0	158.0		208.0		258.0
50.8	38.0	70.5	103.0	131.5	160.0	183.5	207.0	236.0	265.0
76.2	34.0	64.5	95.0	124.0	153.0	180.0	207.0	236.0	265.0
101.6	33.0	61.0	89.0	118.5	148.0	178.0	208.0	237.0	266.0
127.0	30.0	56.5	83.0	113.5	144.0	175.0	206.0	236.0	266.0
152.4	31.5	57.5	83.5	114.0	144.5	175.0	205.5	235.8	266.0
177.8	34.5	62.8	91.0	118.5	146.0	175.0	204.9	234.5	265.0
203.2	36.0	66.5	97.0	124.5	152.0	179.0	206.0	236.0	266.0
228.6	37.0	68.5	100.0	127.5	155.0	184.5	214.0	240.5	267.0
254.0	36.0	67.5	99.0	130.5	162.0	191.5	221.0	248.0	275.0
279.4	33.0	64.5	96.0	128.5	161.0	193.0	225.0	248.0	271.0

TABLE 13: Interpolated Node Data for Laser Node Location

Table 14 contains frequencies found using FEA with various plate thickness values used in the graph in Figure 26 on page 34.

Thickness	Frequency (Hz)			
(mm)	Mode 1	Mode 5	Mode 8	Mode 12
0.1	17.195	44.759	58.491	61.190
0.2	34.372	89.473	116.920	122.320
0.4	68.569	178.490	233.250	244.010
0.6	103.070	268.310	350.620	366.800
0.8	137.570	358.120	467.990	489.580
1.0	171.950	447.590	584.910	611.900

TABLE 14: Raw Data for Thickness Graph

Appendix III

C Code for Data Manipulation

```
#include <Files.h>
#include <StandardFile.h>
#include <Dialogs.h>
#include <stdio.h>
#include <stdlib.h>
#include <string.h>
#include <math.h>


#define ErrorAlert          256
#define EOL                  13
#define MAXLINE             200
#define NIL_POINTER          0L
#define REMOVE_ALL_EVENTS     0


int OldFile (Str255 fn );
int pStrCopy(StringPtr a, StringPtr b);
int FileError(Str255 s, Str255 f);
void ToolBoxInit( void );
int ReadData( int refNum );
int SaveData( int modeNum );
short ReadLine( int refNum, char *lineBuf );
int WriteData( short rNum, Str255 fileName );


TEHandle TEH;
static Point SFGwhere = { 90, 82 };
static SFReply reply;
/* make this array bigger for more elements */
float dataArray[31][31];

short vRef ;
int   numElements, numModes;
int   modeNum;


main()
    {
        short  rc, refNum;
        Str255 fn;

        ToolBoxInit();

        /* Open the ALGOR file to parse */
        if( OldFile(fn) )
            if( FSOpen( fn, vRef, &refNum )!=noErr){
                FileError( "\pl14 Error opening ", fn );
            exit(1);
            }

        /* find number of elements and modes */
        ReadNodes( refNum );

        /* Read the data for one mode */
        ReadData( refNum );

        /* save the data file */
```

```
        SaveData( modeNum );

        /* All done! Close it up! */
        FSClose( refNum );
    }


short ReadLine( int refNum, char *lineBuf )
    {
        IOParam pb;
        short   len, rc;   /*line length, return code */

        pb.ioRefNum = refNum;
        pb.ioVRefNum = vRef;
        pb.ioPosMode = fsAtMark | 0x80 | (256*EOL);
        pb.ioReqCount = MAXLINE;   /* max line size */
        pb.ioBuffer = lineBuf;       /* transfer to this address */
        rc = PBRead( &pb, FALSE );   /* read one line */
        if(rc==eofErr && pb.ioActCount==0)
            return( eofErr );                /* end of file reaced */
        if( (rc==noErr) || (rc==eofErr) ){
            len = pb.ioActCount;
            if( len==MAXLINE ) return( -1 );   /* not a delimited file */
            if( lineBuf[len-1] != EOL ) len++;   /* last line has no EOL */
            lineBuf[len-1] = 0;              /* convert to ASCIIZ */
        }
        return(rc);
    }

int OldFile( Str255 fn )

{
    SFTypeList myTypes;

    myTypes[0]='TEXT';

    SFGetFile(SFGwhere, "\p", 0L, 1, myTypes, 0L, &reply );

    if (!reply.good)
        exit(0);
    else {
        pStrCopy(reply.fName, fn);
        vRef = reply.vRefNum;
        return(1);
    }
}

int pStrCopy (StringPtr p1, StringPtr p2)

/* copies a pascal string from p1 to p2 */
{
    register int len;

    len = *p2++ = *p1++;
    while (--len>=0) *p2++=*p1++;
}
```

```
int FileError(Str255 s, Str255 f)

{
    ParamText(s, f,"\p", "\p");
    Alert(ErrorAlert, 0L);
}

void ToolBoxInit( void )
{
    InitGraf( &thePort );
    InitFonts();
    FlushEvents( everyEvent, REMOVE_ALL_EVENTS );
    InitWindows();
    InitMenus();
    TEInit();
    InitDialogs( NIL_POINTER );
    InitCursor();
}

int ReadData( int refNum )
{
    char   lineBuffer[255], sFirst[255], sSecond[255];
    int    irow, icol, elNum, aEls;
    double disp;
    char*  position;
    int    iErr, jErr;

    aEls = numElements*2+1;
    do{
        ReadLine( refNum, lineBuffer );
        position = strstr(lineBuffer, "mode number =");
    }while(position == 0);
    sscanf( position+16, "%d", &modeNum );

    /* read 8 useless lines */
    ReadLine( refNum, lineBuffer );
    ReadLine( refNum, lineBuffer );
    ReadLine( refNum, lineBuffer );
    ReadLine( refNum, lineBuffer );
    ReadLine( refNum, lineBuffer );
    ReadLine( refNum, lineBuffer );
    ReadLine( refNum, lineBuffer );
    ReadLine( refNum, lineBuffer );
    if( numElements <= 0 ){
        FileError("\pnumElements is in error", "\p" );
        exit(1);
    }

    /* read element data */
    do{
        ReadLine( refNum, lineBuffer );
        strncpy( sFirst, lineBuffer, 6 );
        sFirst[6] = 0;
        elNum = atoi( sFirst );

        strncpy( sSecond, lineBuffer+31, 12 );
        sSecond[12] = 0;
        disp = atof( sSecond );
```

```
        irow = (elNum-1) / (numElements+1);
        icol = numElements + (elNum-1) % (numElements+1);

        dataArray[irow][icol] = disp;
        dataArray[irow][aEls-icol] = disp;
        dataArray[aEls-irow][icol] = disp;
        dataArray[aEls-irow][aEls-icol] = disp;
    }while(elNum);
    return(0);
}

int ReadNodes( int refNum )
{
    char    lineBuf[100];
    char*   position;
    int     tempValue;

    do{
        ReadLine( refNum, lineBuf );
        position = strstr(lineBuf, "(NUMNP) =");
    }while(position == 0);
    sscanf( position+12, "%d", &tempValue );
    numElements = (int)sqrt( (double)tempValue ) - 1;

    do{
        ReadLine( refNum, lineBuf );
        position = strstr(lineBuf, "(NF) =");
    }while(position == 0);
    sscanf( position+12, "%d", &numModes );

    return(0);
}

int SaveData( int modeNum )
{
    short       refNum;
    Str255      fileName = "\pMode ";
    int         iErr;
    static char modeCount = 'A';

    /* create name of data file */
    fileName[6] = modeCount++;
    Create( fileName, vRef, 'MSWD', 'TEXT' );

    if (FSOpen(fileName, vRef, &refNum) != noErr) {
        FileError("\p115 Error opening file ", fileName);
        exit(1);
    } else {
        WriteData( refNum, fileName );
        FSClose(refNum);
        return(1);
    }
}

int WriteData( short rNum, Str255 fileName )
{
    int     iErr;
```

```
long    inOutCount;
int     row, column;
char    tempString[80], statusString[100];

for( row=0; row <= (numElements*2); row++ ){
    for( column=0; column <= (numElements*2-1); column++ ){
        sprintf( tempString, "%e\t", dataArray[row][column] );
        inOutCount = strlen(tempString);
        if( FSWrite( rNum, &inOutCount, tempString )!=0 ){
            FileError("\p117 Error writing to file ", fileName);
            exit(1);
        }
    }
    sprintf( tempString, "%e\r", dataArray[row][column] );
    inOutCount = strlen(tempString);
    if( FSWrite( rNum, &inOutCount, tempString ) != 0){
        FileError("\p118 Error writing to file ", fileName);
        exit(1);
    }
}
return(0);
}

int WriteStatus( char* string )
{
    long    iErr;
    long    inOutCount;
    int     row, column;
    char    tempString[80];
    short   SFRefNum;
    Str255 statusFileName, errorString;

    pStrCopy( "\pStatus File", statusFileName );
    iErr = Create( statusFileName, vRef, 'MSWD', 'TEXT' );

    if (iErr=FSOpen(statusFileName, vRef, &SFRefNum) != noErr) {
        sprintf((char*)errorString,
            "Error opening file "%#s". Error number %d",
            statusFileName, iErr );
        CtoPstr(errorString);
        FileError("\p111.\r", errorString);
        exit(1);
    }
    if( SetFPos( SFRefNum, 2, 0L ) != 0 ){
        FileError("\p112 Error setting position in file ",
            statusFileName);
        exit(1);
    }
    strcat( string, "\r" );
    inOutCount = strlen( string );
    if( FSWrite( SFRefNum, &inOutCount, string ) != 0){
        FileError("\p113 Error writing to file ", statusFileName);
        exit(1);
    }
    FSClose(SFRefNum);
    return(0);
```

Appendix IV
Dynamic D Sight Photographs

The following are the Dynamic D Sight photographs that did not have a counterpart in the FEA solutions.
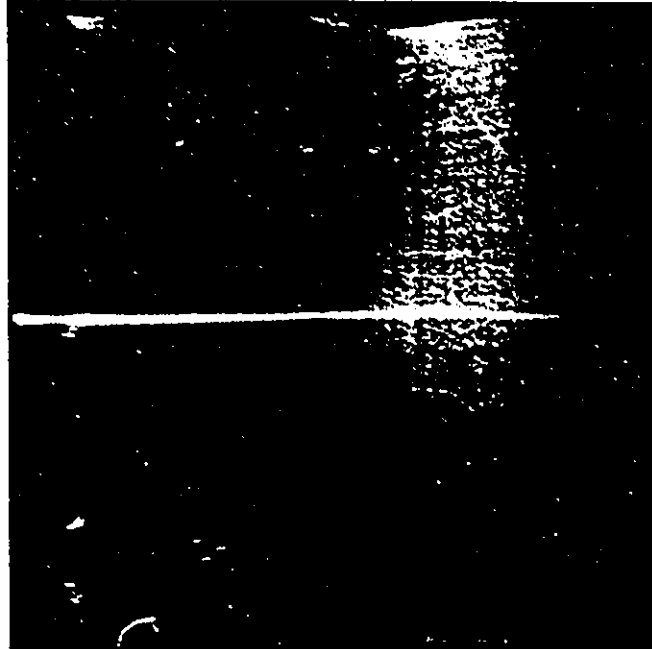
FIGURE 43: 61 Hz Mode Shape (2,1)
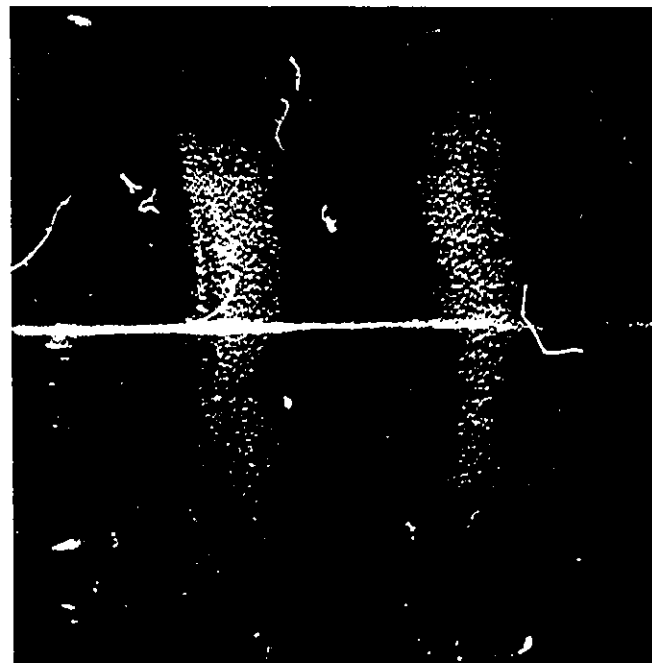
FIGURE 44: 110 Hz Mode Shape (5,1)
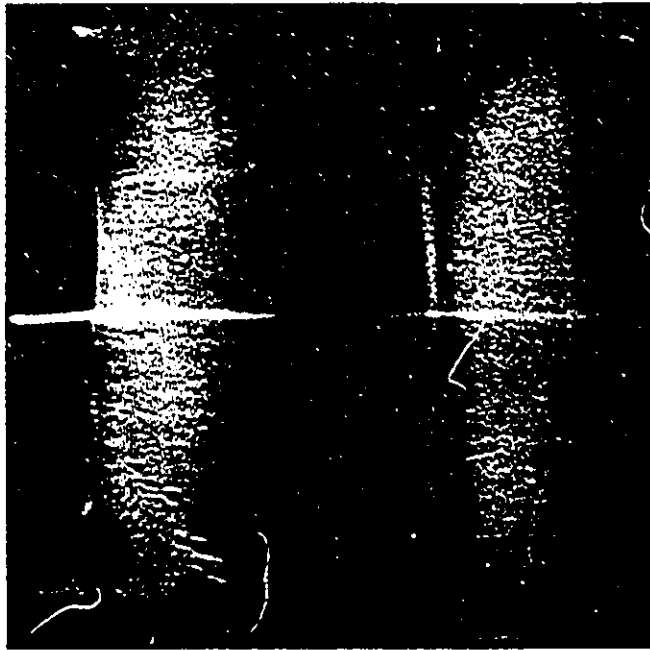
FIGURE 45: 125 Hz Mode Shape (3,1)
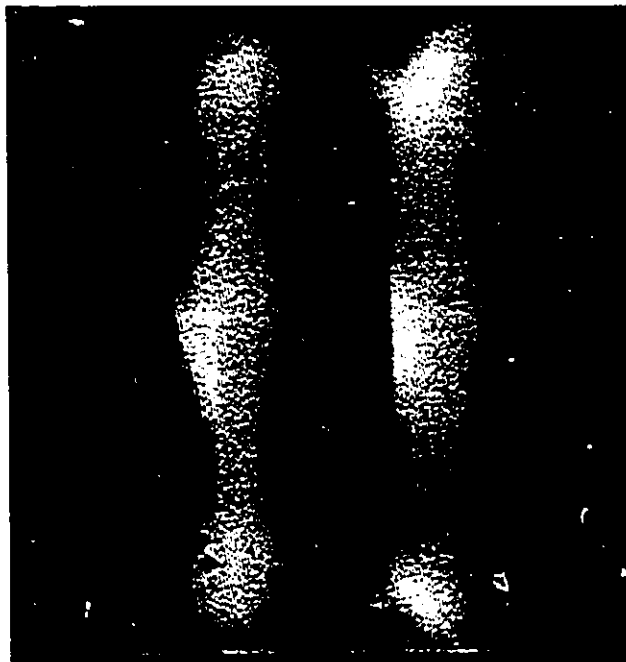
FIGURE 46: 302 Hz Mode Shape (5,1)
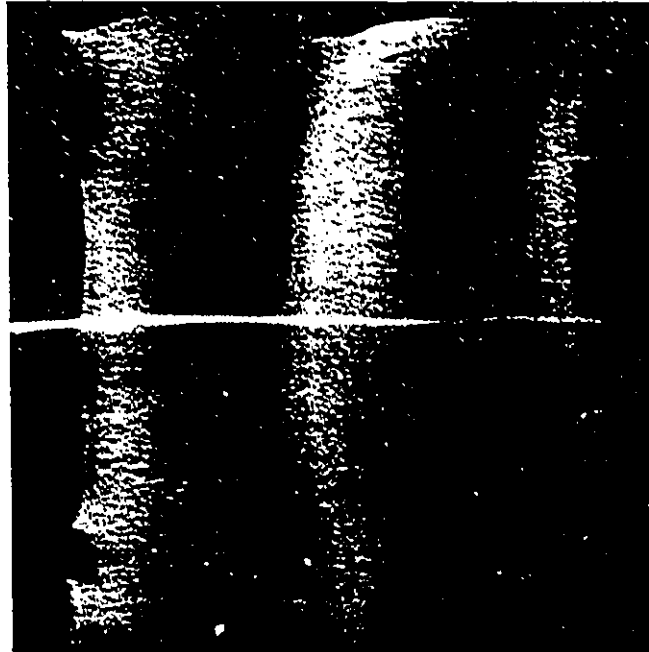
FIGURE 47: 312 Hz Mode Shape (5,1)
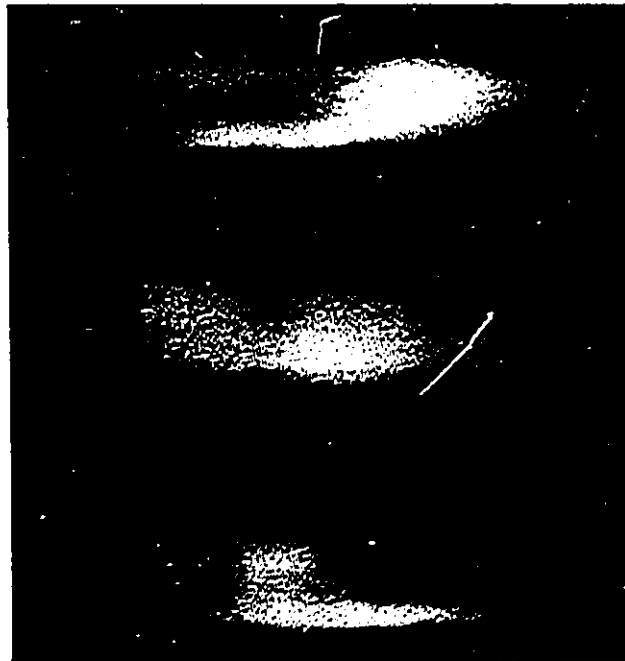
FIGURE 48: 332 Hz Mode Shape (1,5)
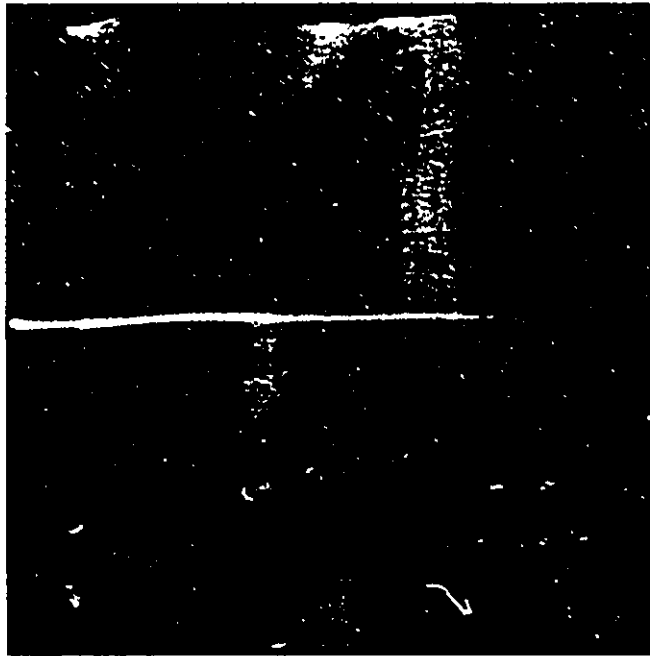
FIGURE 49: 596 Hz Mode Shape (5,5)
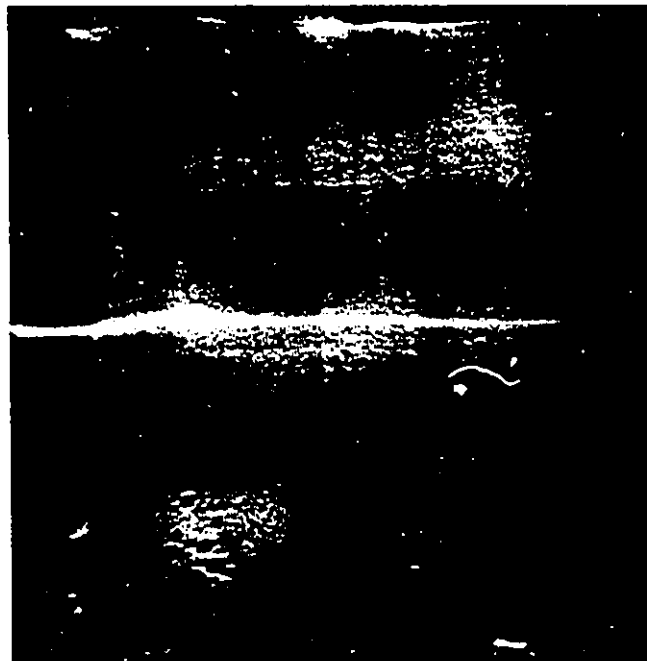
FIGURE 50: 617 Hz Mode Shape (6,7)

Appendix V
FEA Mode Shapes

The mode shapes were on the following pages were calculated using ALGOR FEA software. The plate thickness is 0.625 mm to correspond to the plate used in the set of Dynamic D Sight images used to corollate to the FEA values. Frequency values for FEA and the approximate theoretical method are given in Table 15. The mode numbers in brackets are for modes that could not be readily interpreted as a mode index (i, j).

FEA Mode Number	i	j	Theoretical Frequency	FEA Frequency
1	1	1	40.03	39.96
2	1	2	81.69	81.51
2	2	1	81.69	
3	2	2	120.52	120.32
(4)	1	3	146.77	146.15
(5)	3	1	146.77	146.83
6	2	3	183.76	183.52
6	3	2	183.76	
7	1	4	234.13	233.80
7	4	1	234.13	
8	3	3	244.71	245.09
(9)	2	4	270.27	269.44
(10)	4	2	270.27	270.50
11	3	4	329.55	330.29
11	4	3	329.55	
(12)	1	5	343.47	343.04
(13)	5	1	343.47	343.32
14	2	5	379.25	378.90
14	5	2	379.25	
15	4	4	412.65	414.62
(16)	3	5	437.49	438.08
(17)	5	3	437.49	439.27
18	1	6	474.71	474.52
18	6	1	474.71	
(19)	2	6	510.37	509.82
(20)	6	2	510.37	510.43
21	4	5	519.19	522.16
21	5	4	519.19	
22	3	6	567.99	569.52

TABLE 15: FEA and Theory Frequency Values

FEA Mode Shapes

FEA Mode Number	I	j	Theoretical Frequency	FEA Frequency
22	6	3	567.99	
(23)	5	5	624.34	627.69
(24)	1	7	627.83	627.79
(25)	7	1	627.83	629.58
(26)	4	6	648.67	652.34
(27)	6	4	648.67	653.55
28	2	7	663.47	663.32
28	7	2	663.47	
(29)	3	7	720.74	722.45
(30)	7	3	720.74	723.26
31	5	6	752.63	759.77
31	6	5	752.63	
33	4	7	800.72	806.03
33	7	4	800.72	
32	1	8	802.81	802.80
32	8	1	802.81	
(34)	2	8	838.48	838.38
(35)	8	2	838.48	838.74
36	6	6	879.76	890.55
37	3	8	895.55	898.11
37	8	3	895.55	
(38)	5	7	903.73	912.83
(39)	7	5	903.73	914.01
(40)	4	8	975.06	981.42
(41)	8	4	975.06	982.32
(42)	1	9	999.65	999.54
(43)	9	1	999.65	999.62
45	6	7	1029.83	1043.80
45	7	6	1029.83	
(44)	2	9	1035.38	1035.40
(44)	9	2	1035.38	
46	5	8	1077.37	1089.20
46	8	5	1077.37	
(47)	3	9	1092.36	1095.30
(48)	9	3	1092.36	1095.80
49	9	4	1171.55	1179.30
49	4	9	1171.55	
50	7	7	1178.91	1198.40

TABLE 15: FEA and Theory Frequency Values

15 X 15 Elements
Mode 1 (1SS)
39.96 Hz
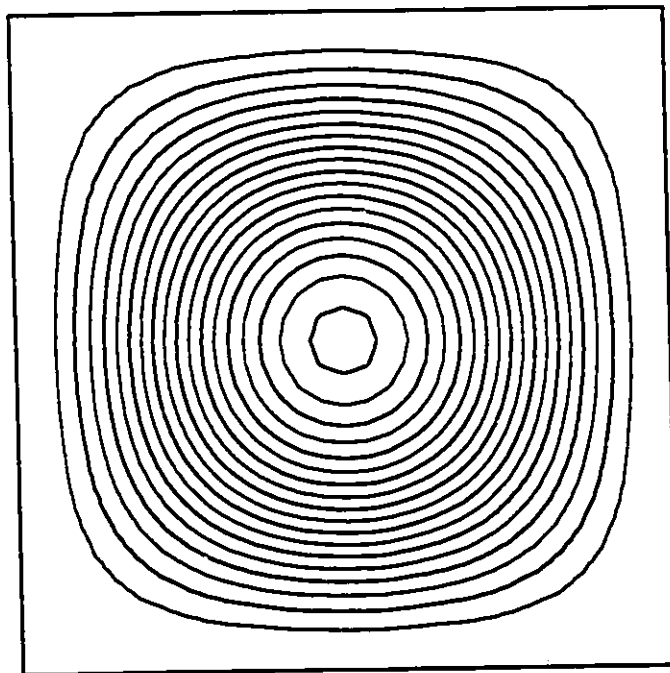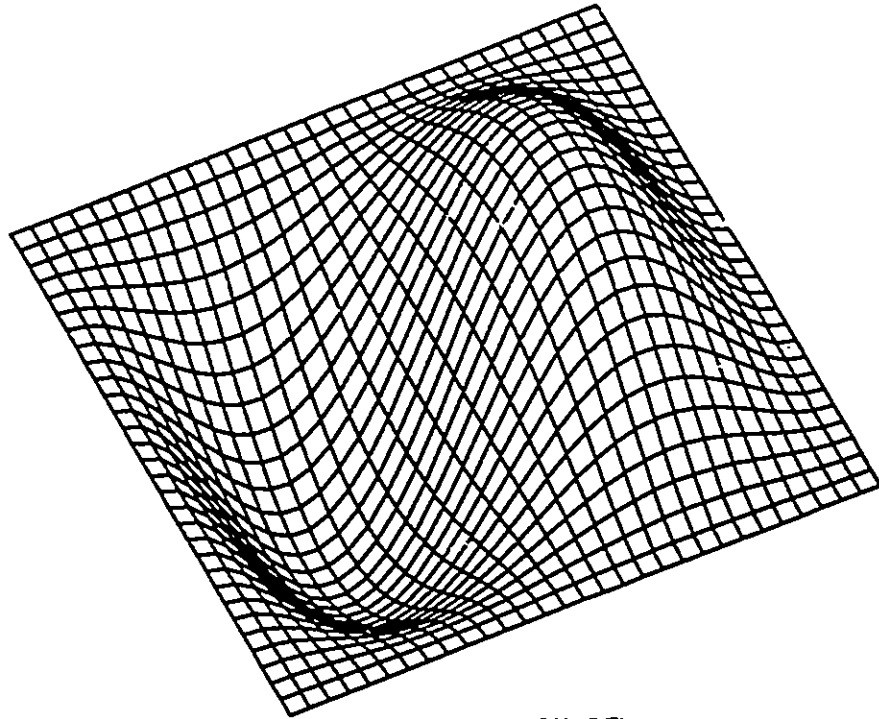
15 X 15 Elements
Mode 2 (1SA)
81.51 Hz
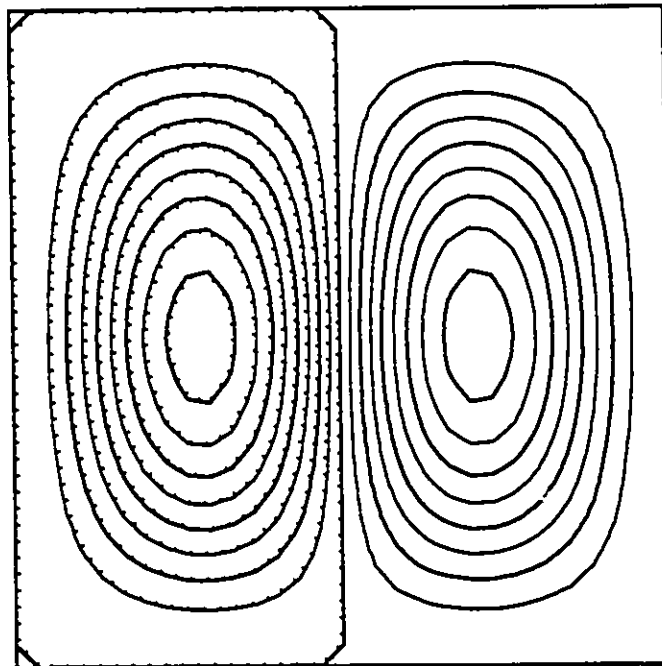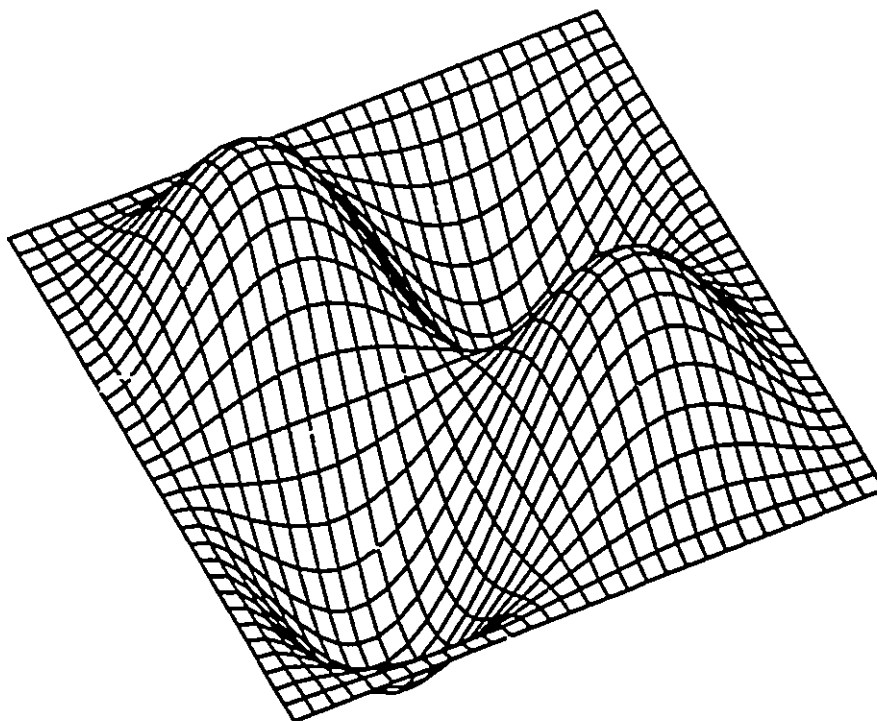
15 X 15 Elements
Mode 3 (1AA)
120.32 Hz
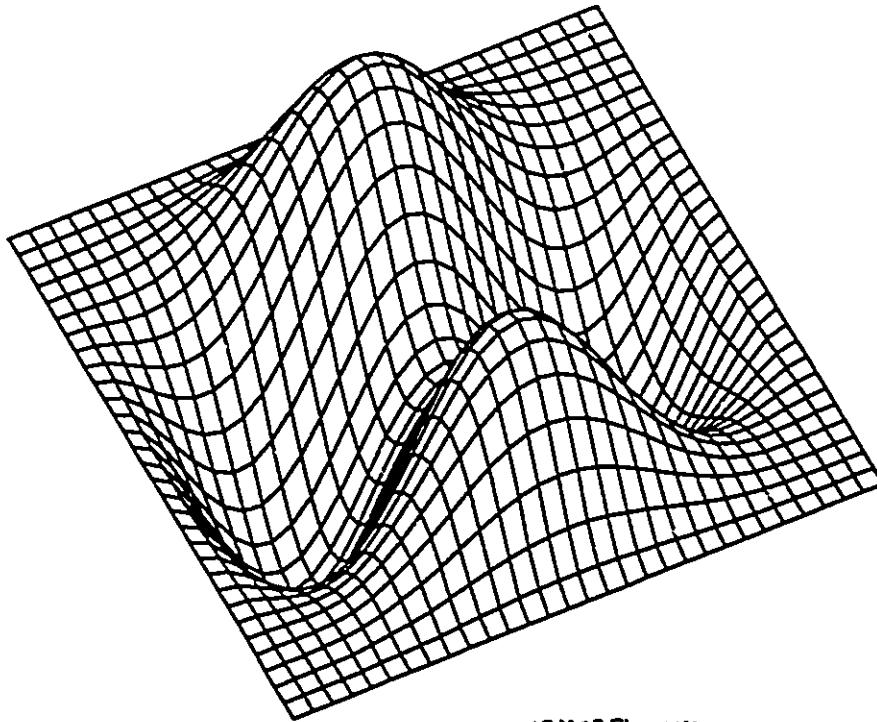
15 X 15 Elements
Mode 4 (2SS)
146.15 Hz
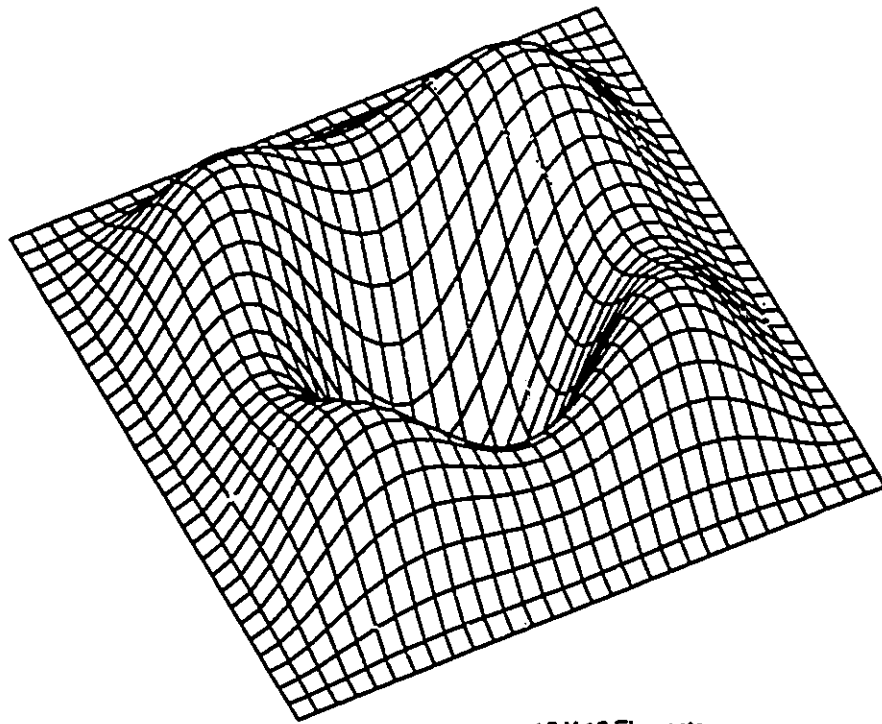
15 X 15 Elements
Mode 5 (3SS)
146.83 Hz
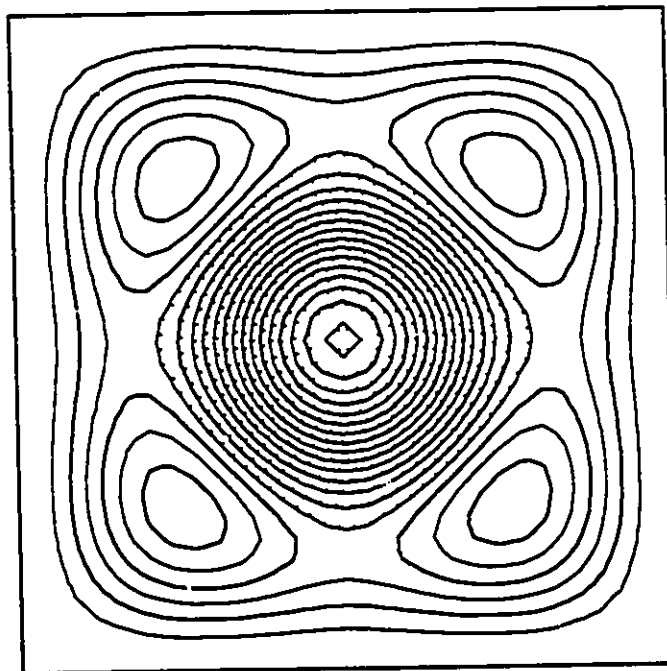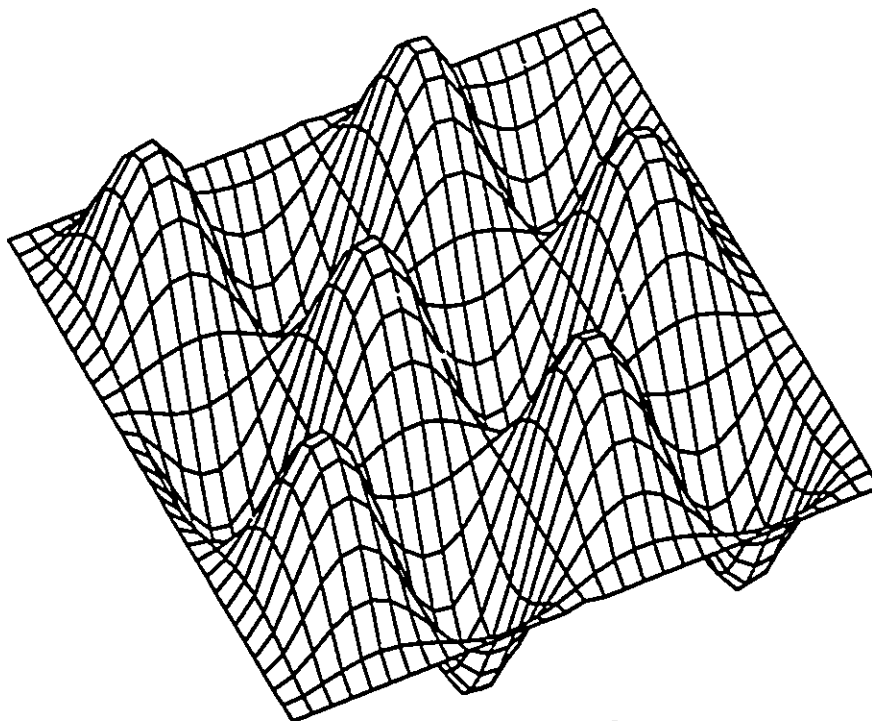
15 X 15 Elements
Mode 6 (2SA)
183.52 Hz
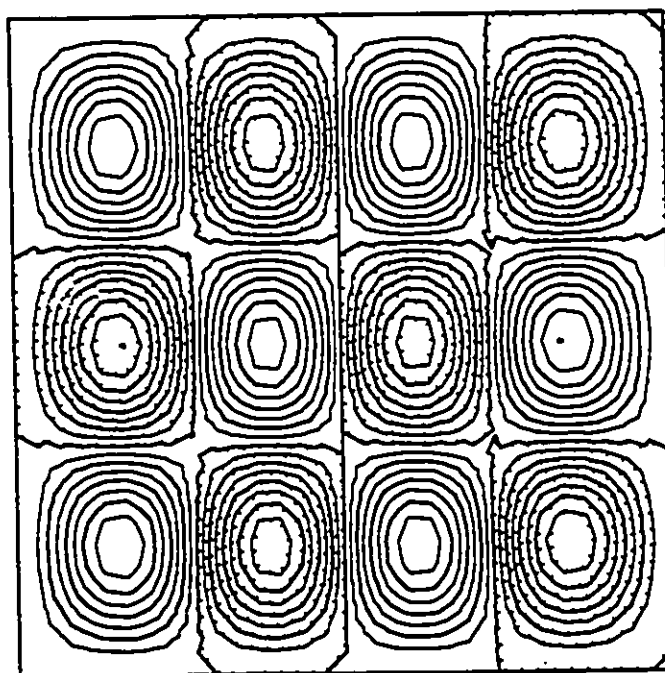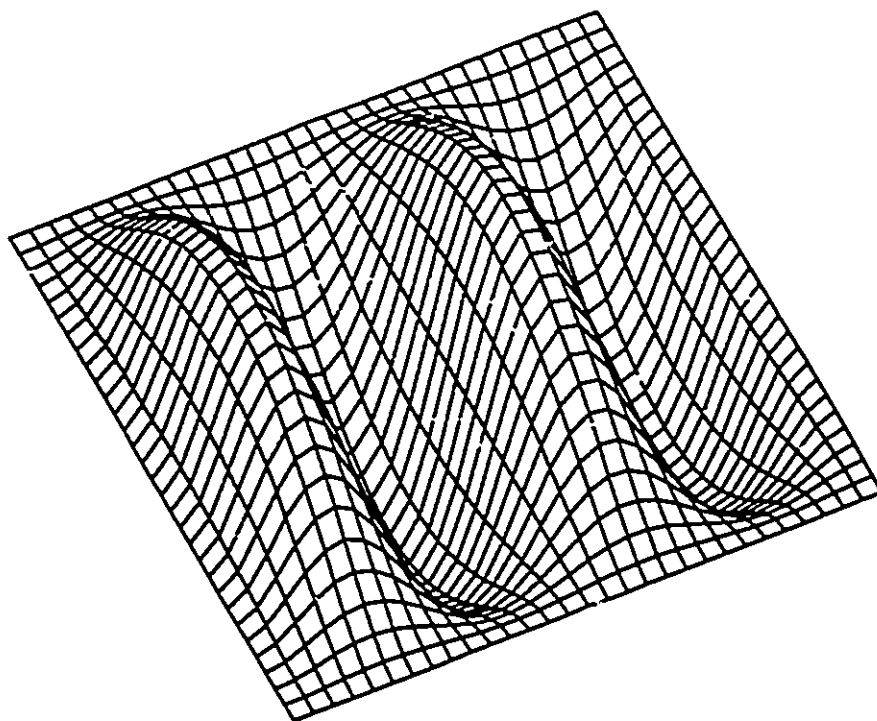
15 X 15 Elements
Mode 7 (3SA)
233.80 Hz
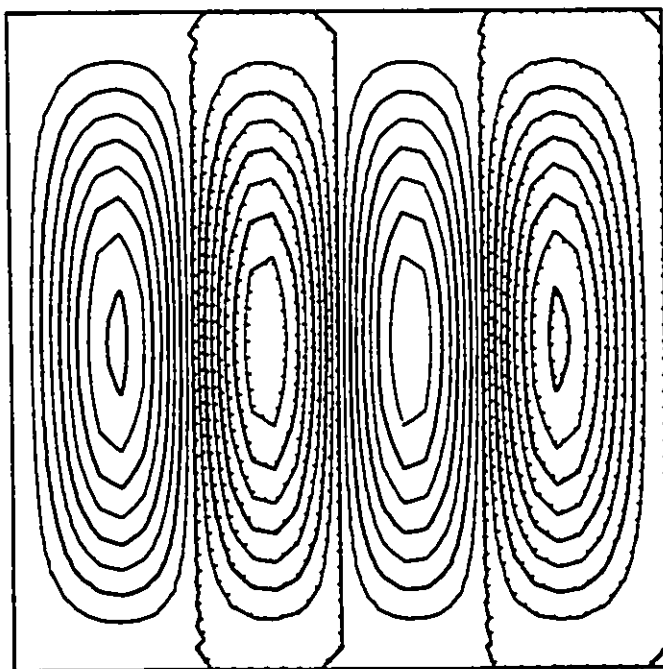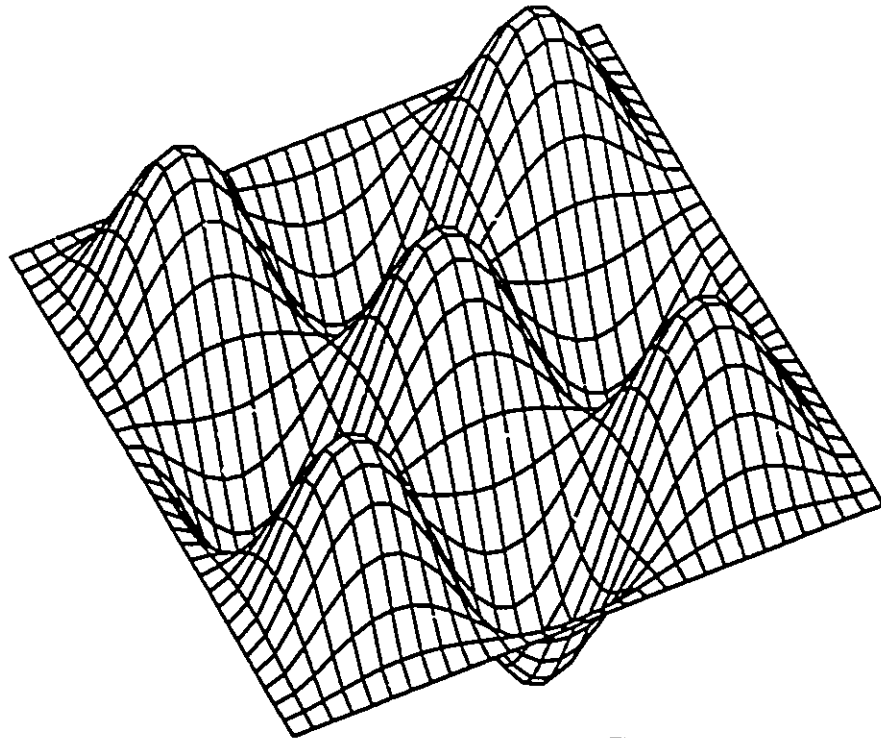
15 X 15 Elements
Mode 8 (4SS)
245.09 Hz
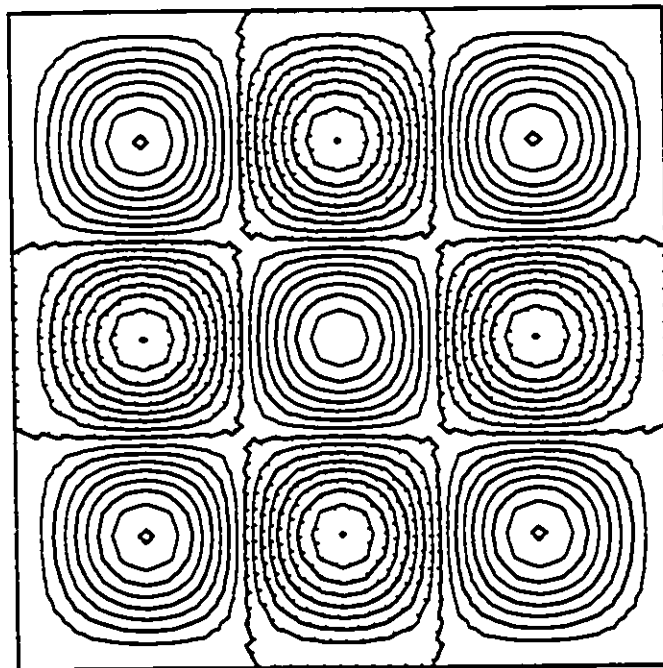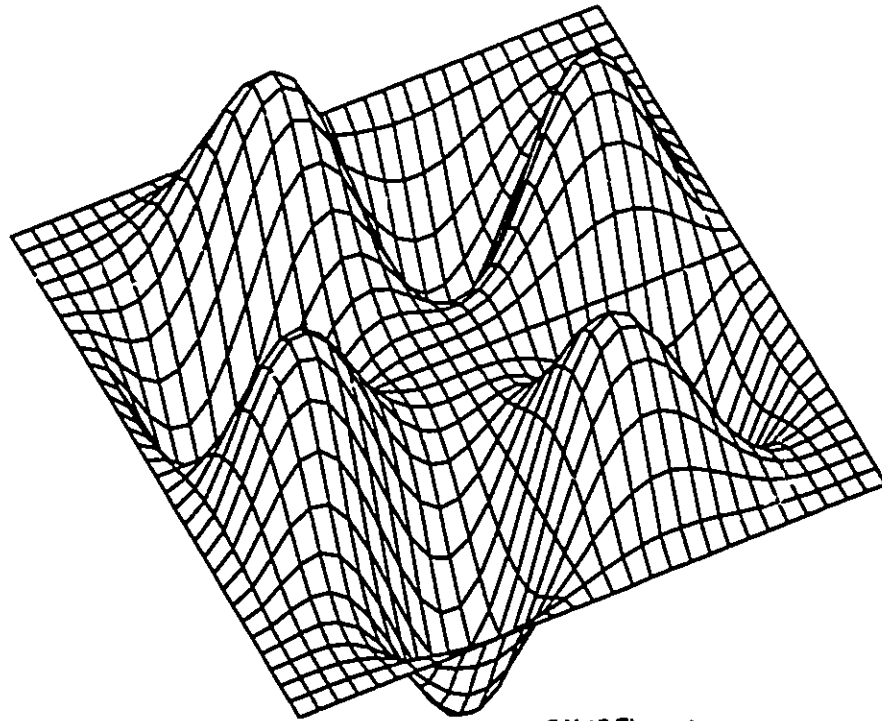
15 X 15 Elements
Mode 9 (2AA)
269.44 Hz
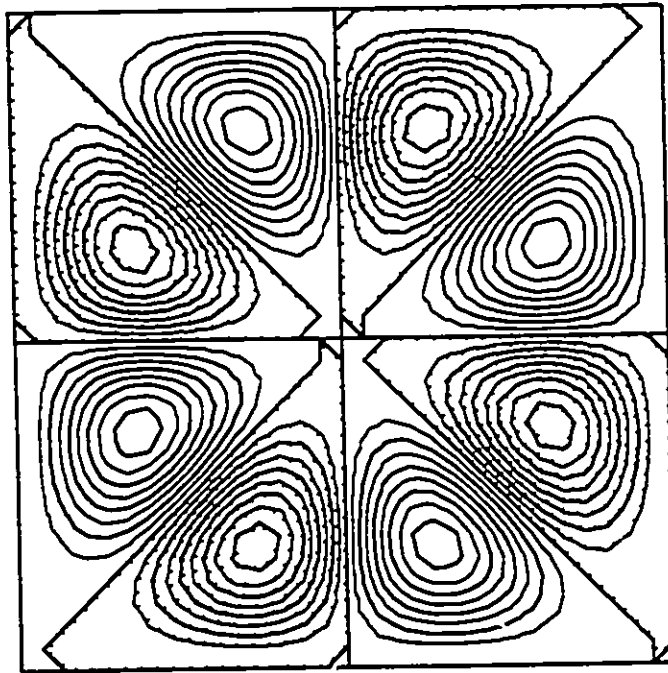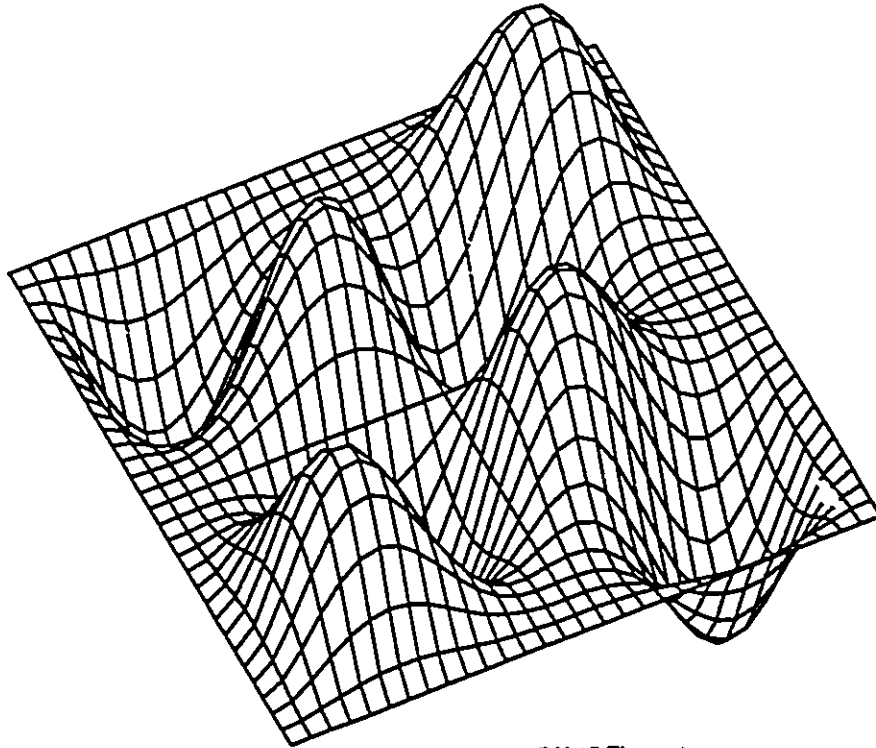
15 X 15 Elements
Mode 10 (3AA)
270.50 Hz
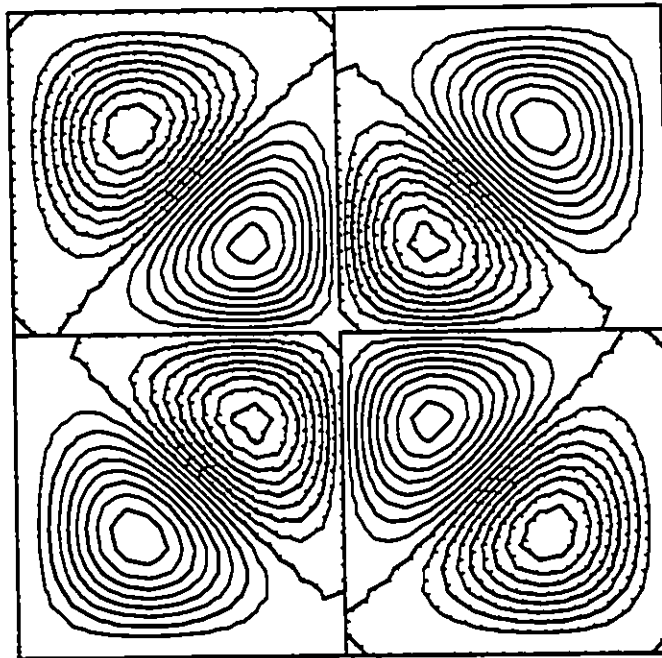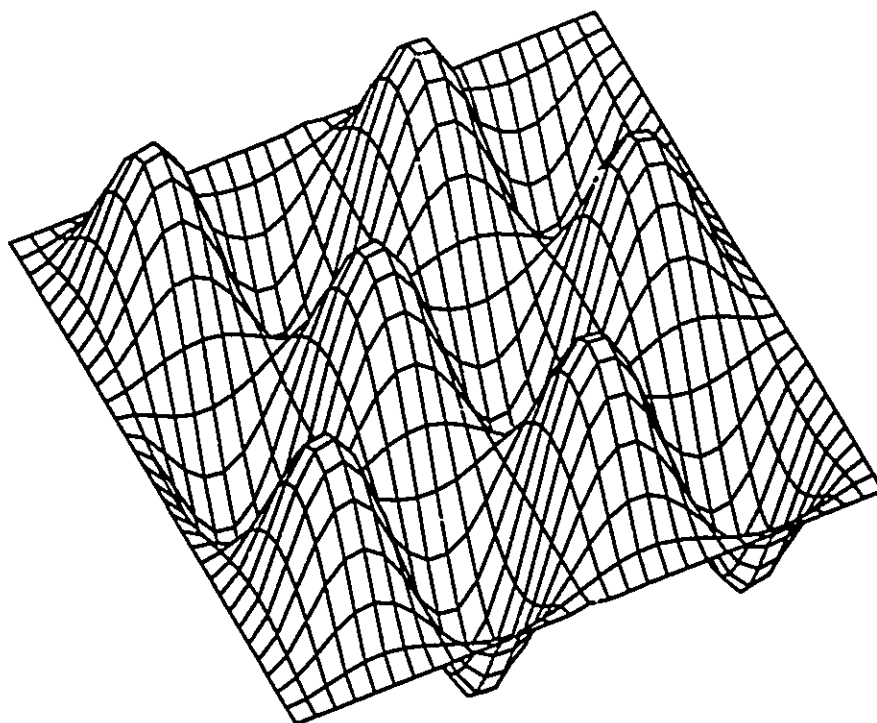
15 X 15 Elements
Mode 11 (4SA)
330.29 Hz
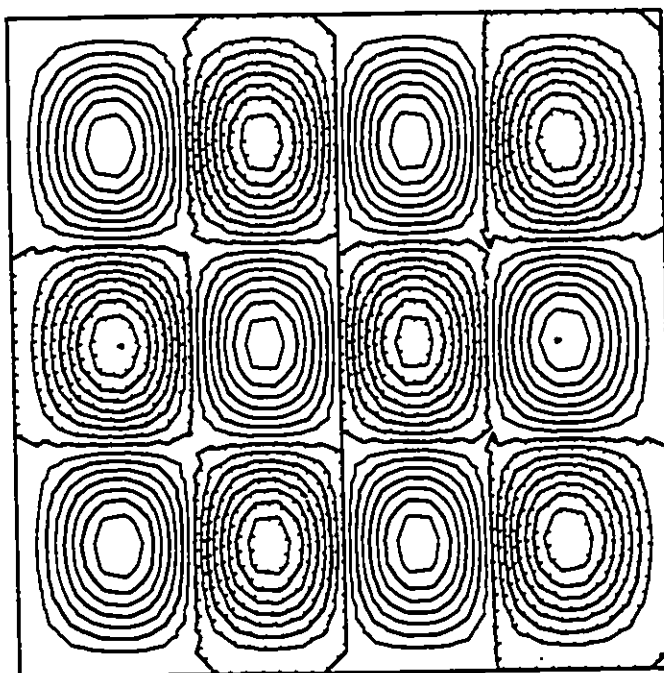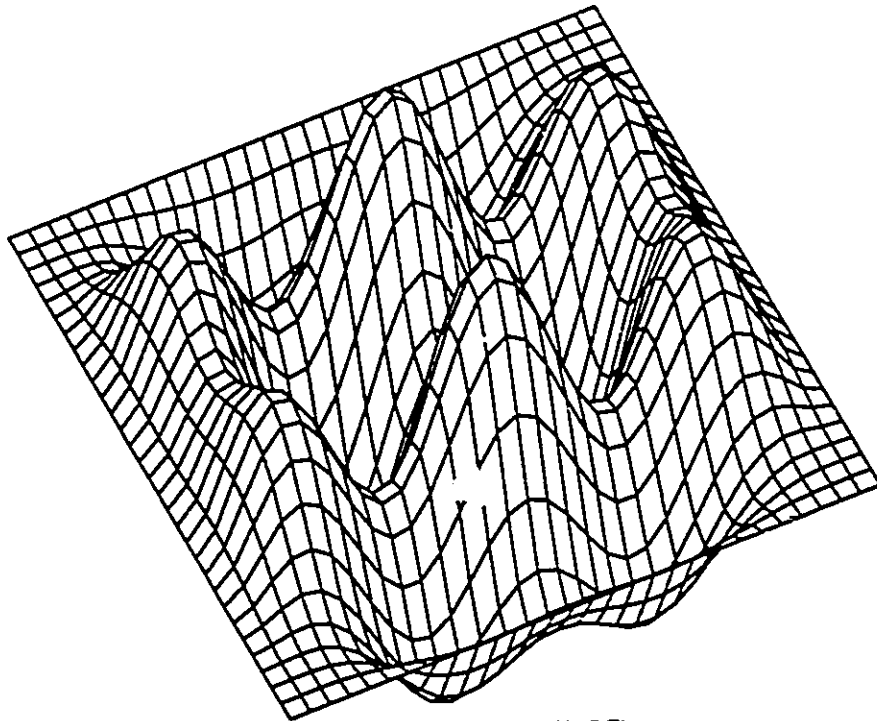
15 X 15 Elements
Mode 12 (5SS)
343.04 Hz
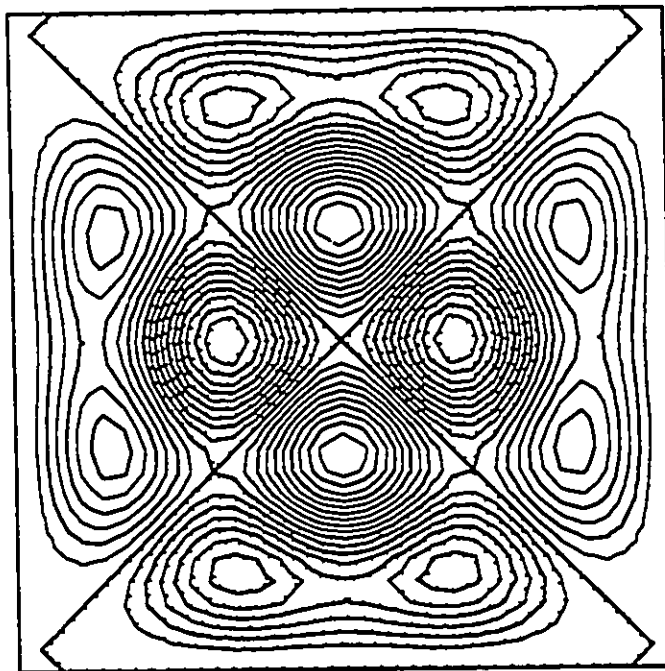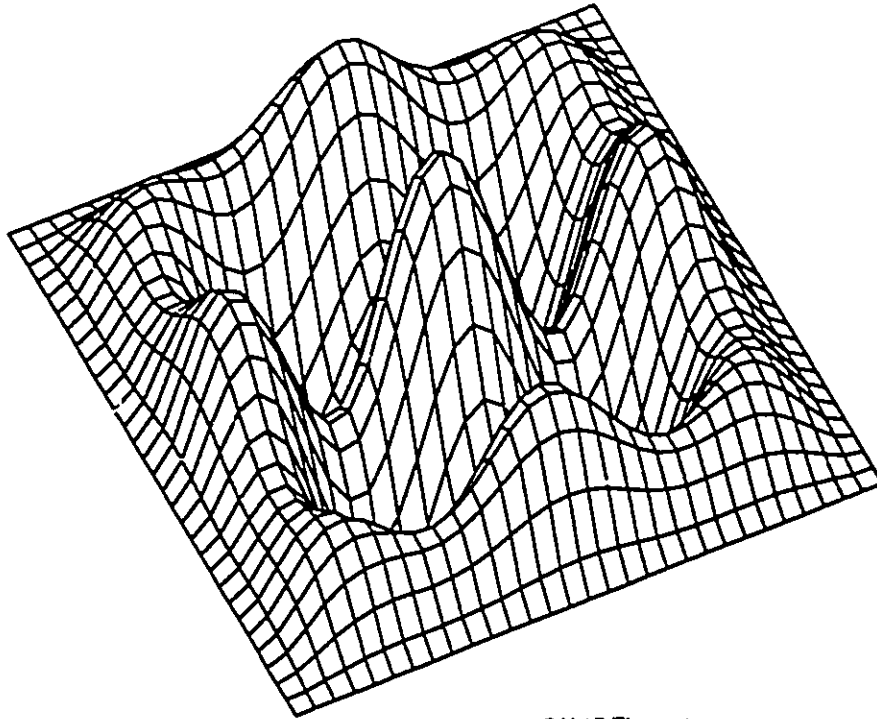
15 X 15 Elements
Mode 13 (6SS)
343.32 Hz
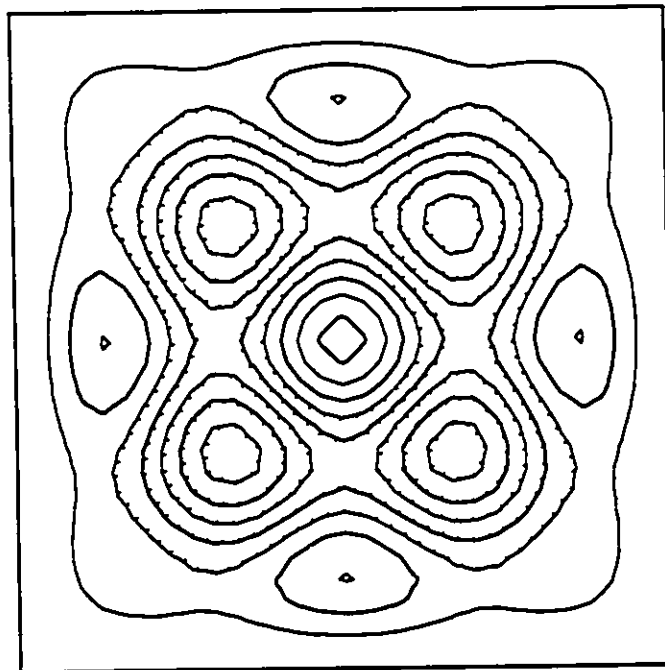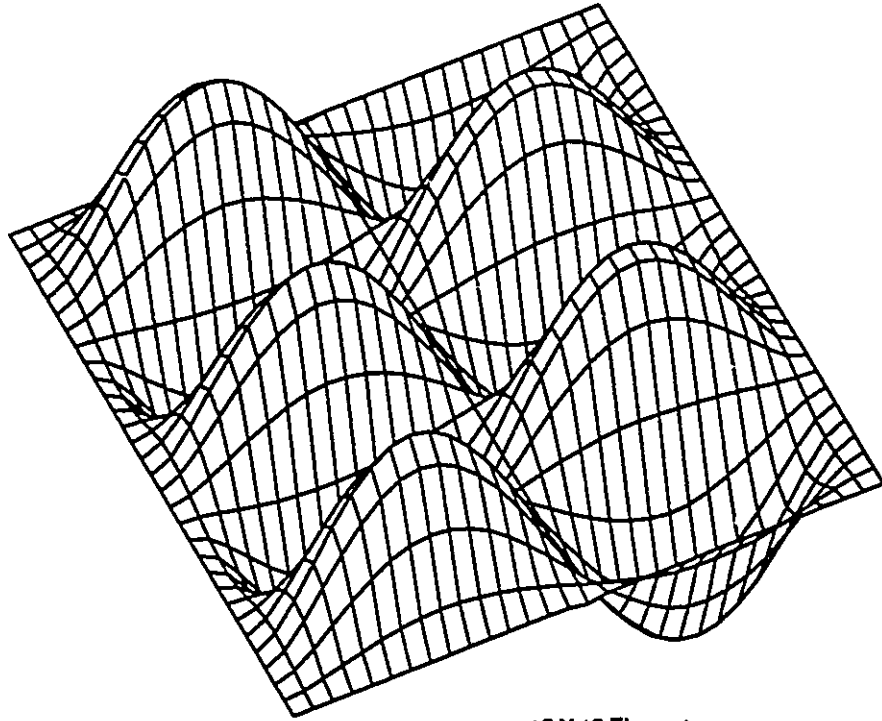
15 X 15 Elements
Mode 14 (5SA)
378.90 Hz
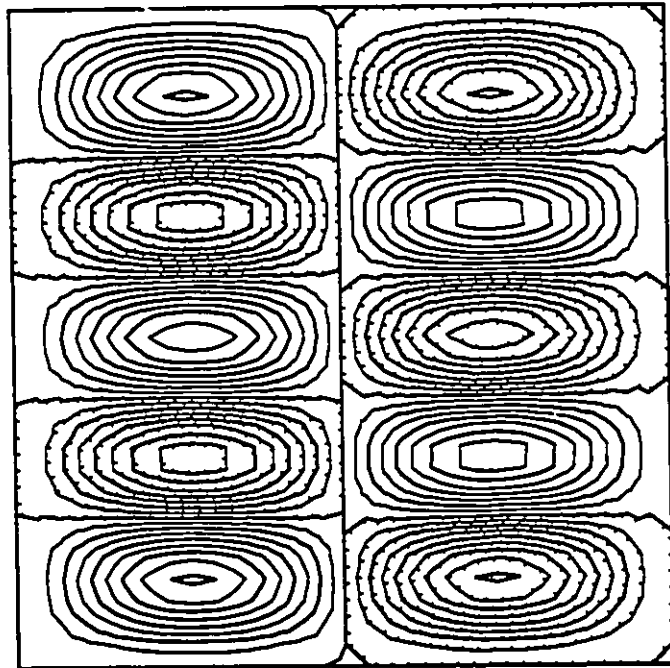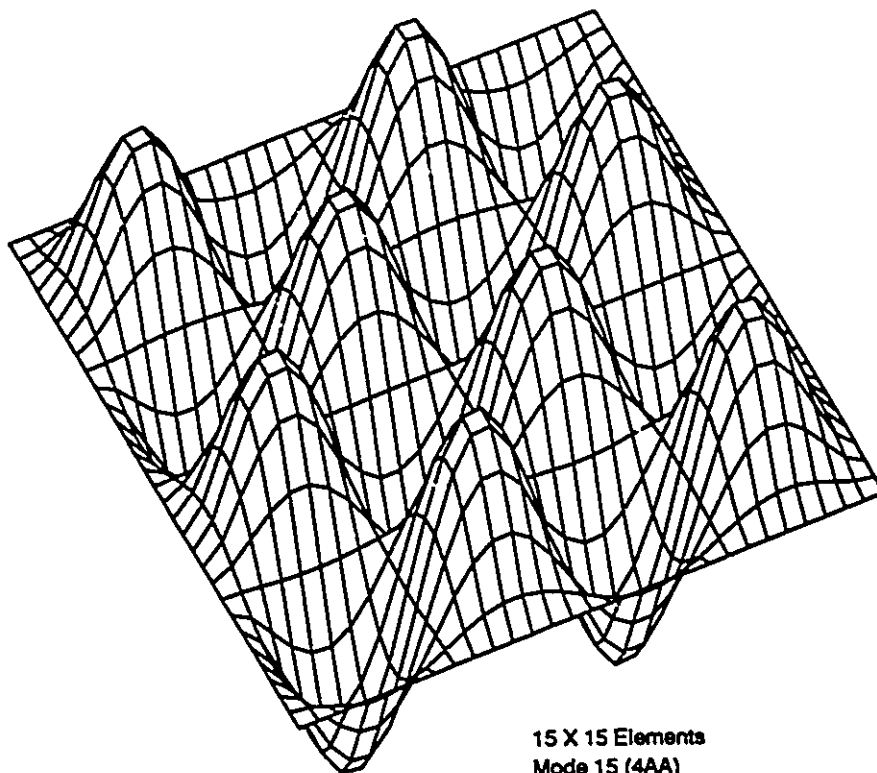
15 X 15 Elements
Mode 15 (4AA)
414.62 Hz
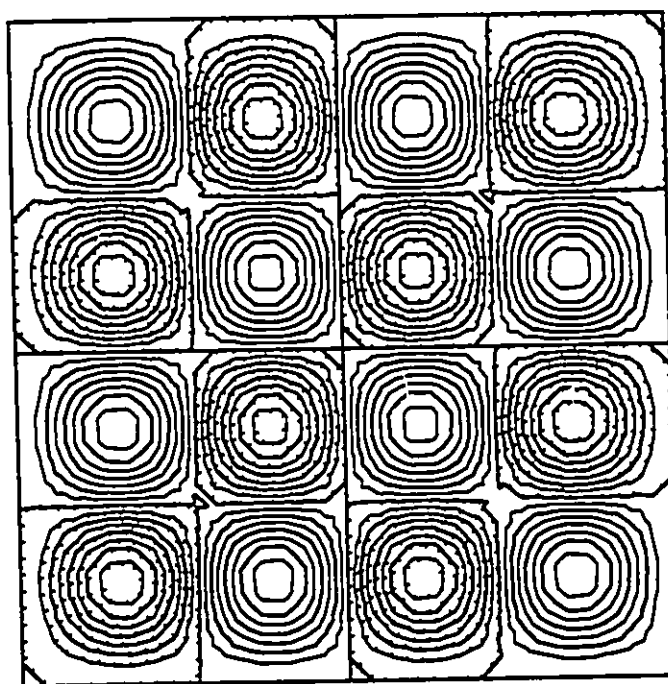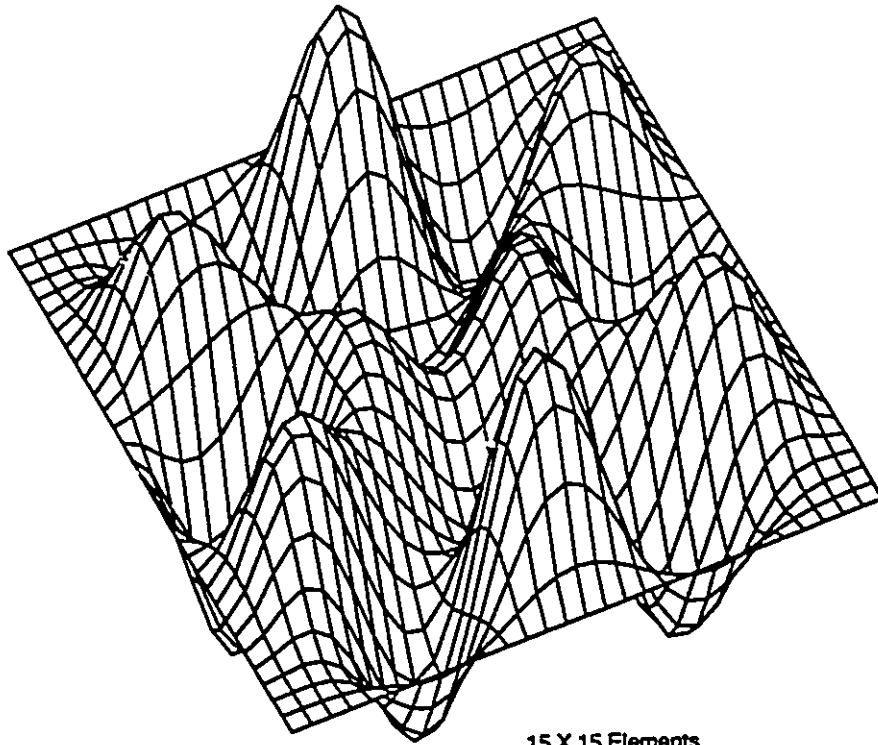
15 X 15 Elements
Mode 16 (7SS)
438.08 Hz
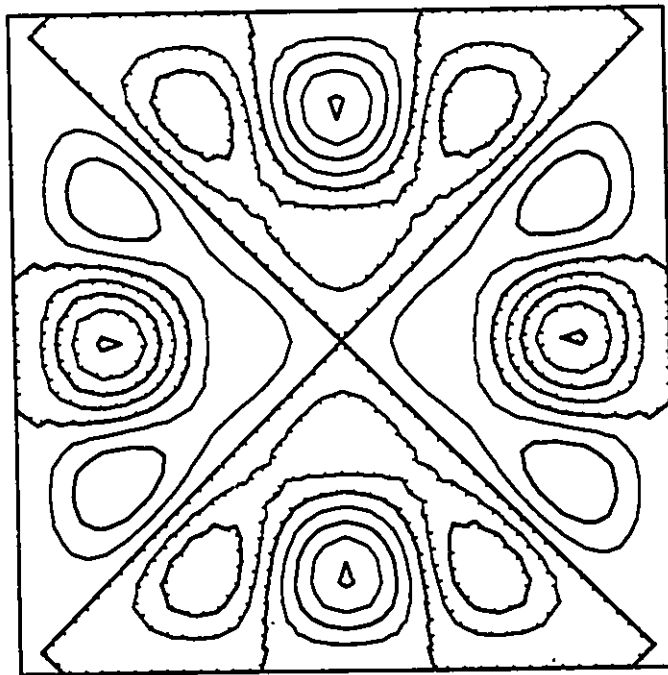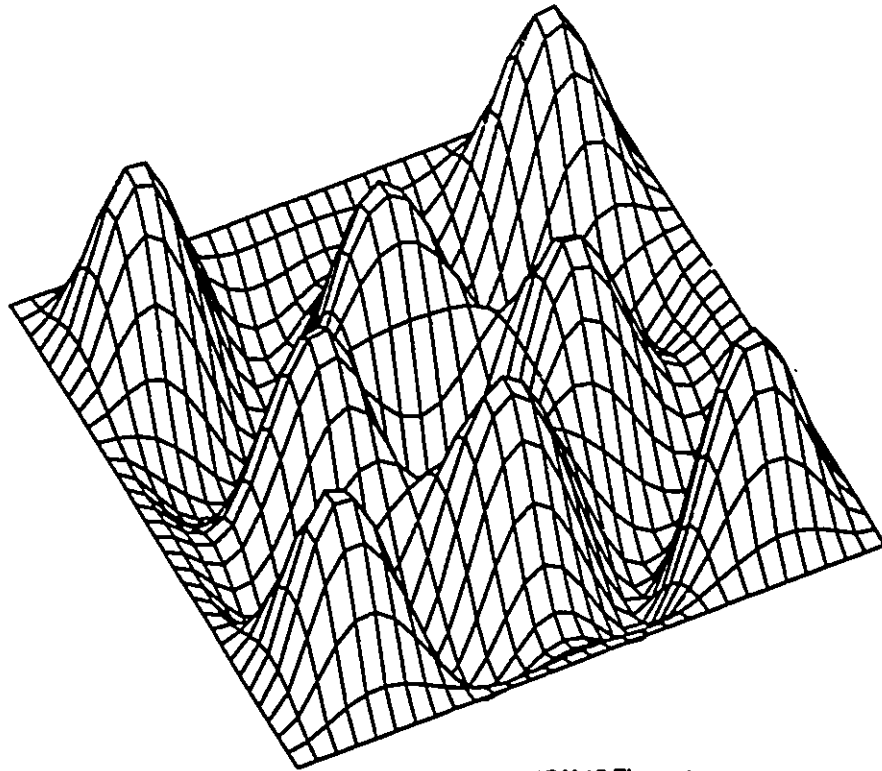
15 X 15 Elements
Mode 17 (8SS)
439.27 Hz
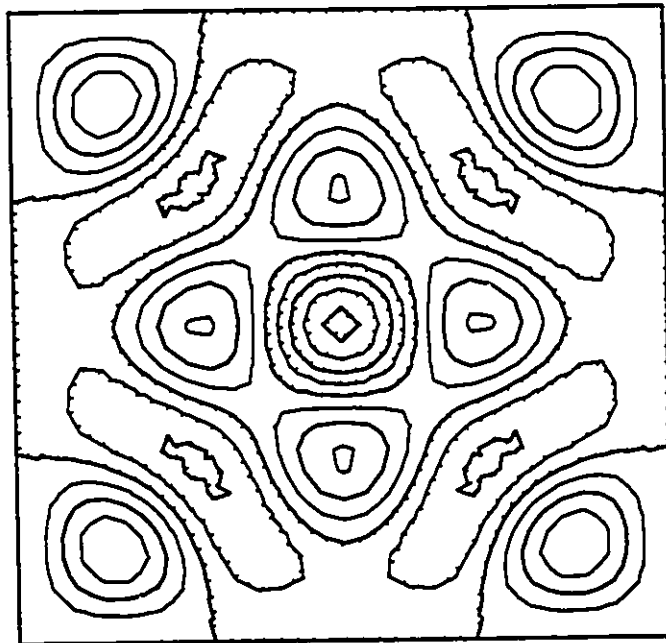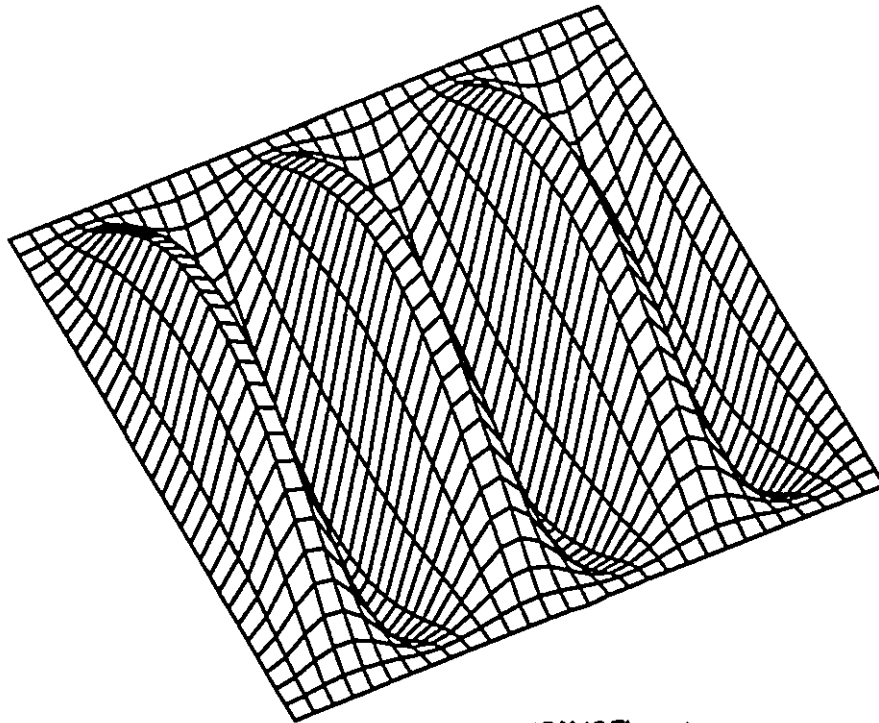
15 X 15 Elements
Mode 18 (6SA)
474.52 Hz
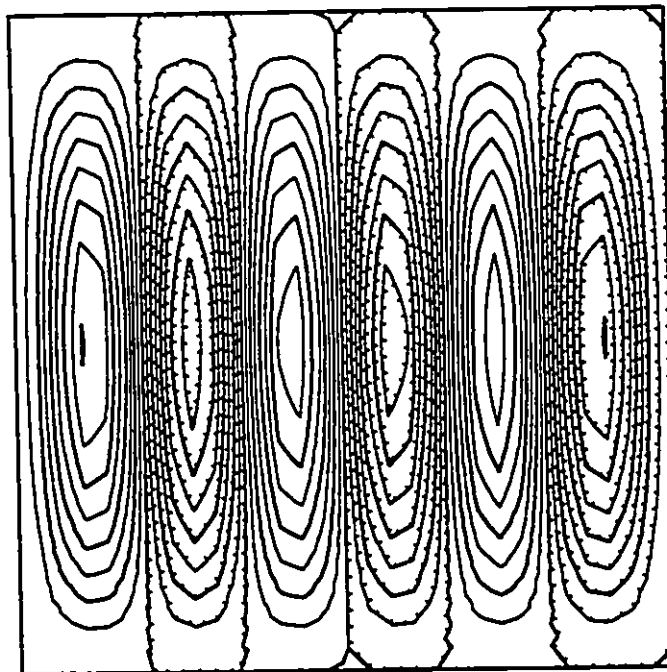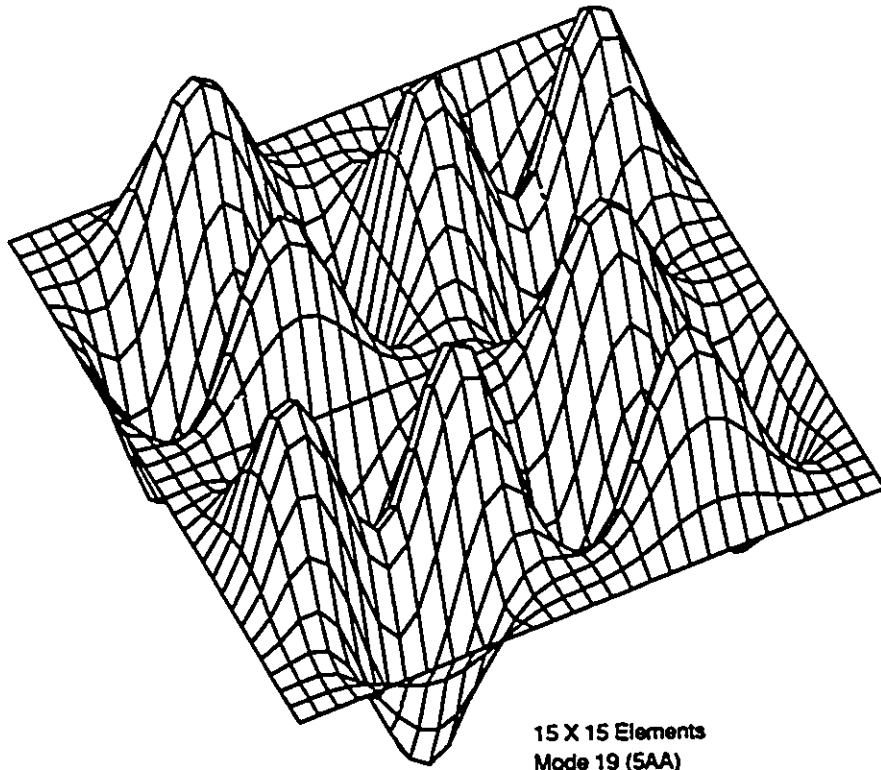
15 X 15 Elements
Mode 19 (5AA)
509.82 Hz
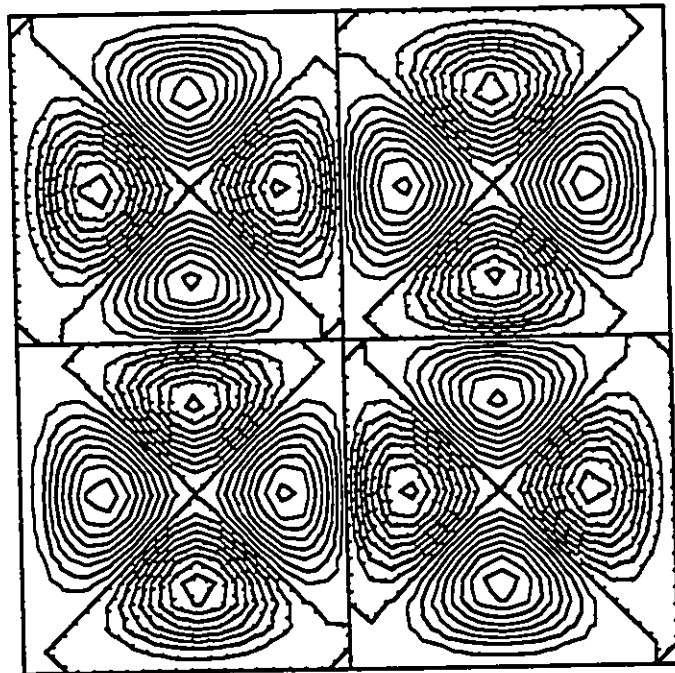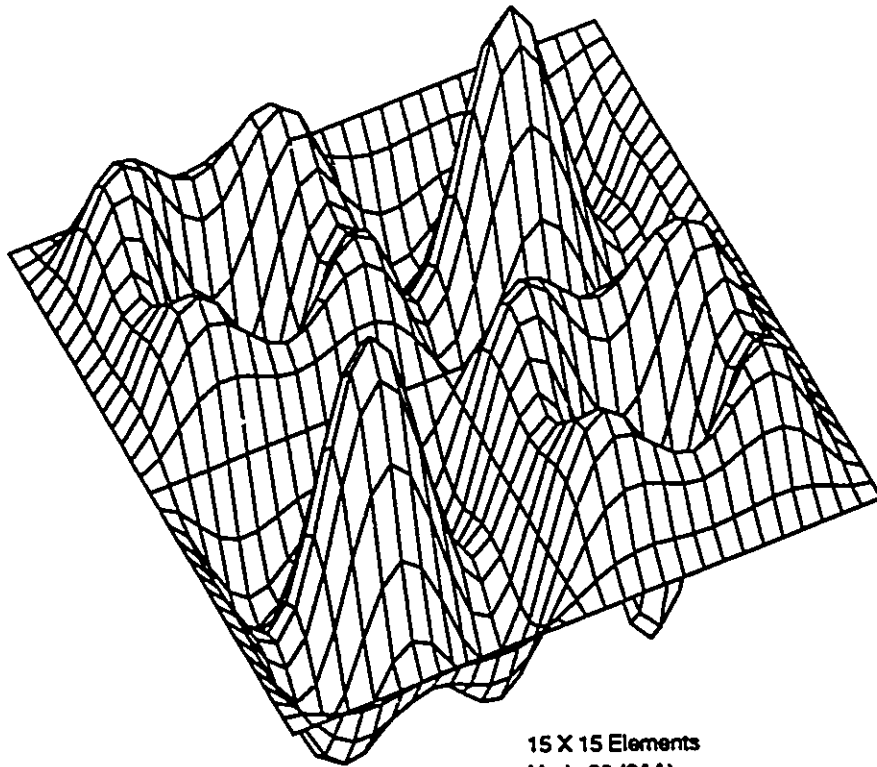
15 X 15 Elements
Mode 20 (6AA)
510.43 Hz
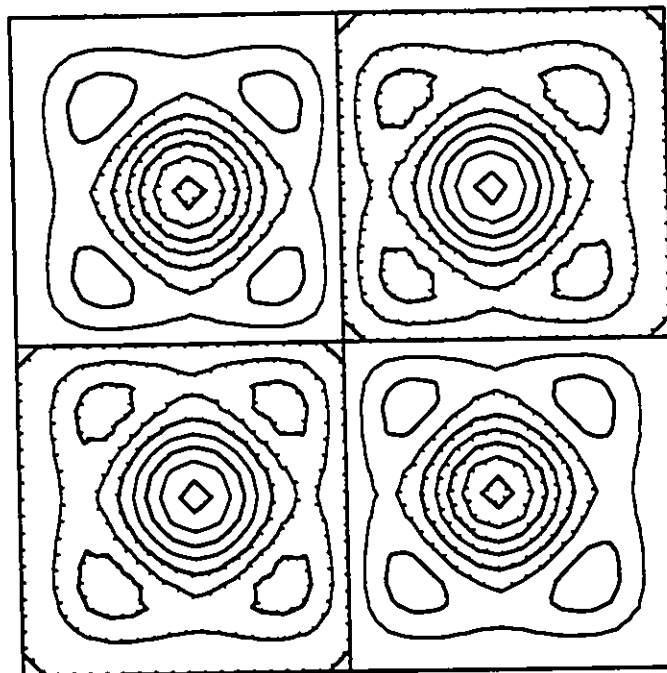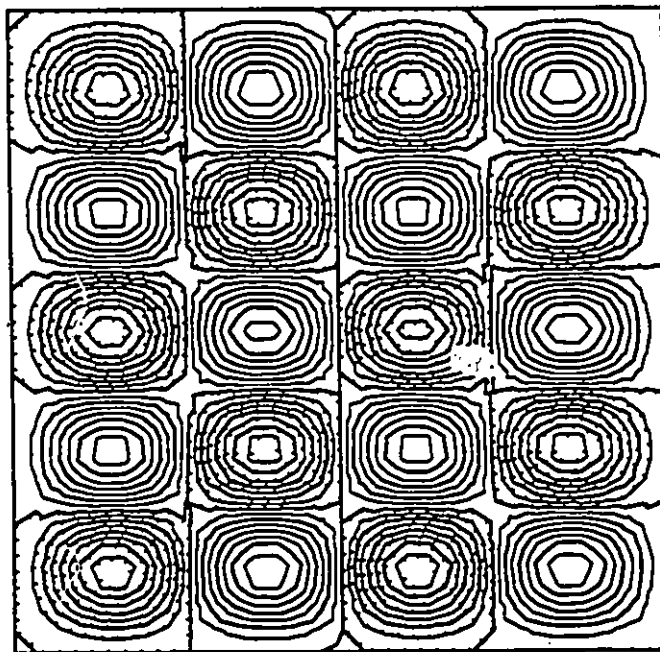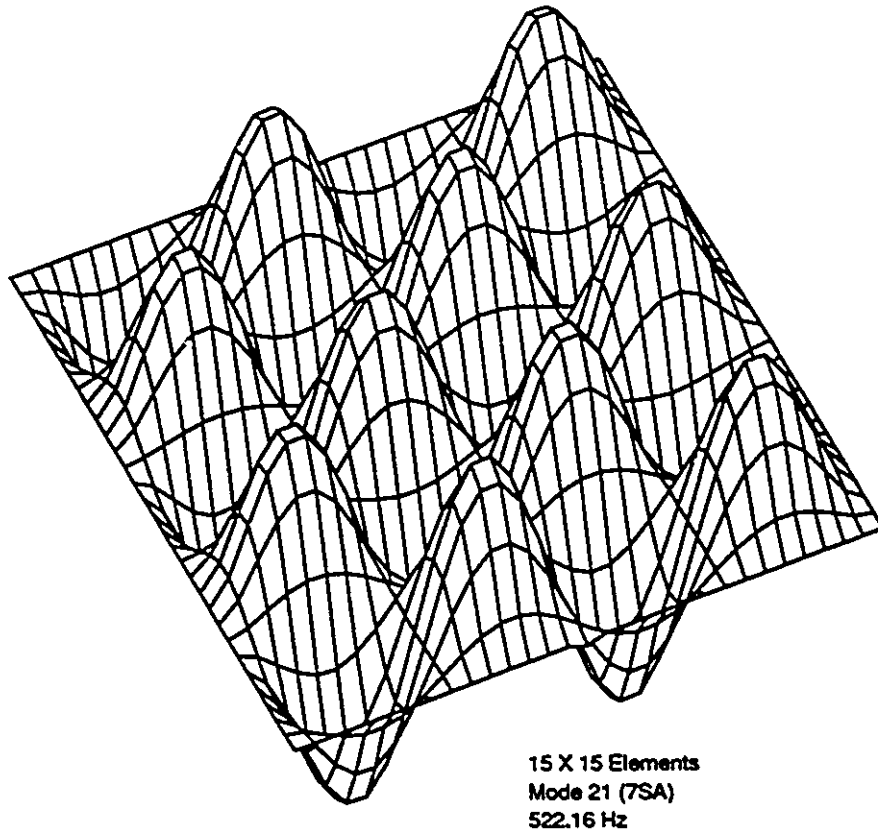
15 X 15 Elements
Mode 21 (7SA)
522.16 Hz
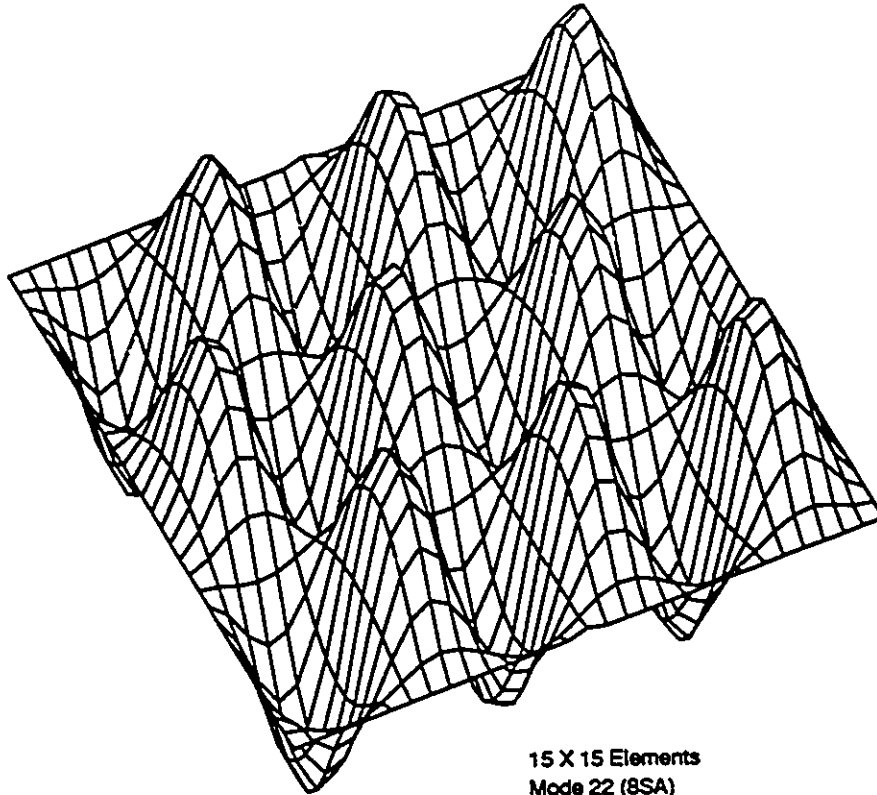
15 X 15 Elements
Mode 22 (8SA)
569.52 Hz
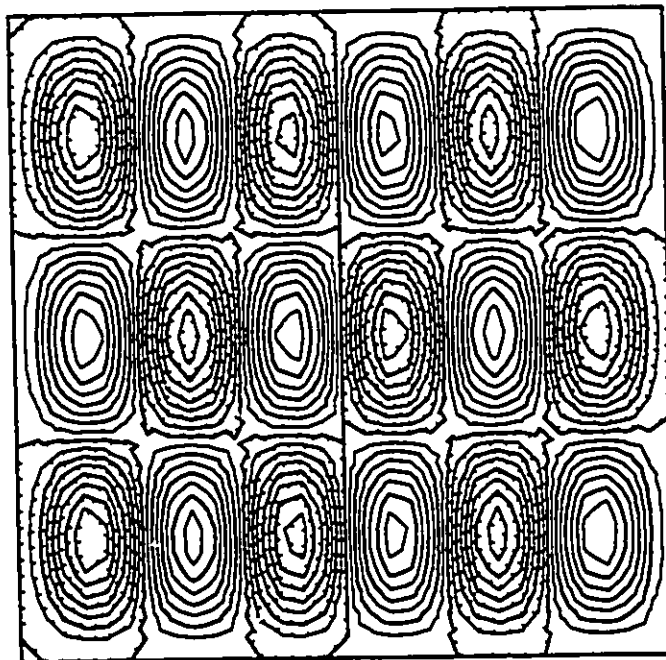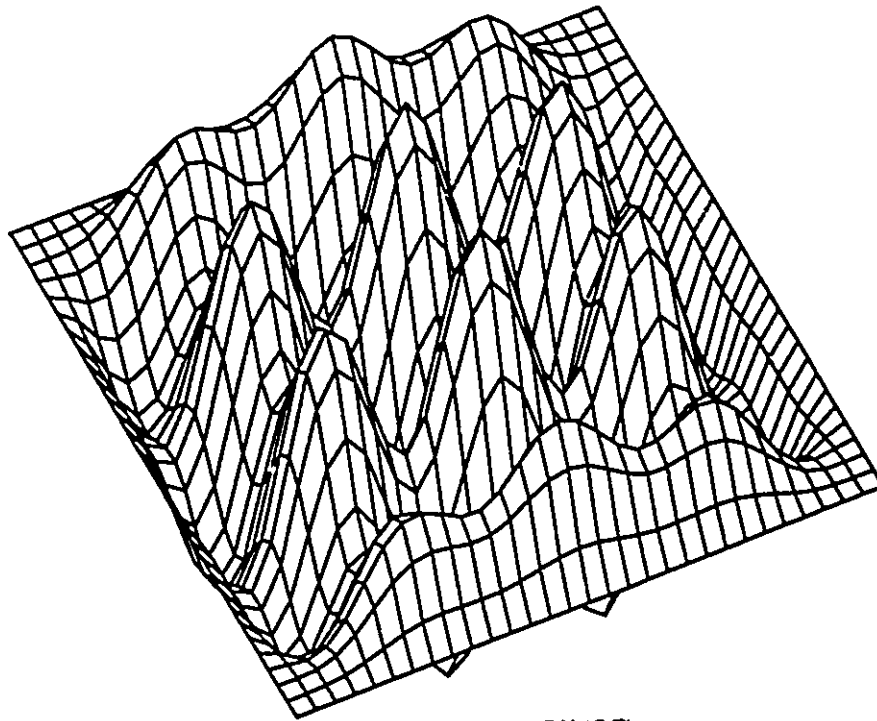
15 X 15 Elements
Mode 23 (9SS)
627.69 Hz
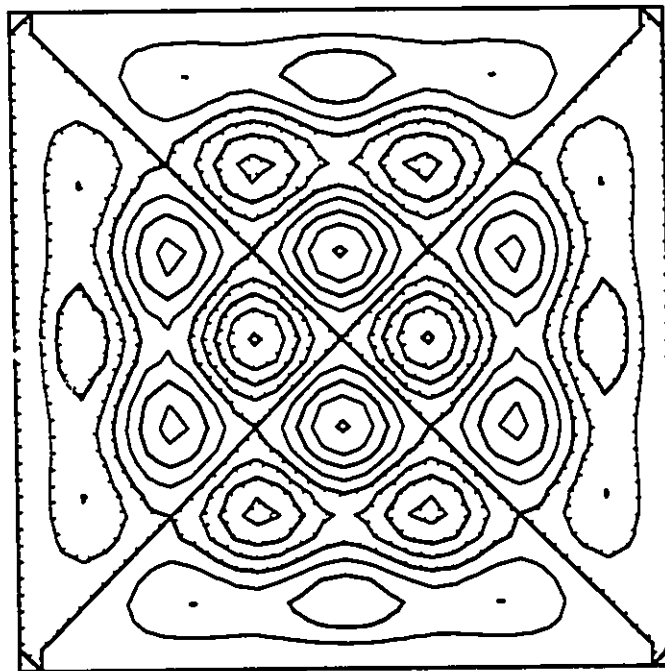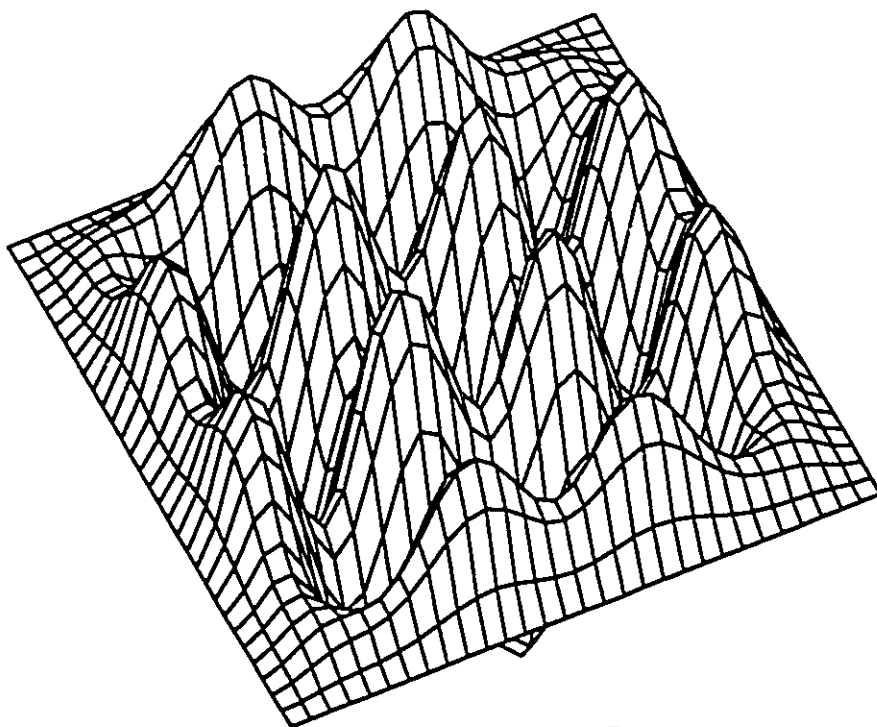
15 X 15 Elements
Mode 24 (10SS)
627.79 Hz
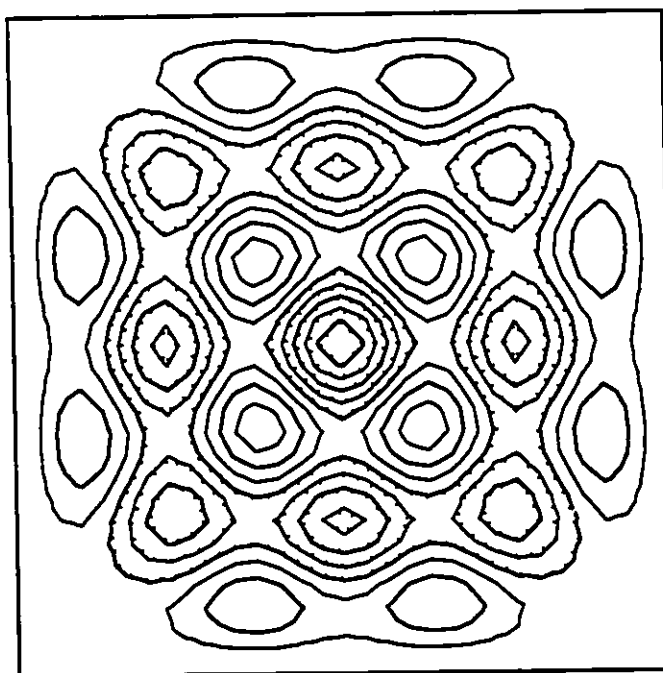
15 X 15 Elements
Mode 25 (11SS)
629.58 Hz
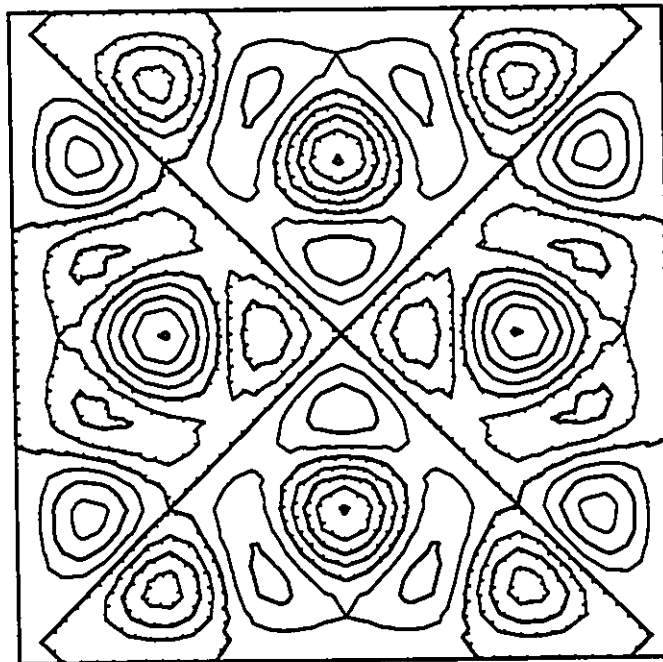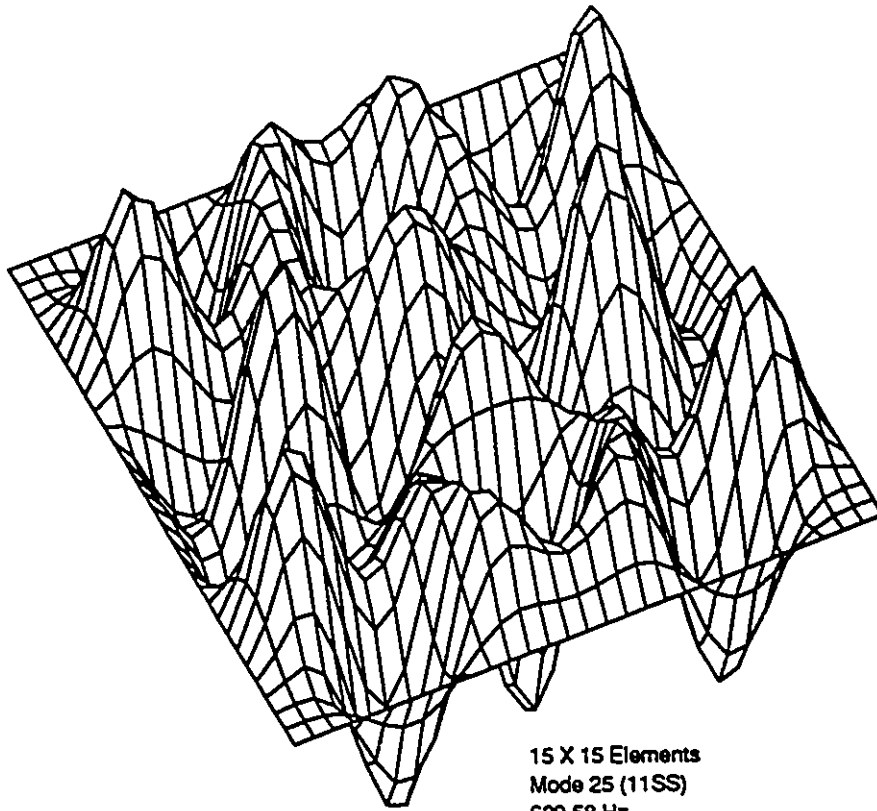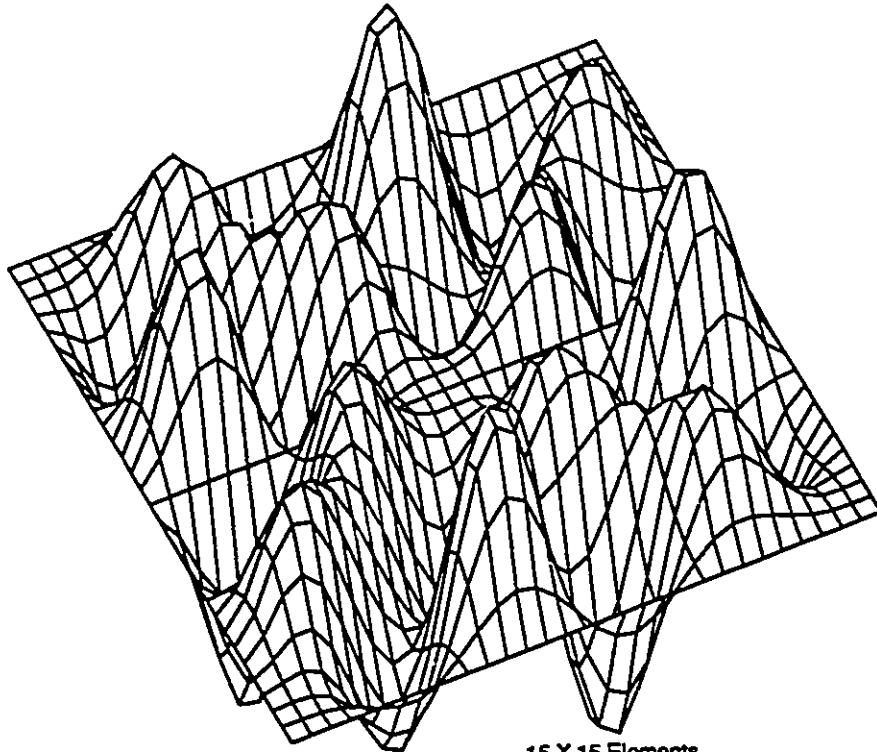
15 X 15 Elements
Mode 26 (7AA)
652.34 Hz

15 X 15 Elements
Mode 27 (8AA)
653.55 Hz

15 X 15 Elements
Mode 28 (9SA)
663.32 Hz

15 X 15 Elements
Mode 29 (12SS)
722.45 Hz
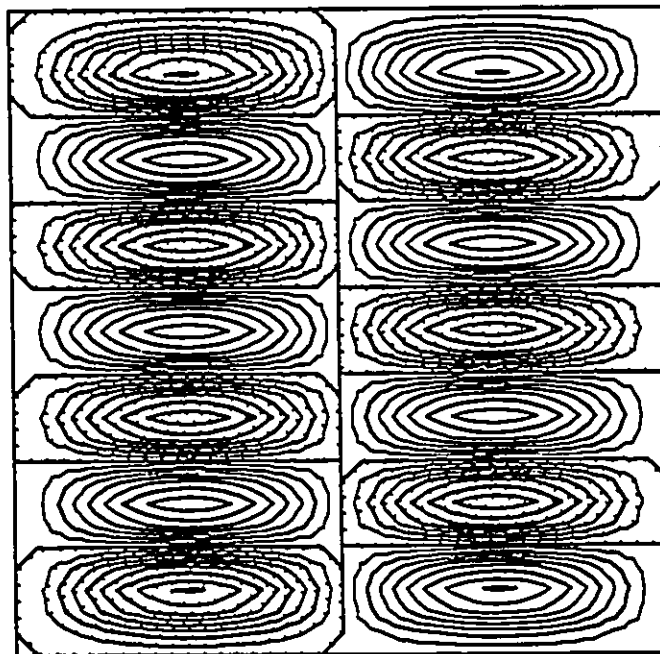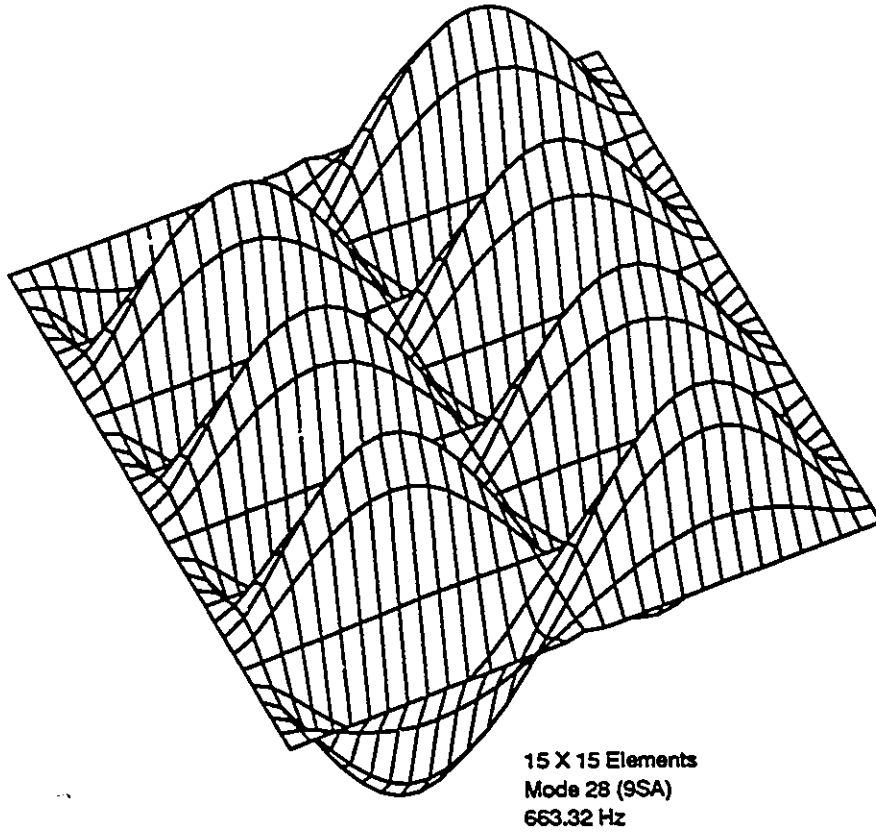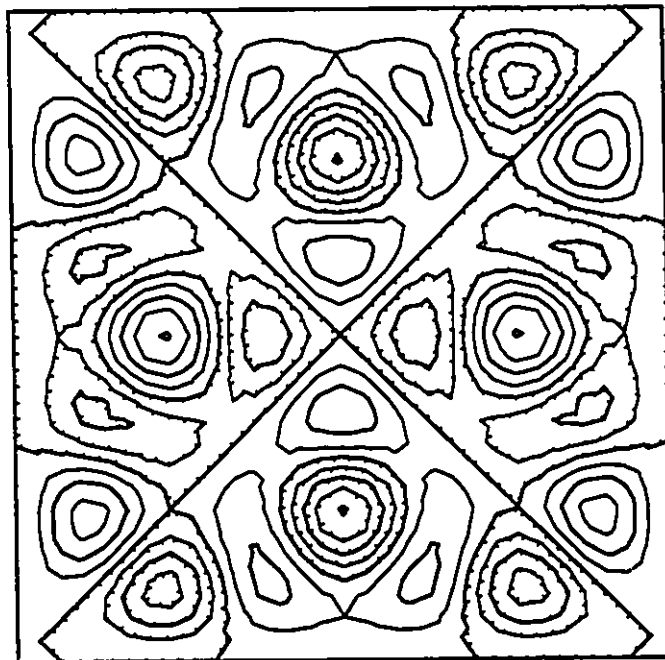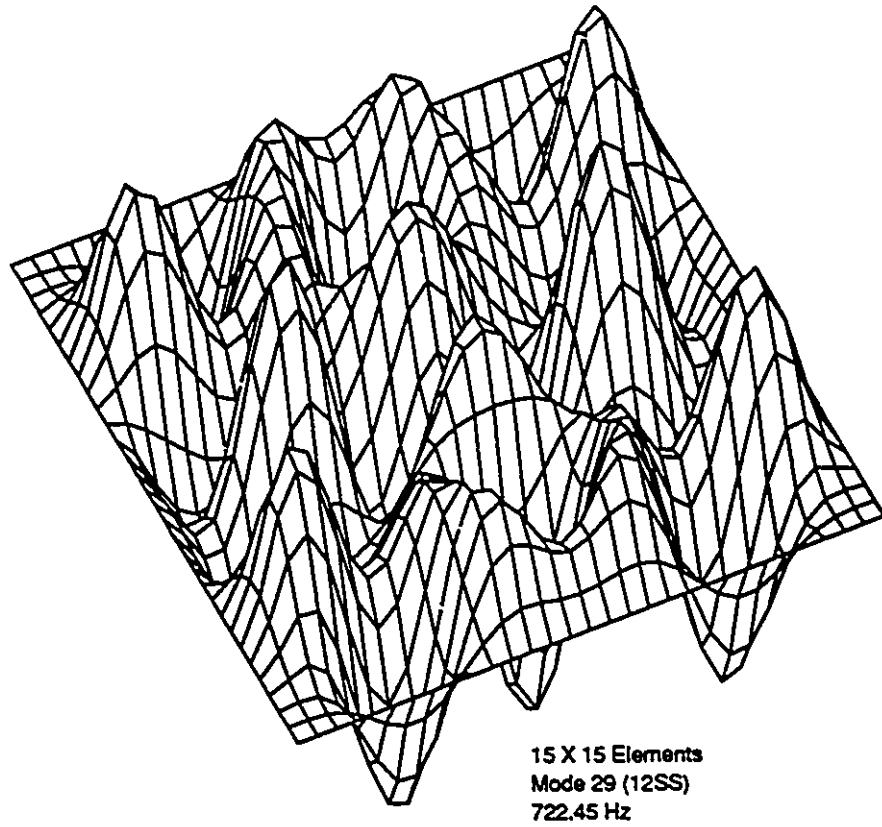
15 X 15 Elements
Mode 30 (13SS)
723.26 Hz
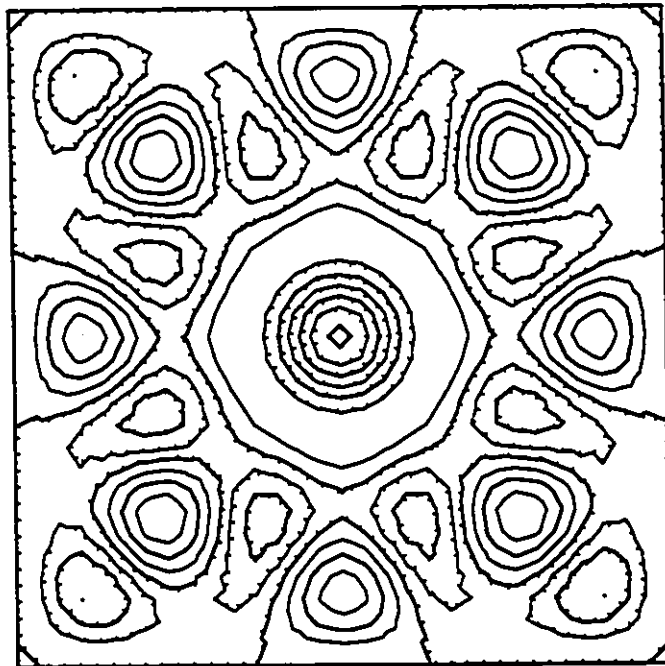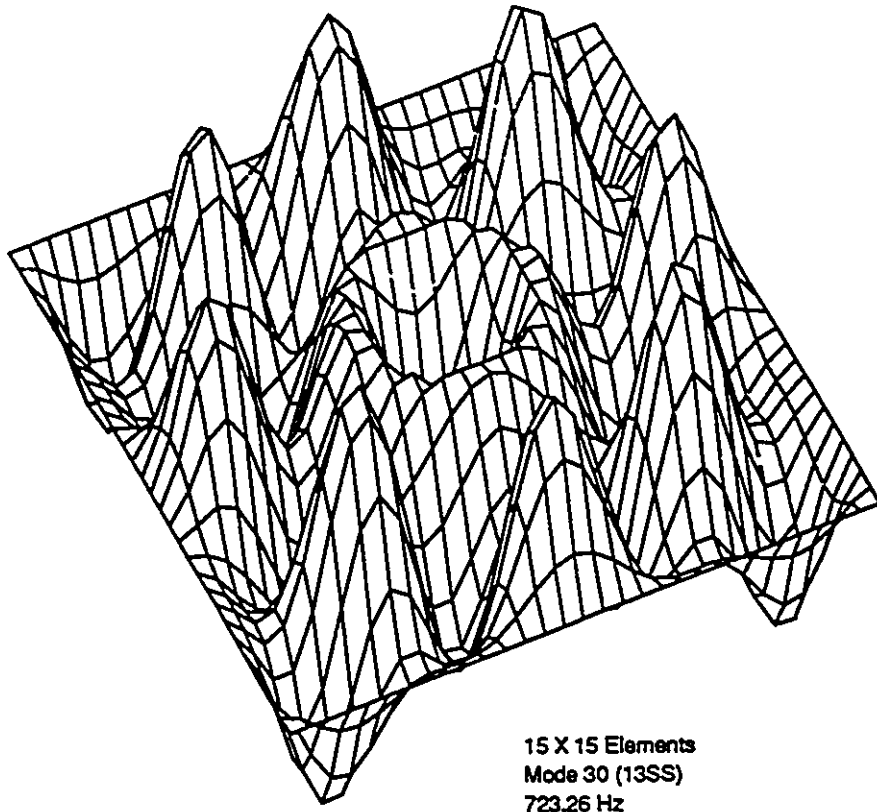
15 X 15 Elements
Mode 31 (10SA)
759.77 Hz
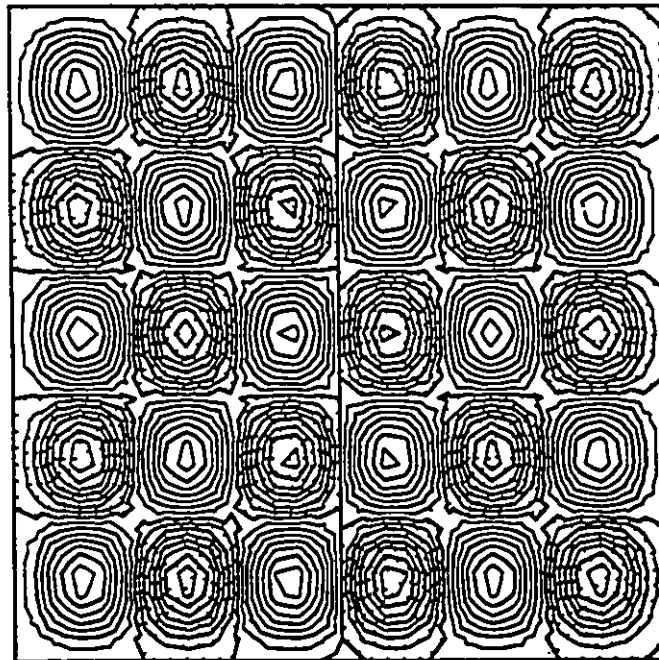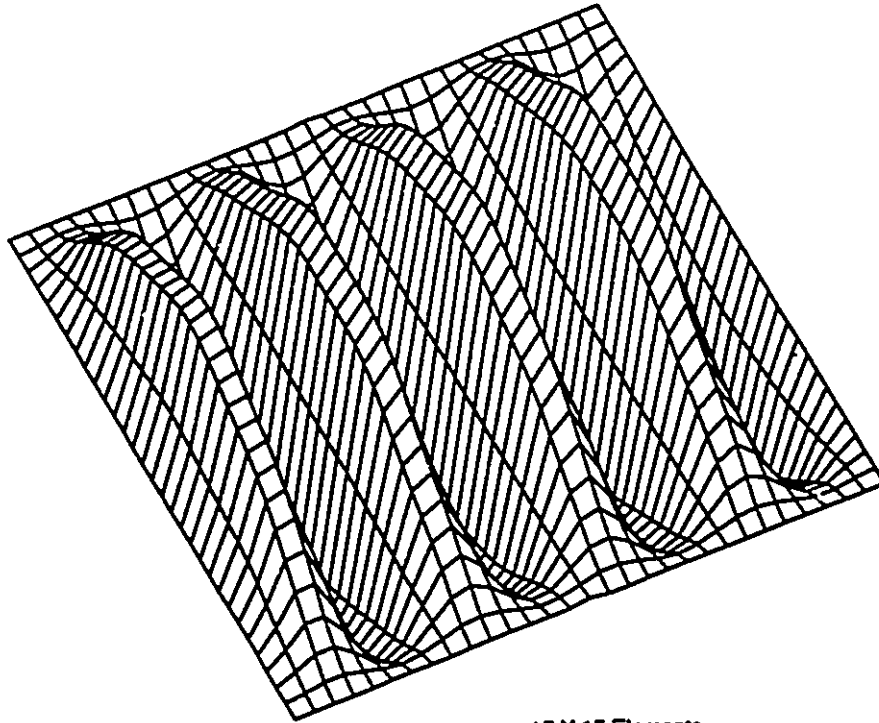
15 X 15 Elements
Mode 32 (11SA)
802.80 Hz
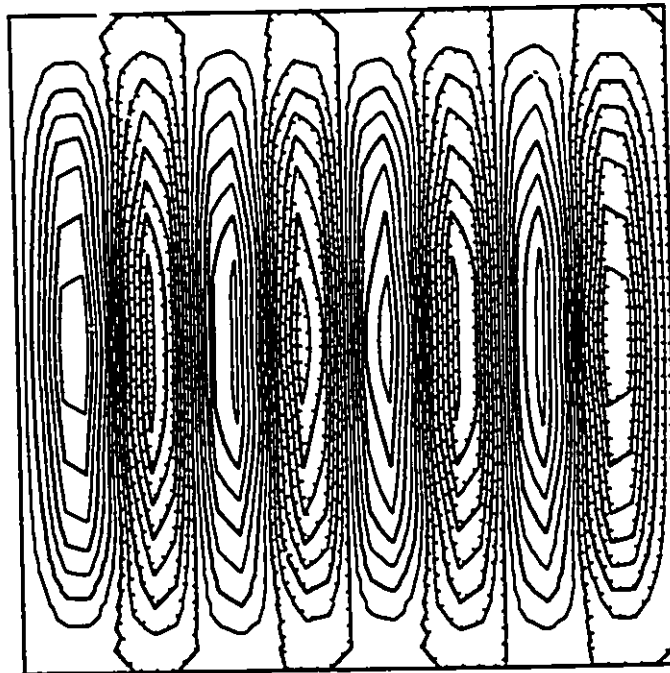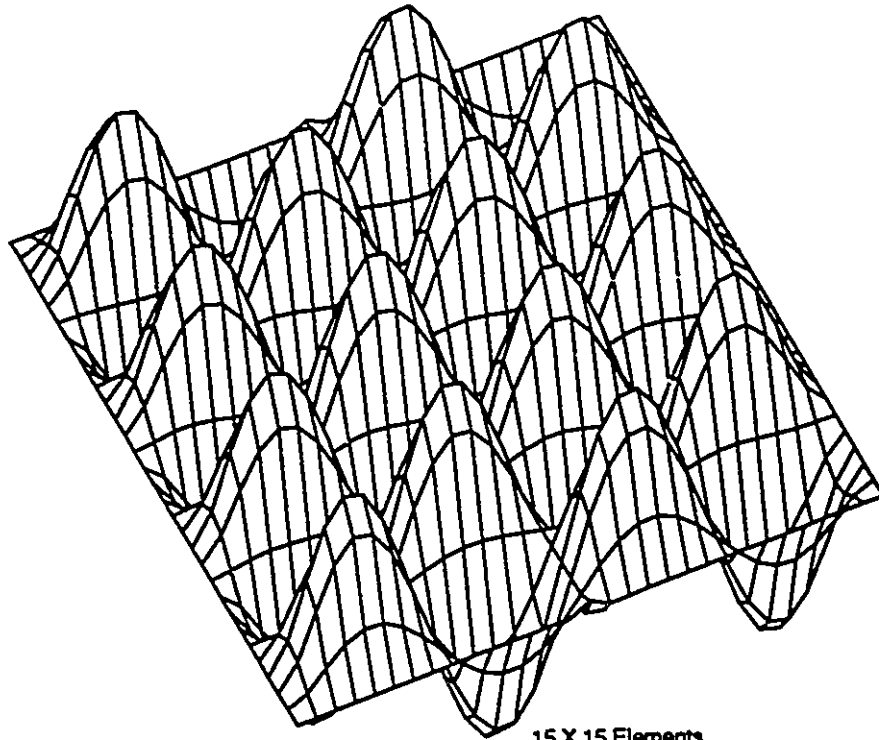
15 X 15 Elements
Mode 33 (12SA)
806.03 Hz
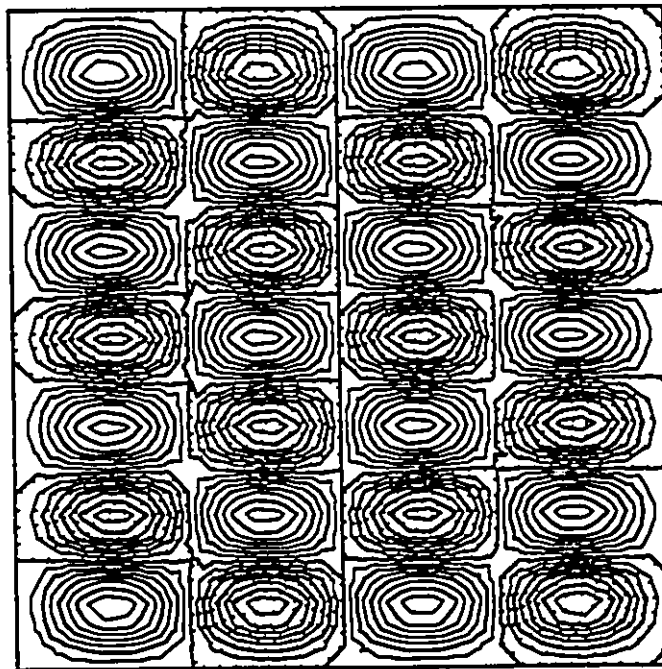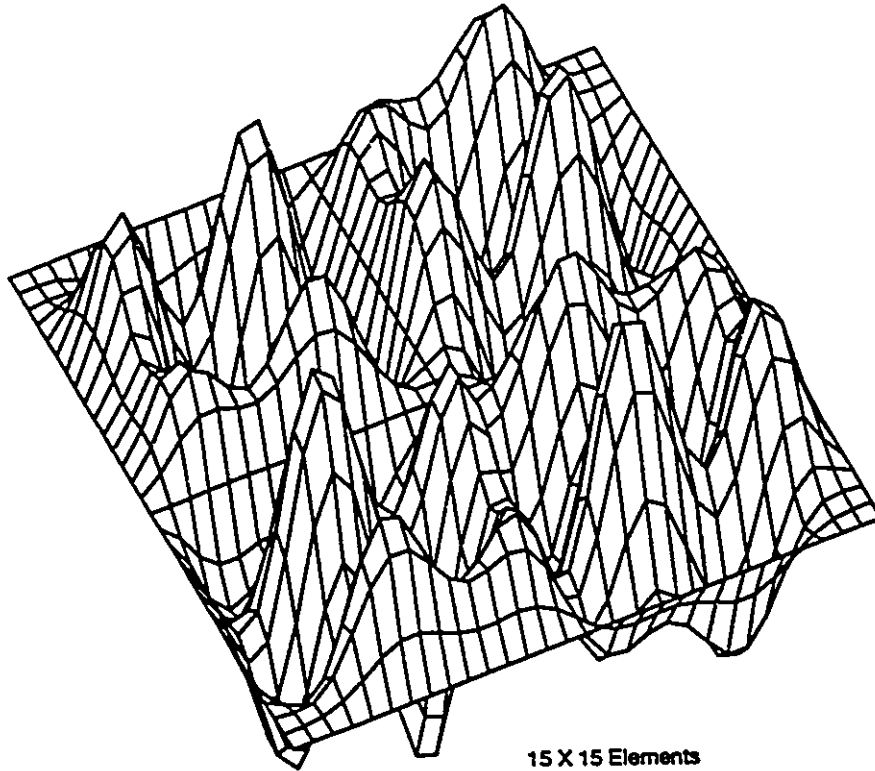
15 X 15 Elements
Mode 34 (9AA)
838.38 Hz
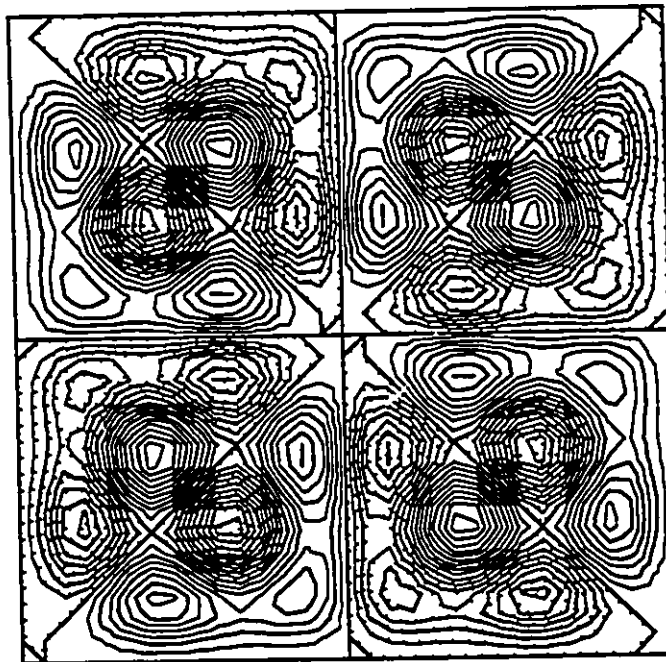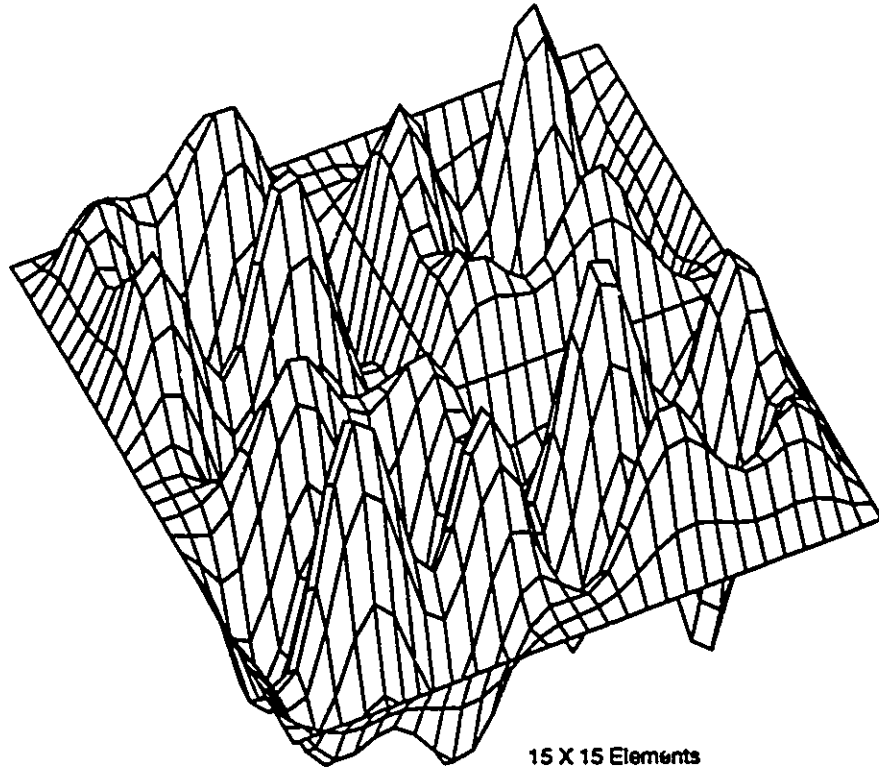
15 X 15 Elements
Mode 35 (10AA)
838.74 Hz
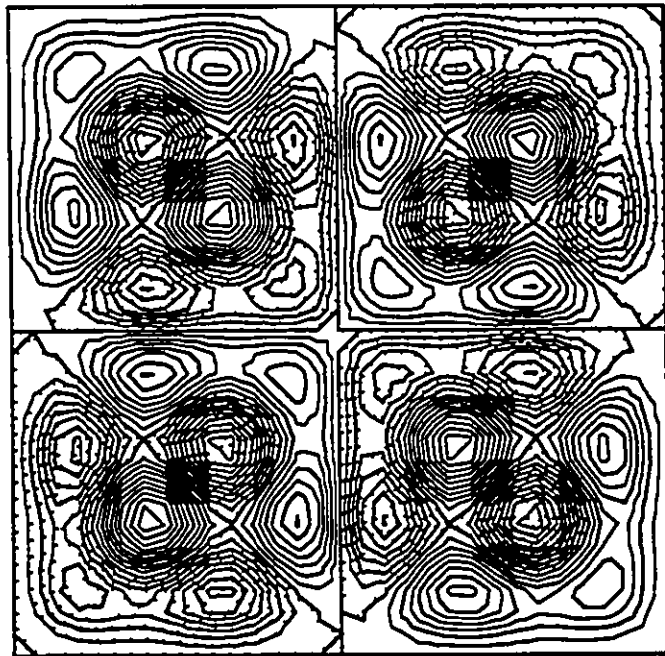
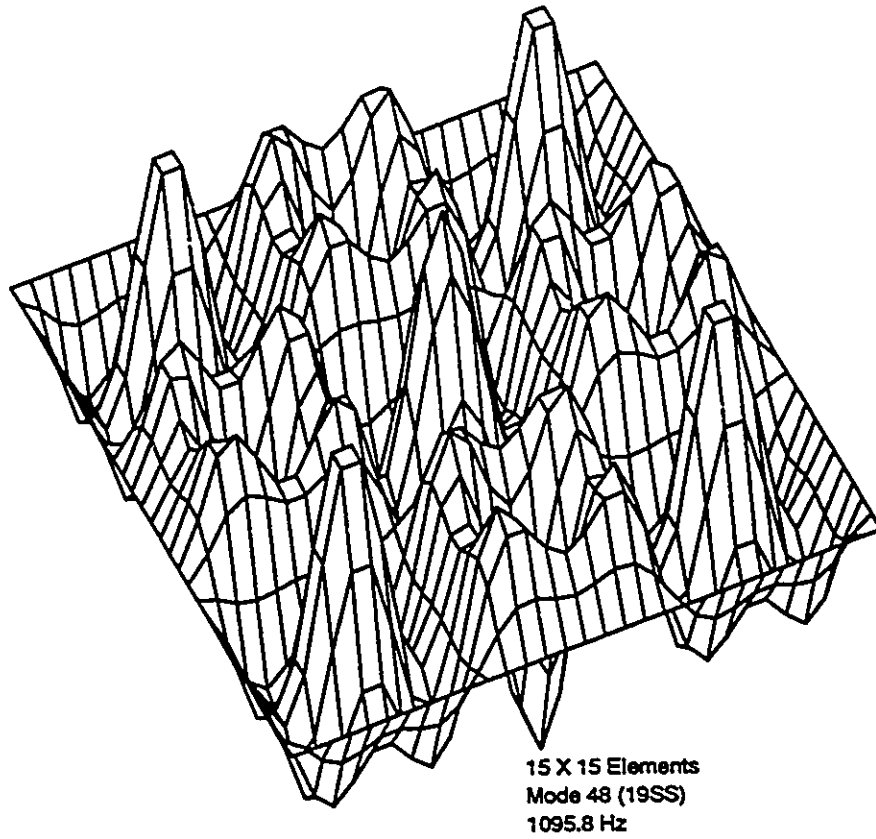15 X 15 Elements
Mode 36 (11AA)
890.55 Hz
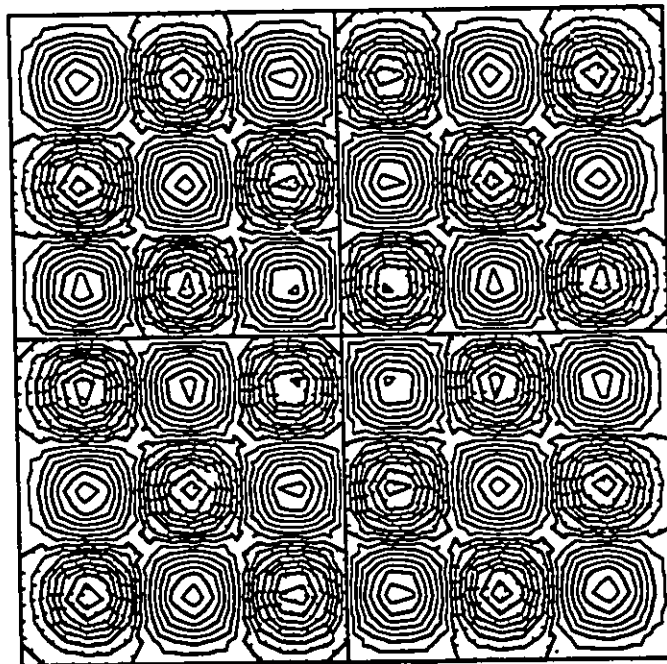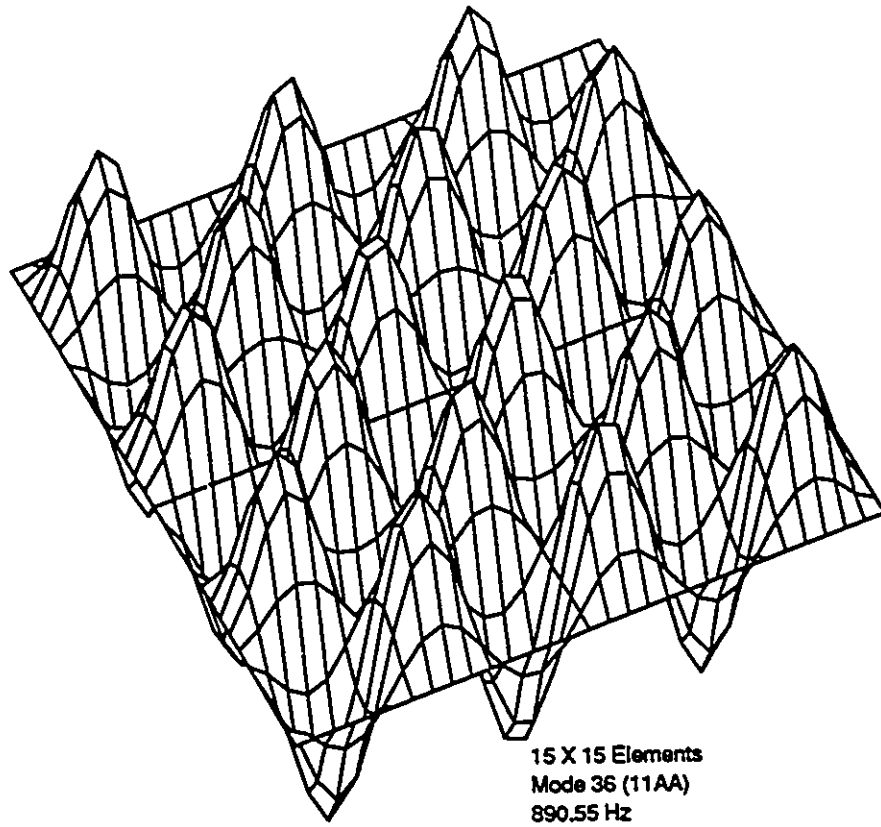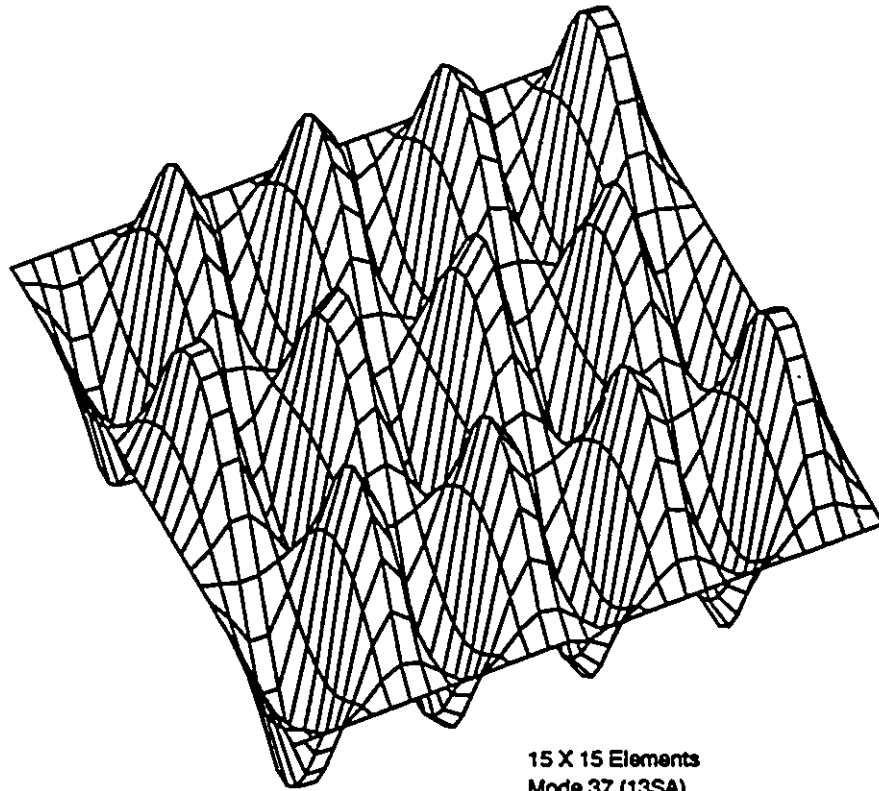
15 X 15 Elements
Mode 37 (13SA)
898.11 Hz

15 X 15 Elements
Mode 38 (14SS)
912.83 Hz
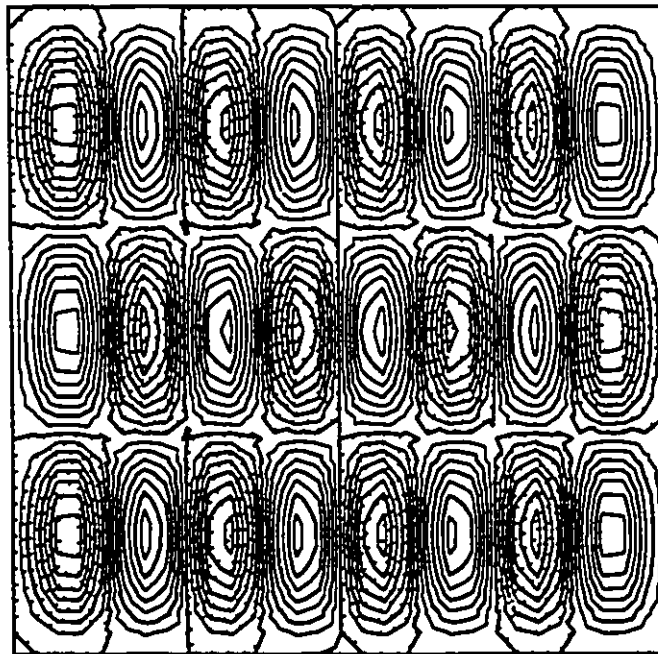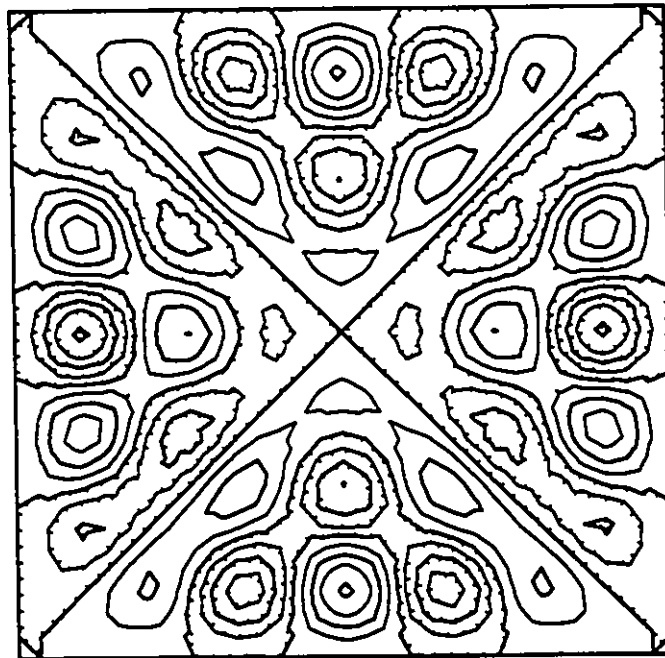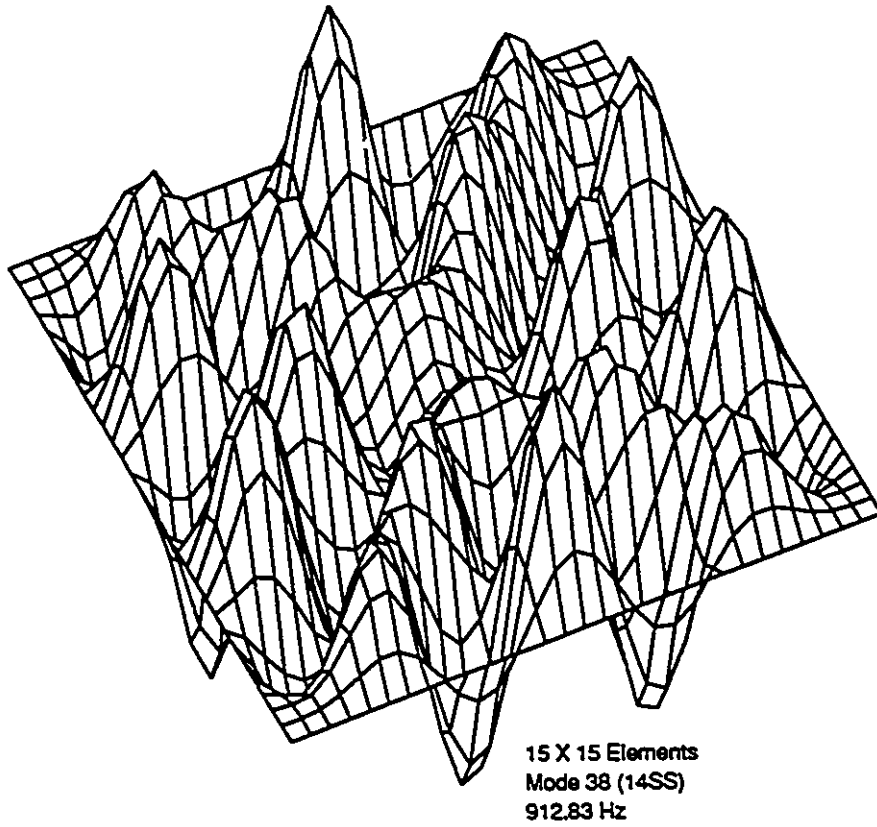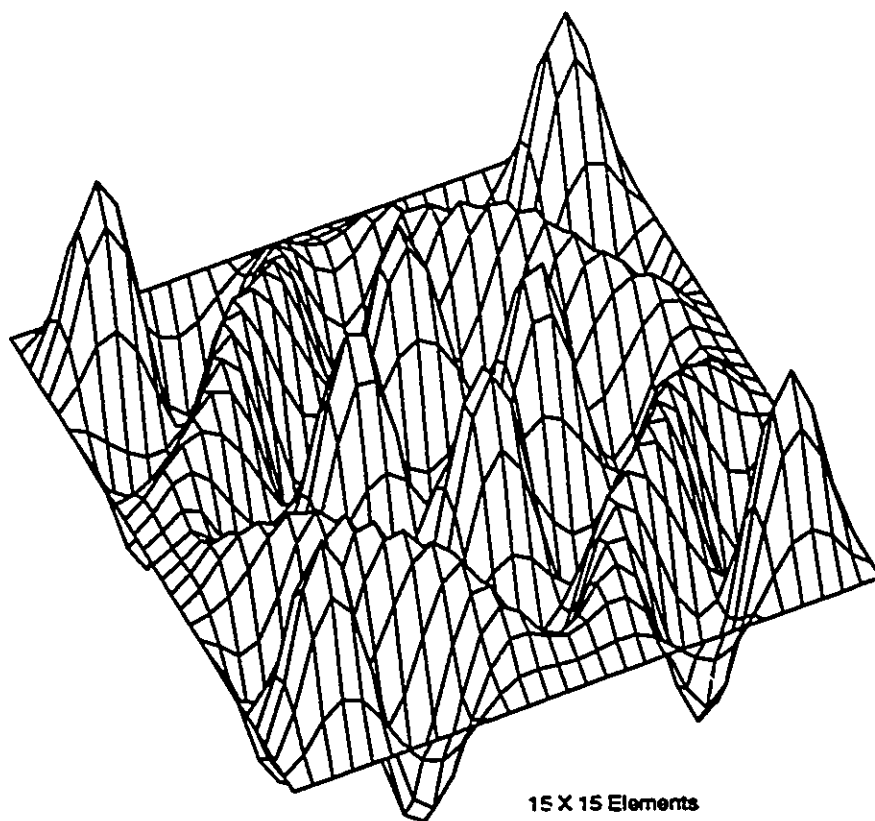
15 X 15 Elements
Mode 39 (15SS)
914.01 Hz

15 X 15 Elements
Mode 40 (12AA)
981.42 Hz
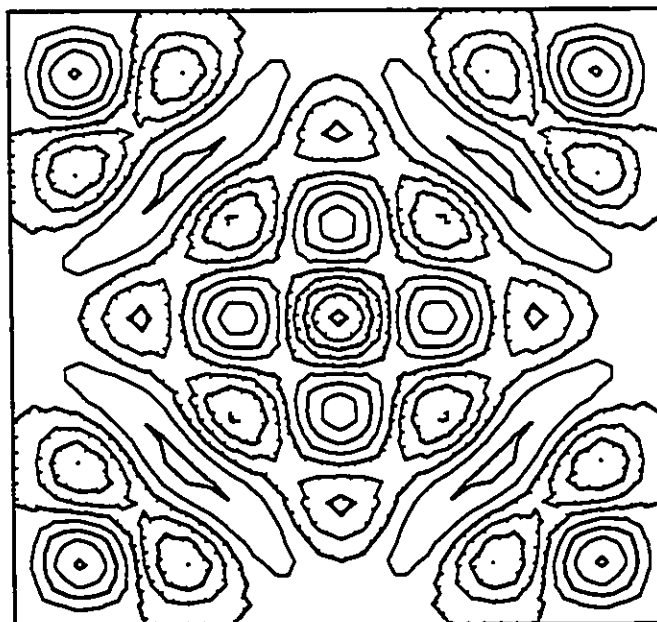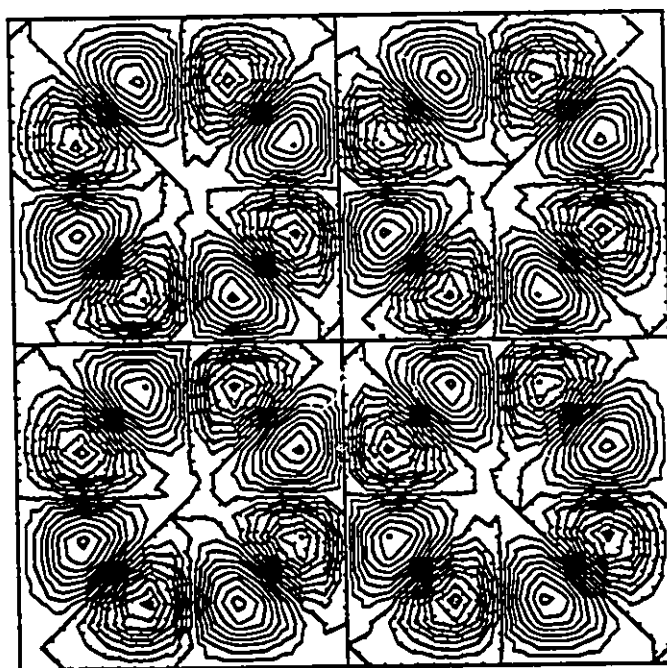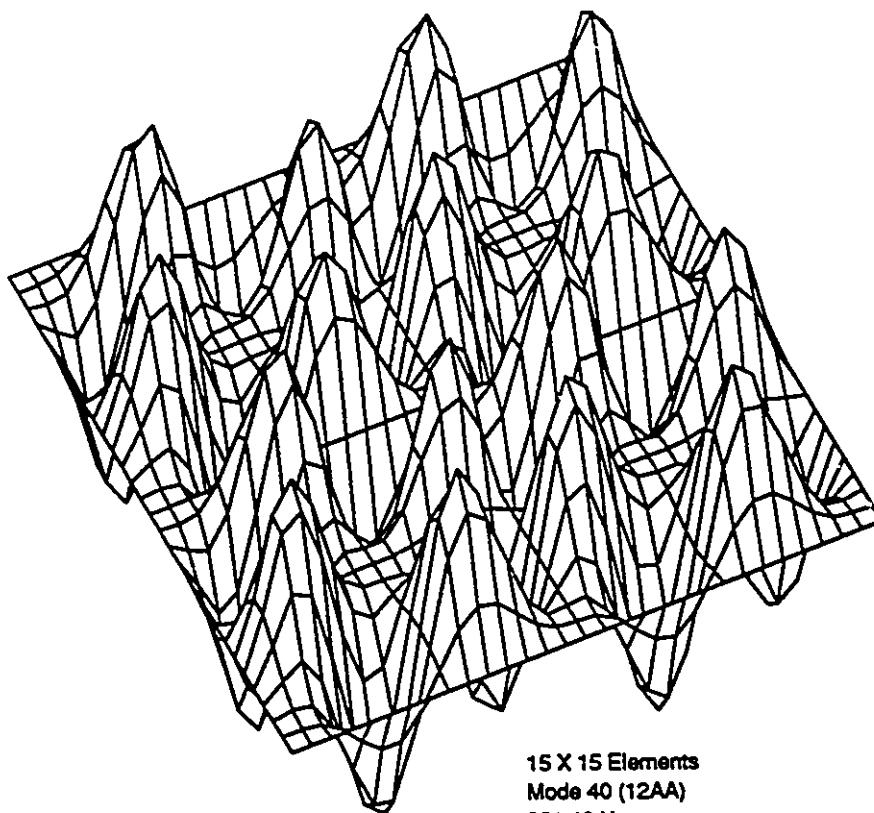
15 X 15 Elements
Mode 41 (13AA)
982.32 Hz
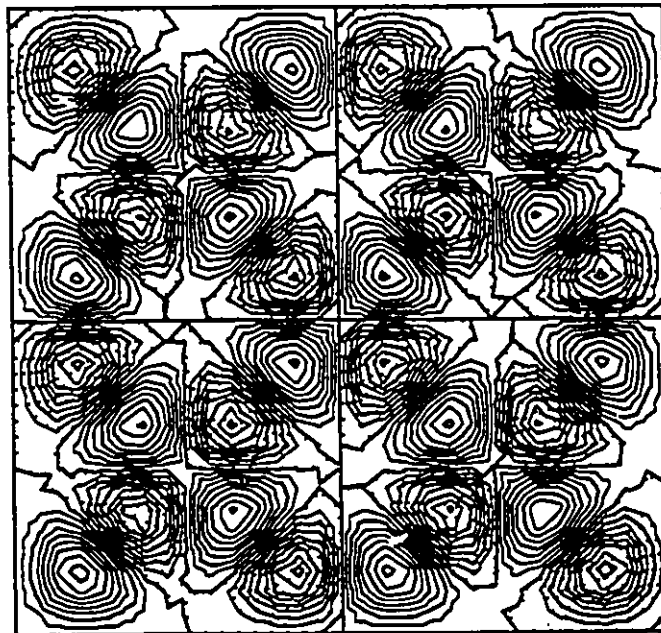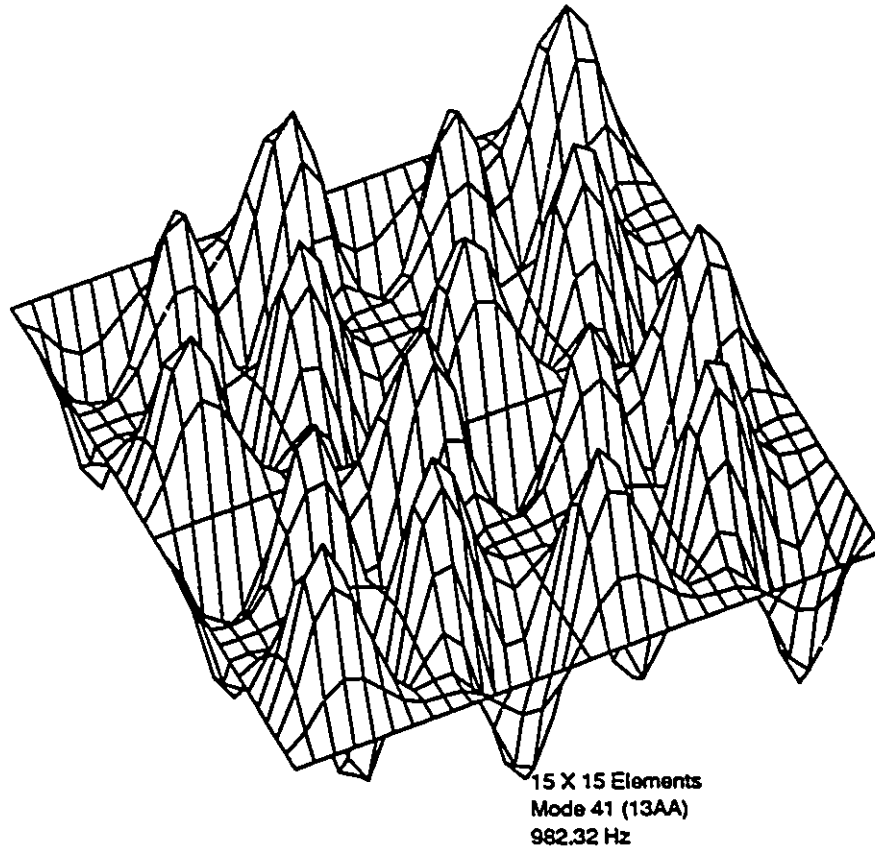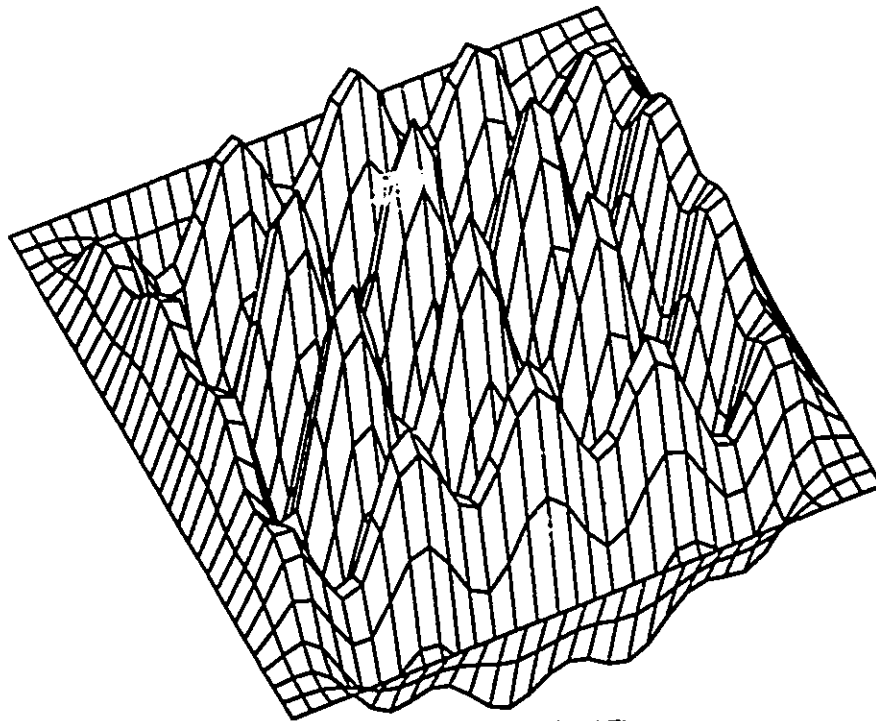
15 X 15 Elements
Mode 42 (16SS)
999.54 Hz
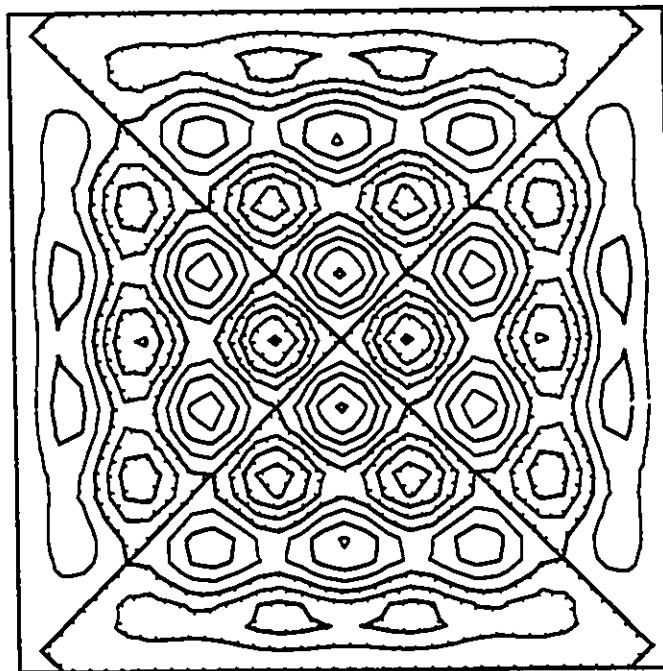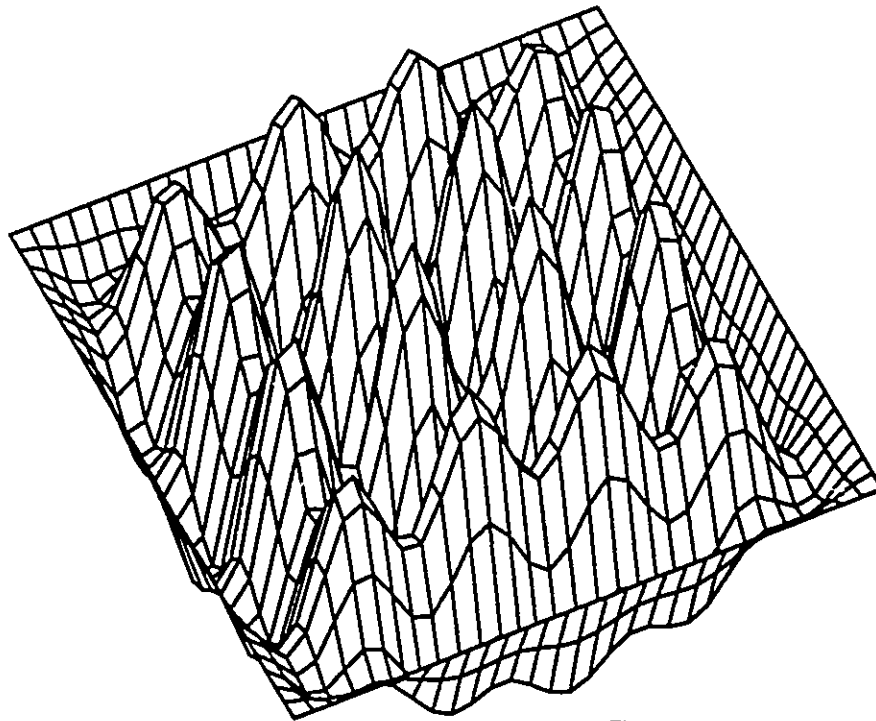
15 X 15 Elements
Mode 43 (17SS)
999.62 Hz
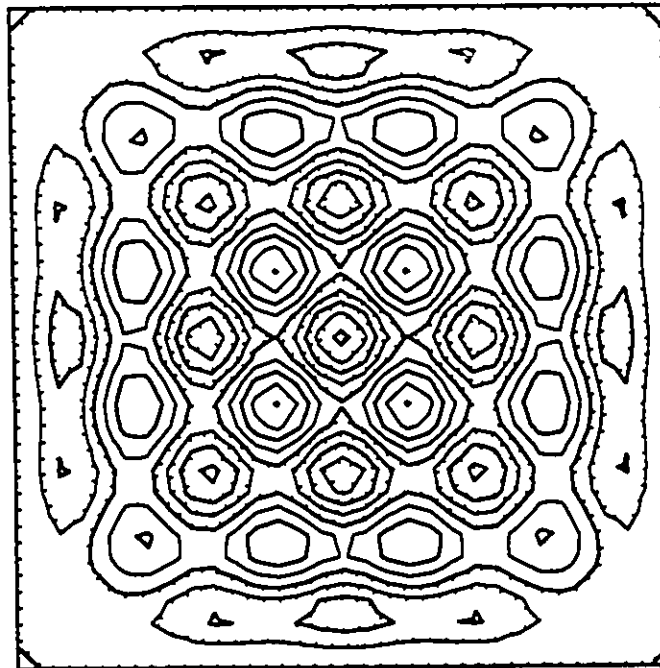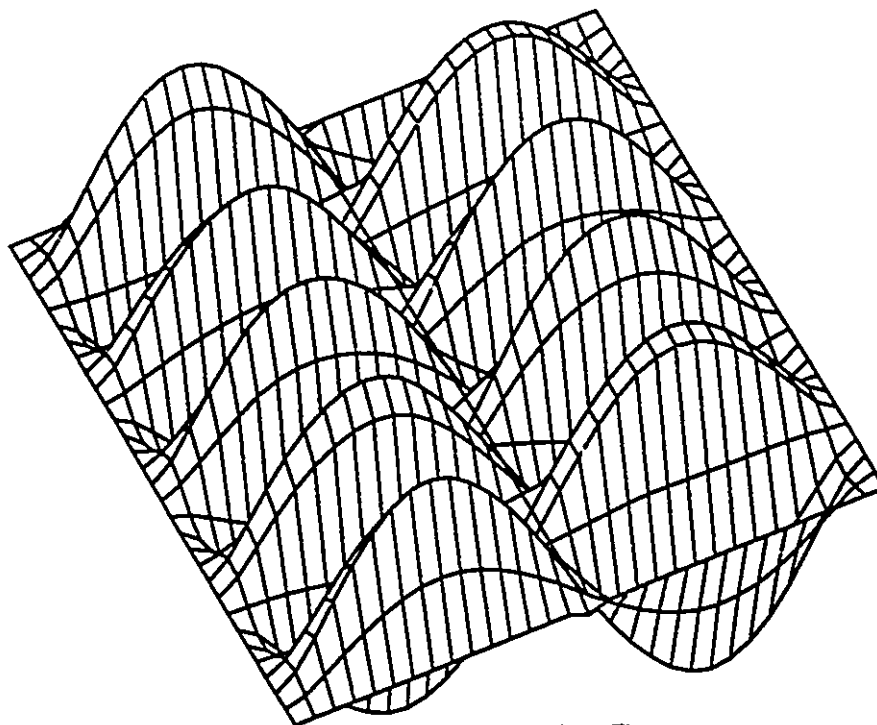
15 X 15 Elements
Mode 44 (14SA)
1035.4 Hz
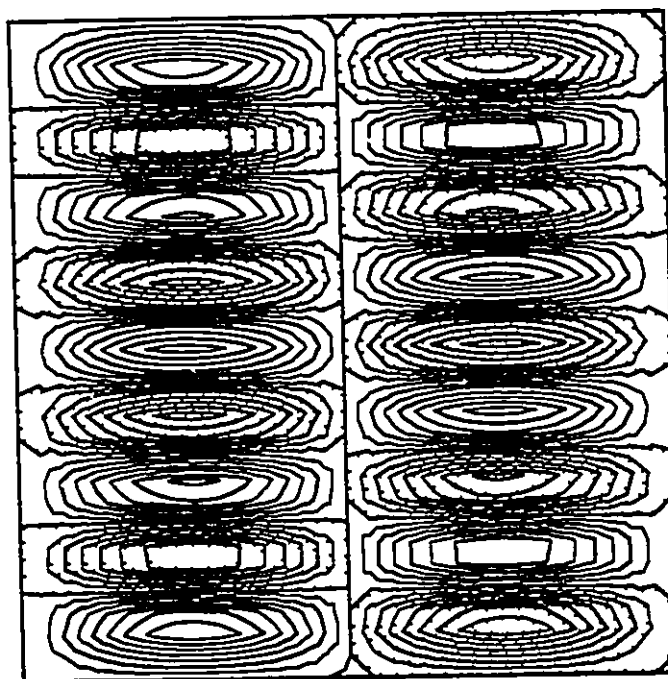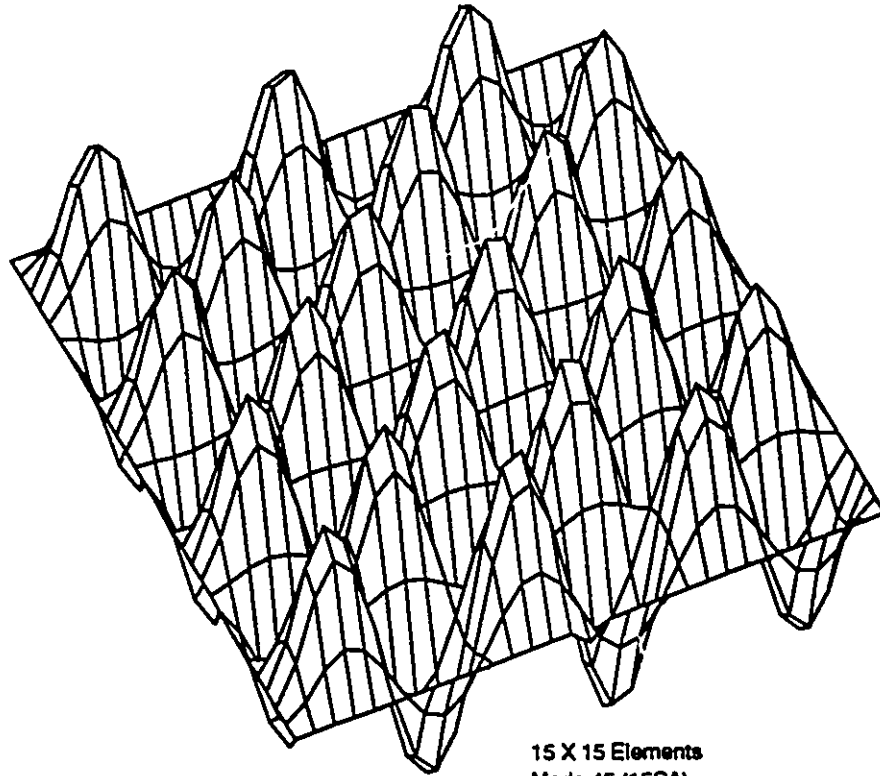
15 X 15 Elements
Mode 45 (15SA)
1043.8 Hz

15 X 15 Elements
Mode 46 (16SA)
1089.2 Hz
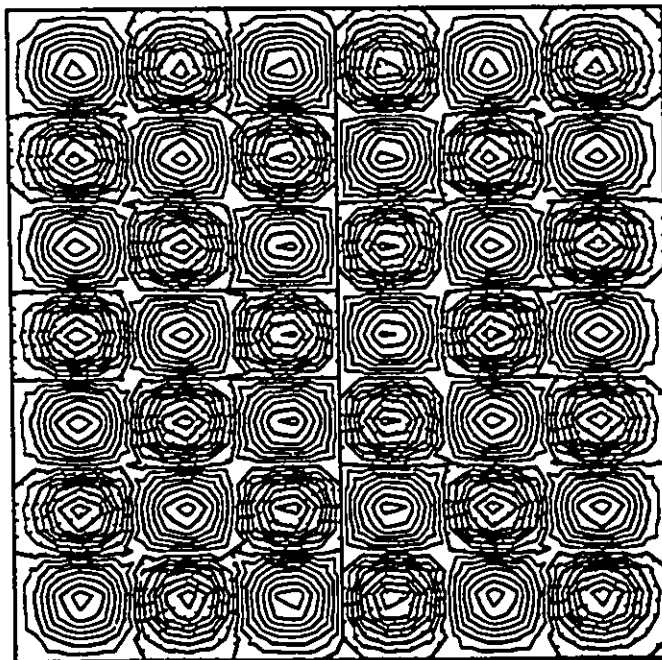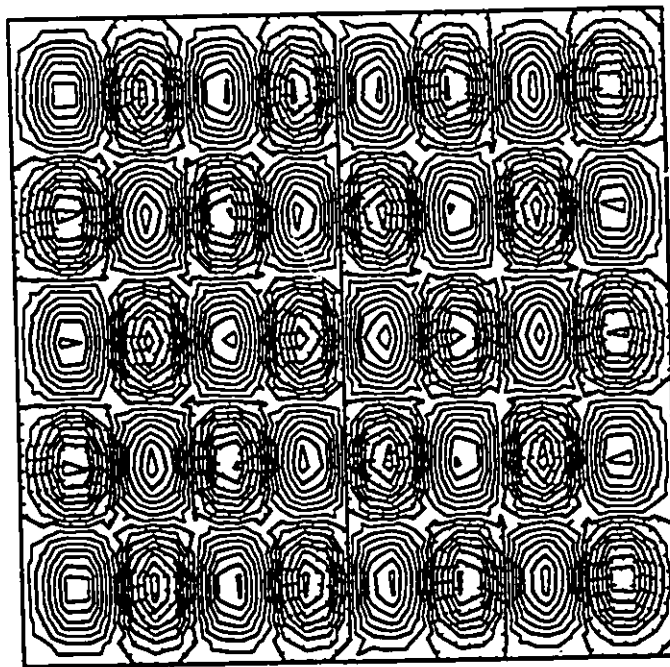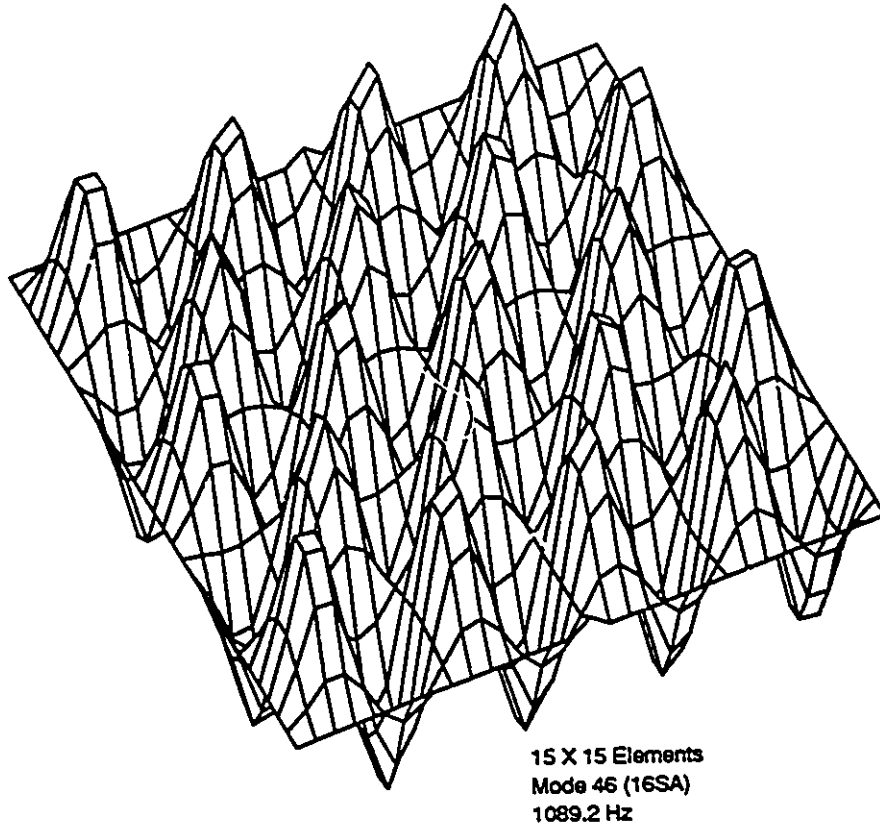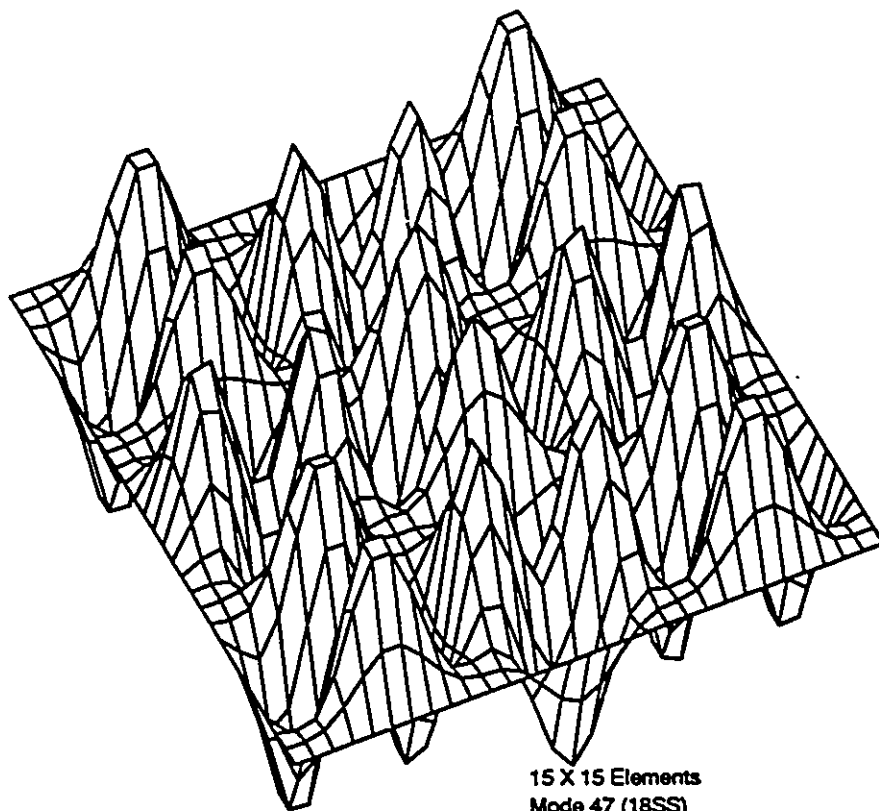
15 X 15 Elements
Mode 47 (18SS)
1095.3 Hz

15 X 15 Elements
Mode 48 (19SS)
1095.8 Hz

15 X 15 Elements
Mode 49 (17SA)
1179.3 Hz

15 X 15 Elements
Mode 50 (20SS)
1198.4 Hz
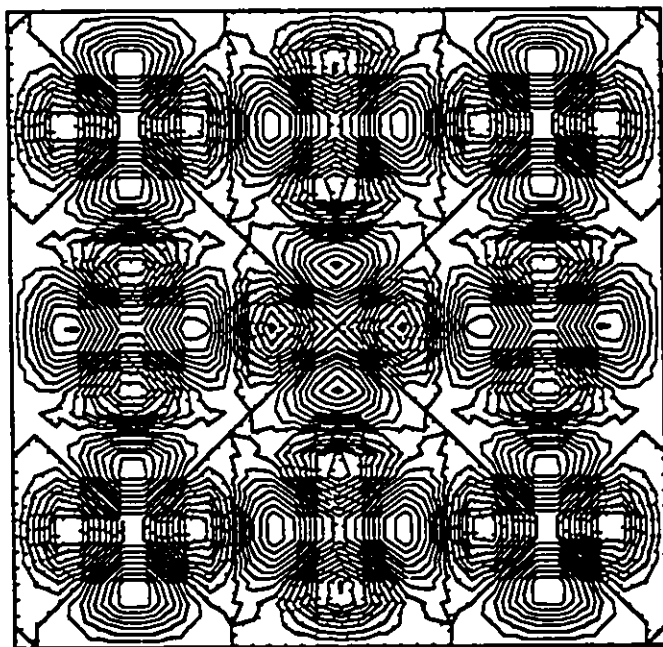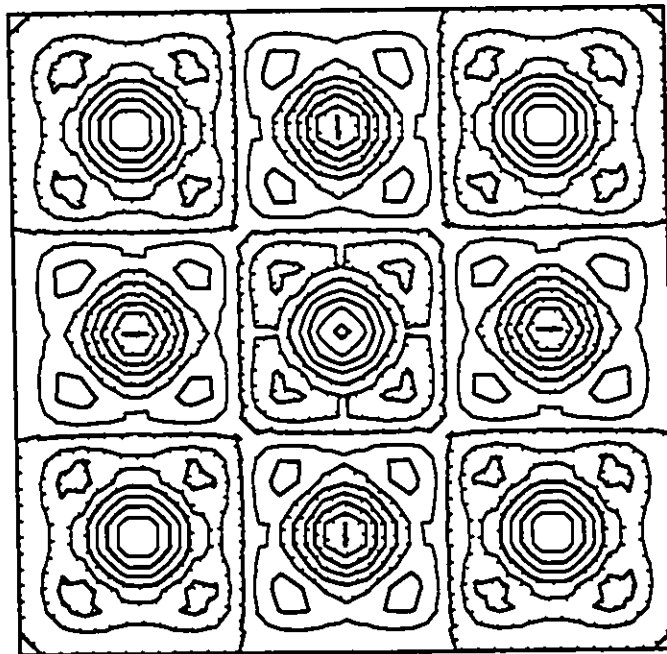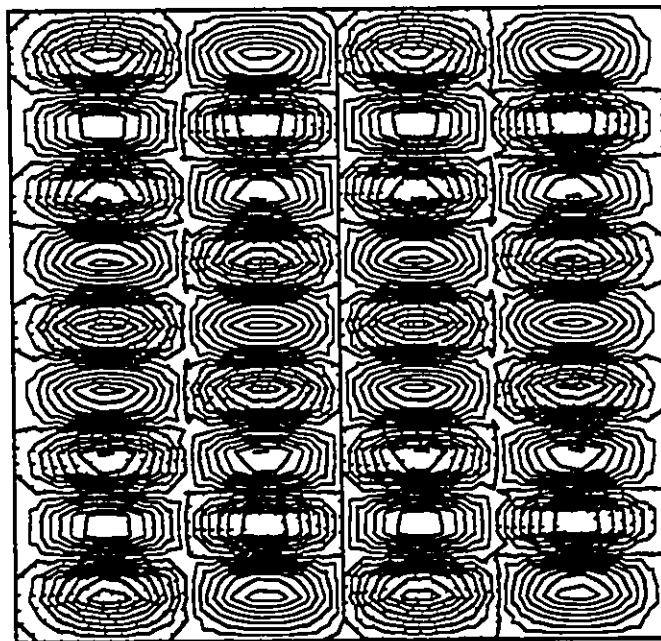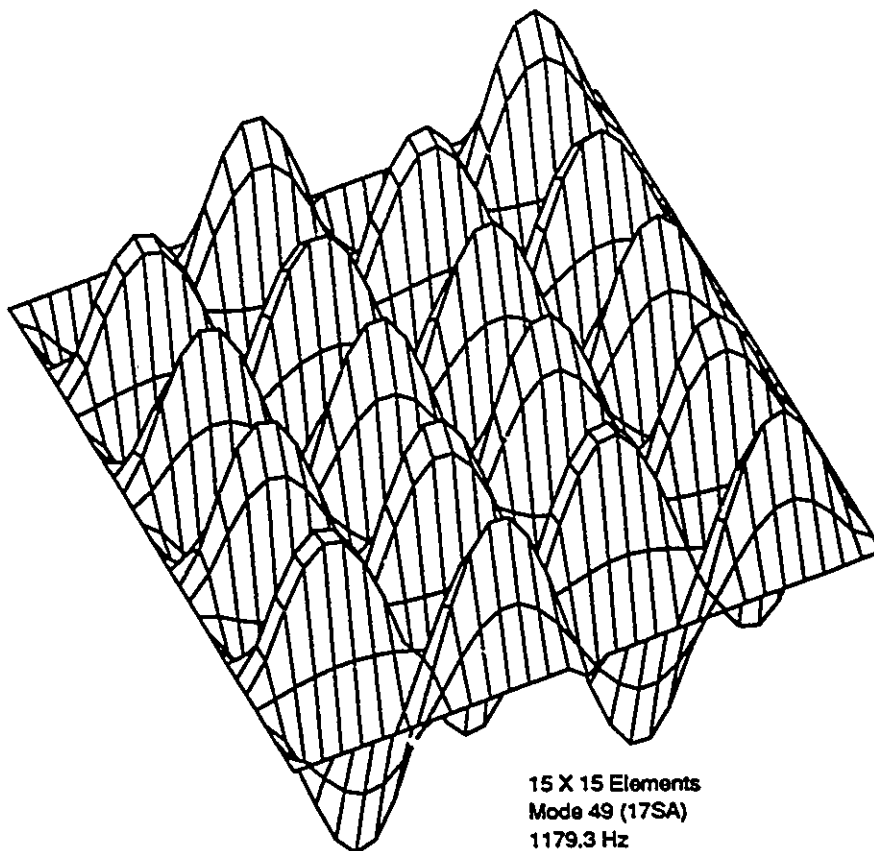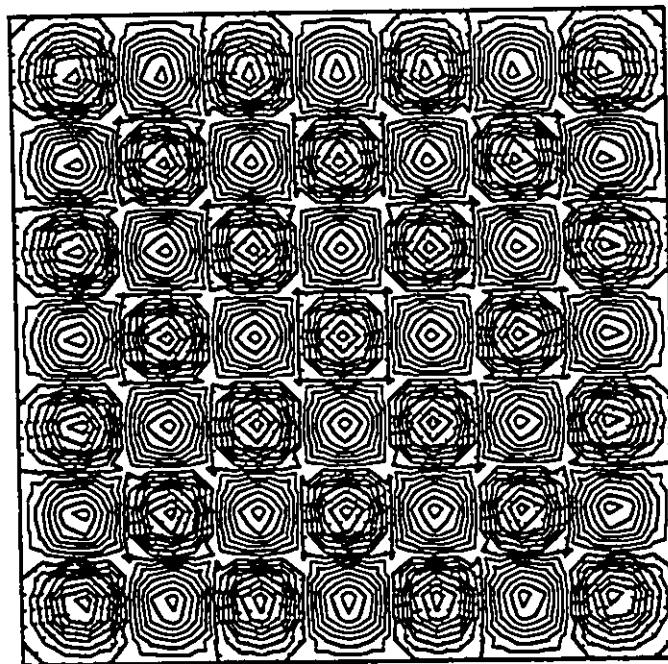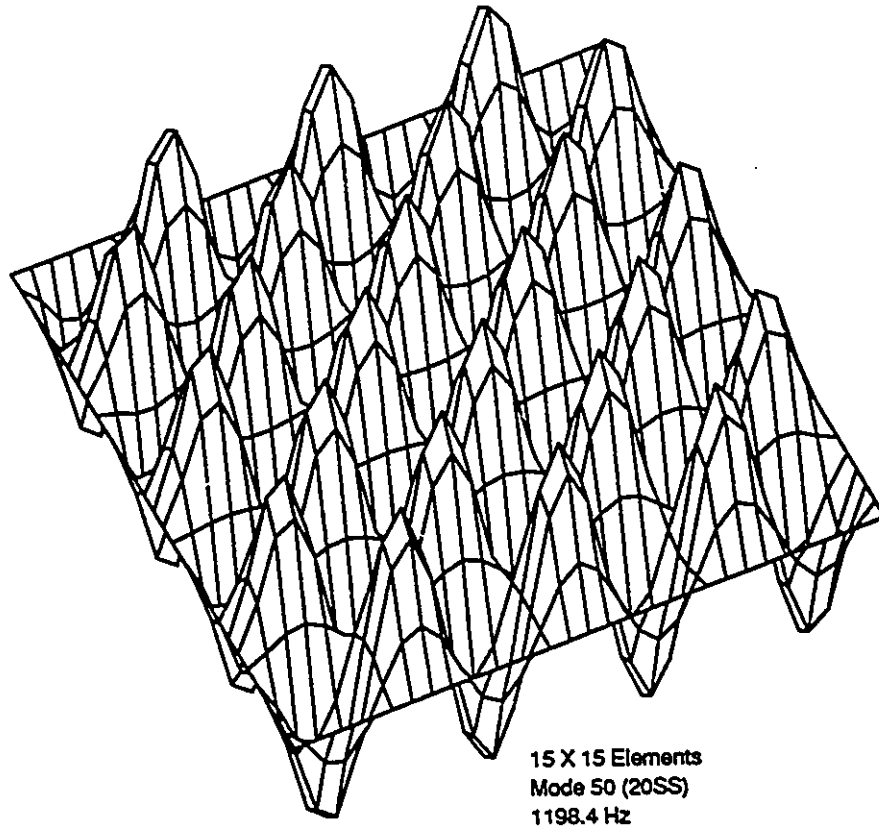
Vita Auctoris

Name:	Philip Albert Aylesworth
Place of Birth:	Windsor, Ontario
Year of Birth:	1960
Education:	J. L. Forster Secondary School, Windsor, Ontario. 1974-1978
	University of Windsor, Windsor, Ontario. B. A. Sc. 1984-1988
	University of Windsor, Windsor, Ontario. M. A. Sc. 1990-1993